

Design, Modelling and Sensing Possibilities of Magneto-Rheological Based Devices

THÈSE N° 7372 (2017)

PRÉSENTÉE LE 17 FÉVRIER 2017

À LA FACULTÉ DES SCIENCES ET TECHNIQUES DE L'INGÉNIEUR

LABORATOIRE D'ACTIONNEURS INTÉGRÉS

PROGRAMME DOCTORAL EN ROBOTIQUE, CONTRÔLE ET SYSTÈMES INTELLIGENTS

ÉCOLE POLYTECHNIQUE FÉDÉRALE DE LAUSANNE

POUR L'OBTENTION DU GRADE DE DOCTEUR ÈS SCIENCES

PAR

Daniel GRIVON

acceptée sur proposition du jury:

Prof. J. A. Schiffmann, président du jury

Prof. Y. Perriard, directeur de thèse

Prof. B. Dehez, rapporteur

Dr Z. Pataky, rapporteur

Prof. S. Henein, rapporteur



ÉCOLE POLYTECHNIQUE
FÉDÉRALE DE LAUSANNE

Suisse
2017

Les idées qui n'ont pas peur de l'avenir, qui au contraire se plaisent à regarder l'avenir sont celles qui font plus fortune et auxquelles naturellement est réservé l'avenir.

— *Emile Chanoux*

– Donca, teu i t'it un ricercatour?

– *Donc, toi t'es un chercheur?*

– *Oil.*

– *Oui.*

– Et di-quèi teu tchertché?

– *Et c'est quoi que tu cherches?*

Sèn qué llèi pas perdu.

– *Ce que je n'ai pas perdu.*

— *Dialogue entre un jeune doctorant et sa grand-mère*

Remerciements

Quoique acteur principal sur la scène, je n'aurais jamais pu accomplir de ce travail de thèse sans le soutien, l'aide et la présence d'un grand nombre de personnes qui ont joué un rôle tout sauf que secondaire. C'est avec ces quelques lignes que je tiens à tous vous remercier de ma façon la plus sincère.

Je remercie les Prof. Schiffmann, Dehez et Henein qui ont accepté de faire partie du jury pour l'examen de cette thèse et d'avoir lu et commenté mon travail.

Je voudrais remercier de façon particulière le Dr. Zoltan Pataky, des Hôpitaux Universitaires de Genève, pour avoir initié le projet à la base de cette thèse, pour sa contribution pour ce qui concerne la partie médicale et pour avoir partagé son enthousiasme envers le projet.

Je tiens également à remercier le Prof. Yves Perriard, non seulement pour son travail de directeur de thèse et son encadrement tout au long de mon doctorat, mais aussi pour l'incroyablement agréable ambiance qui réussit à créer dans son laboratoire, qui se démontre être une vraie équipe.

Ah, "*cet' équipe!...*"

Même si de façon différente, tous les collègues du laboratoire ont participé à enrichir mon parcours de doctorat. Parmi eux, un tout grand merci à Yoan, pour les interminables discussions, corrections et partages d'idées qui ont permis d'améliorer la qualité du travail de recherche que je présente. Merci également aux autres cadres du laboratoire, Paolo, pour ses conseils et son esprit pratique et Christian, pour avoir partagé sa maîtrise dans le domaine électromécanique. Sans oublier Magda et Myriam, pour leur patience et pour leur grande disponibilité. Un grand merci à tous les collègues avec qui, selon un parcours plus au moins long, j'ai partagé cette aventure: Omar, Chris, Tophe, François, Leopoldo, Romain, ShiDan, Xinchang, Jasha, Cécile, Florian, Jonathan, Louis, Guillaume et Douglas. Pendant ces quatre années j'ai amassé un grand trésor d'expériences et je garderai toujours ces souvenirs avec moi.

Enfin, un énorme merci à ma famille. C'est à vous que, comme personne d'autre, avez toujours été là pour me soutenir et m'encourager que je dédie ce travail.

Neuchâtel, janvier 2017

Daniel

Abstract

This work has been put in place during the development of an innovative medical device which consists in an intelligent footwear for foot plantar pressure redistribution in diabetic patients. In fact, despite the several sophisticated techniques developed in the last twenty years, diabetes remains one of the first causes of non-traumatic lower limb amputation worldwide. This is mainly due to the combination of peripheral neuropathy, which determines the loss of pain sensation in the lower extremities, and high plantar pressures, both recurrent among diabetic patients.

The target application imposes severe constraints for what concerns the system requirements because of the high plantar pressure magnitude and dynamics achieved by diabetic people during walking. Furthermore, the need to maintain the offloading system portable requires at the same time a high level of miniaturisation and a reduced power consumption.

Within a so challenging scenario, a regulating principle relying on Magneto-Rheological (MR) fluids, may represent a good solution. In fact, MR-based systems offer as main and common advantages high sustainable loads, high dynamic ranges of operation, low complexity, high reliability and low power consumption. MR fluids are a particular group of smart materials whose rheological properties (mainly the fluid internal yield stress which in turn determines the apparent viscosity of the fluid itself) can be controlled by an external magnetic field. With increasing levels of exciting field higher values of viscosity can be obtained, with the consequent possibility to control the material transition from the liquid to the semi-solid state.

The research work presented in this thesis focuses on MR valves, the core element of the offloading system conceived. Nevertheless, the analysis has been conducted in order to be as broad as possible and most of the concepts presented can be extended to all MR-based devices.

The development of an enhanced magnetic equivalent circuit to take into account relevant fringing and leakage phenomena is firstly addressed. High accuracy, flexibility and computational efficiency characterise the proposed approach which can be generalised to any axisymmetric structure.

Analytical models are developed to describe three MR valves configurations and the analysis steps followed can be used as guidelines to define a design methodology. A dimensioning routine is implemented to shape the valves structures in order to fulfil some imposed design

requirements and/or compare the different valves performances.

A qualitatively consistent attempt for the dynamic modelling of MR valves is presented through considerations on energy exchanges between the different physical domains involved. This analysis underlined that MR-based systems behave like transducers and their sensing possibilities are demonstrated experimentally. Finally, all the contents addressed contribute to the conception and realisation of a miniature MR soft shock absorber, the basic constitutive element of the variable stiffness sole conceived.

The research activities and the related results presented in this thesis do not pretend to definitely clarify and fix all points still open to question. The aim of this work is rather to provide some further elements and concepts to improve the design and modelling of MR-based devices.

Key words: Magneto-Rheological (MR) fluid, MR-based devices, high fidelity magnetic modelling, design methodology, dynamic modelling, sensing possibilities, miniaturisation.

Résumé

Ce travail de thèse a été mis en place dans le cadre du développement d'un dispositif médical novateur, i.e. une chaussure intelligente pour la redistribution des pressions plantaires chez les patients diabétiques. En effet, malgré les nombreuses et sophistiquées techniques qui ont été développées ces vingt dernières années, le diabète reste une des premières causes d'amputation non-traumatique dans le monde. Cela est principalement dû à la combinaison de la neuropathie périphérique, qui détermine une perte de la sensation de douleur dans les extrémités inférieures, et aux hautes pressions plantaires, les deux récurrents chez les diabétiques.

L'application ciblée impose des contraintes sévères pour ce qui concerne le cahier des charges, en premier lieu à cause des ordres de grandeurs et des dynamiques élevés qu'on retrouve dans la démarche des patients diabétiques. En outre, la nécessité de maintenir le système de décharge portable demande en même temps un processus de miniaturisation élevé et une faible consommation.

Dans le cadre d'un scénario de développement si exigeant, un principe de régulation basé sur les fluides Magnéto-Rhéologiques (MR), représente une solution intéressante. En effet, les dispositifs MR offrent, comme principaux avantages, la possibilité de soutenir des charges importantes, une vaste plage de dynamiques d'utilisation, un niveau de complexité réduit et une fiabilité remarquable tout en gardant une consommation réduite. Les fluides MR représentent un groupe particulier de matériaux intelligents dont les propriétés rhéologiques (principalement la contrainte de cisaillement interne du fluide qui détermine, en même temps, sa viscosité apparente) peuvent être contrôlées à l'aide d'un champ magnétique. Des valeurs croissantes du champ permettent d'obtenir des viscosités de plus en plus importantes, ce qui permet de contrôler la transition du matériel de l'état liquide à celui semi-solide.

Le travail de recherche présenté se concentre sur l'étude des valves MR. Néanmoins, un grand effort a été fait pour chercher à maintenir l'analyse menée la plus générale possible et la plupart des principes développés peuvent être étendus à tous les dispositifs MR.

Le développement d'un circuit magnétique équivalent à "haute-fidélité" qui tient compte des franges et des fuites est adressé en premier. Un haut niveau de précision, de flexibilité et une remarquable efficacité de calcul sont propres à l'approche proposée qui peut être généralisée à n'importe quelle structure axisymétrique.

Trois configurations de valve MR sont décrites à l'aide de modèles analytiques qui peuvent

être utilisés en tant que lignes directrices pour définir une vraie méthodologie de conception. Une routine de dimensionnement est également développée pour définir les géométries capables de satisfaire les contraintes imposées par le cahier des charges et comparer leurs performances.

Une modélisation dynamique des valves MR est ensuite présentée grâce à une approche de "haut niveau" basée sur des considérations concernant les échanges d'énergie parmi les différents domaines physiques impliqués. Cette analyse permet de faire ressortir la possibilité d'utiliser les dispositifs MR en tant que transducteurs, validée par la suite expérimentalement. Finalement, les contenus présentés convergent vers la conception et la réalisation d'un "amortisseur souple", élément central sur lequel l'application finale est basée.

Mots clés : Fluide Magnéto-Rhéologique (MR), systèmes MR, modélisation magnétique à "haute-fidélité", méthodologie de conception, modélisation dynamique, possibilités de détection, miniaturisation.

Riassunto

Il lavoro di ricerca presentato in questa tesi deriva dallo sviluppo di un innovativo dispositivo medico, ovvero una scarpa intelligente per la redistribuzione della pressione plantare nei pazienti diabetici. In effetti, nonostante le numerose e sofisticate tecniche che sono state sviluppate in questi ultimi anni, il diabete rimane una delle prime cause di amputazione non traumatica nel mondo. Ciò è principalmente dovuto alla combinazione di neuropatia periferica, che determina la perdita della sensazione di dolore nelle estremità inferiori, ed alle alte pressioni plantari, entrambi ricorrenti nei soggetti diabetici.

L'applicazione designata impone dei requisiti esigenti per quanto riguarda le specifiche, in primo luogo a causa dell'intensità e delle dinamiche elevate che caratterizzano la deambulazione dei diabetici. Inoltre, la necessità di mantenere il sistema di riduzione della pressione plantare portatile impone allo stesso tempo un processo di miniaturizzazione spinto oltre che un debole consumo.

All'interno di uno scenario di sviluppo così esigente, un principio di regolazione basato sui fluidi Magneto-Reologici (MR) rappresenta una soluzione interessante. In effetti, i dispositivi MR offrono, come vantaggi principali, la possibilità di sostenere carichi elevati, una vasta gamma di dinamiche di utilizzo, un livello di complessità ridotto ed un alto grado di affidabilità mantenendo un consumo di energia ridotto. I fluidi Magneto-Reologici (MR) rappresentano una particolare categoria di "*materiali intelligenti*" le cui proprietà reologiche (principalmente la tensione di snervamento interna del fluido che a sua volta determina la sua viscosità apparente) possono essere controllate tramite un campo magnetico di eccitazione. A crescente intensità del campo eccitante corrispondono crescenti valori di viscosità, da cui la conseguente possibilità di regolare la transizione del materiale dallo stato liquido a quello semi-solido.

Il lavoro di ricerca qui presentato si concentra sullo studio delle valvole MR. Nonostante ciò, il massimo sforzo è stato fatto per rendere l'analisi proposta quanto più generale possibile e la maggior parte dei concetti proposti può essere facilmente estesa a ogni dispositivo MR.

Dapprima, la definizione di una strategia di costruzione di un circuito magnetico equivalente ad "alta-fedeltà" capace di tenere conto dei flussi di frangia e di fuga viene proposta. Un alto livello di accuratezza, di flessibilità e una elevata efficienza di calcolo sono propri dell'approccio proposto che può essere facilmente generalizzato a qualsiasi struttura magnetica assialsimmetrica.

Tre configurazioni di valvole MR sono descritte tramite l'utilizzo di modelli analitici che possono essere usati come linee guida per definire una vera metodologia di concezione. Una routine di dimensionamento è ugualmente sviluppata per definire le geometrie capaci di soddisfare i vincoli imposti dalle specifiche e successivamente confrontare le loro prestazioni.

Una modellizzazione dinamica delle valvole MR è in seguito introdotta grazie ad un approccio ad "alto livello" basato su considerazioni legate allo scambio di energia fra i diversi domini fisici implicati. Questa analisi permette di far emergere la possibilità di utilizzare i dispositivi MR come dei trasduttori, ipotesi verificata sperimentalmente. Infine, i contenuti presentati convergono nello sviluppo e realizzazione di un "ammortizzatore flessibile", l'elemento centrale su cui l'applicazione finale è basata.

Parole chiave: Fluidi Magneto-Reologici (MR), dispositivi MR, modellizzazione magnetica ad "alta-fedeltà", metodologia di concezione, modellizzazione dinamica, possibilità di detezione, miniaturizzazione.

Contents

Abstract (English/Français/Italiano)	iii
List of figures	xiii
List of tables	xvii
1 Introduction	1
1.1 Magnetics, Rheology and Fluid Mechanics	2
1.2 Magneto-Rheological (MR) fluids	3
1.2.1 Typical properties of MR fluids	5
1.2.2 MR fluids operational modes	9
1.2.3 MR fluid flow between fixed parallel plates	11
1.2.4 MR fluid flow through annular and radial channels	12
1.3 MR valve configurations	13
1.3.1 Annular MR valve	13
1.3.2 Radial MR valve	14
1.3.3 Annular-Radial MR valve	15
1.4 Extension to generic MR-based devices	15
1.5 Content of the thesis	17
2 High Fidelity Magnetic Equivalent Circuit for Axisymmetric Devices	21
2.1 Introduction	22
2.2 Finite Element Based semi-empirical modelling	23
2.3 HFMEC of MR valves	32
2.3.1 Permeances Calculation	33
2.3.2 MEC Permeances	33
2.3.3 HFMEC Permeances	35
2.4 Results	39
2.5 Summary and conclusion	43
3 Design and Comparison of Different MR Valves Configurations	47
3.1 Introduction	48
3.2 Evaluation criteria for MR valves	49
3.3 MR valves analysis	50

Contents

3.3.1	Annular MR valve	50
3.3.2	Radial MR valve	55
3.3.3	Annular-Radial MR valve	57
3.4	Design Methodology for MR Valves	60
3.4.1	Design equations assuming magnetic flux conservation	60
3.4.2	Design equations extension for the inclusion of HFMEC	61
3.4.3	Complete design routine	62
3.5	Results	64
3.6	Summary and conclusion	70
4	Dynamic Modelling and Sensing Possibilities of MR Valves	73
4.1	The Bond Graph modelling approach	74
4.1.1	Bond Graph Variables and Physical Analogies	74
4.1.2	Bond Graph Elements	75
4.2	A useful case study: the electromagnet as a transducer	78
4.3	Bond Graph modelling of MR valves	81
4.3.1	Electro-magnetic domain modelling	82
4.3.2	Hydraulic domain modelling	83
4.3.3	Complete MR valve bond graph model	89
4.4	Sensing Possibilities of MR valves	91
4.4.1	Experimental sessions and results	91
4.5	Summary and conclusions	95
5	Case Study: Miniature Soft Plantar Pressure Limiter for Smart Footwear	99
5.1	Introduction: Foot neuropathy in diabetic patients	100
5.2	Intelligent footwear for foot plantar pressure redistribution	103
5.2.1	Offloading strategy	103
5.2.2	System requirements	105
5.3	Miniature soft MR pressure limiters	108
5.3.1	Offloading module configuration	110
5.3.2	Deformable cushion	111
5.3.3	Elastic reflow membrane	112
5.3.4	Miniature MR Valves	112
5.3.5	Complete MR miniature soft pressure limiter	114
5.4	Experimental sessions and results	115
5.4.1	Static measurements	116
5.4.2	Dynamic measurements	117
5.5	Summary and Conclusion	120
6	Conclusions and Perspectives	125
6.1	Original Contributions	126
6.2	Outlook	127

A Flow of Bingham fluid between two fixed parallel plates	129
B Complete permeances formulations	135
B.1 MEC permeances	135
B.2 Fringing permeances	135
C Bond graph elements: A more complete overview	141
C.1 Power conserving junctions	141
C.2 Energy Storage Elements	142
C.2.1 1-port C energy store	142
C.2.2 1-port I energy store	143
C.3 Dissipators	145
C.4 Ideal Energy Sources	145
C.5 Couplers	146
C.5.1 Transformers	146
C.5.2 Gytrators	147
Nomenclature	149
Curriculum Vitae	153

List of Figures

1.1	Schematic diagram representing the different physics involved in the study of MR fluids.	2
1.2	Classification of existing fluids according to their different rheological behaviour.	3
1.3	(a) - Infinitesimal fluid element under an applied strain $\frac{d\theta}{dt}$. (b) - Velocity profile distribution near the wall for a Newtonian fluid.	3
1.4	Magneto-Rheological phenomenon.	4
1.5	Schematic representation of the Yield stress Vs Shear rate characteristic of a MR fluid	5
1.6	BH characteristic for the MRF132CG.	6
1.7	Shear stress Vs Strain rate characteristic for the MRF132CG.	7
1.8	Yield stress Vs Magnetic field characteristic for the MRF132CG.	8
1.9	MR fluid operational modes.	10
1.10	Yield stress distribution and velocity profile for MR fluid flow between two parallel plates.	11
1.11	The two main axisymmetric channel geometries considered.	12
1.12	Schematic representation and main elements for the annular MR valve configuration.	14
1.13	Schematic representation and main elements for the radial MR valve configuration.	14
1.14	Schematic representation and main elements for the annular-radial MR valve configuration.	15
1.15	The two basic configurations of the main MR devices other than MR valves.	16
2.1	Cross-sectional schematic representation of the fringes approximation in the case of an annular air gap.	23
2.2	Cross-sectional representation of infinitesimal quarter of hollow toroids for the flux tubes associated with internal and external arc-shaped fringes.	24
2.3	Infinitesimal internal arc-shaped permeances $d\Lambda_{int}$	27
2.4	Infinitesimal external arc-shaped permeances $d\Lambda_{ext}$	28
2.5	Graphical representation of the contribution of the infinitesimal permeances $d\Lambda_A$ and $d\Lambda_B$	29
2.6	Graphical representations of the different permeances contributions to model fringes originating at magnetic domains interfaces.	30
2.7	Disc geometry with a thickness increasing proportionally with its radius.	31

List of Figures

2.8	Relative errors of the existing methods and the proposed model for the fringing permeance computation with respect to FEA results.	32
2.9	Annular MR valve configuration: (a) - Nodes placement for the lumped magnetic model. (b) - Corresponding HFMEC.	34
2.10	Elementary domains for the computation of MEC permeances: (a) - Cylindrical geometry. (b) - Disc geometry.	35
2.11	Iterative solution flow chart used to solve the magnetic circuits for nonlinear permeability materials.	39
2.12	Annular MR valve configuration: (a) - Magnetic inductions B_{MR} in the valve channel obtained with the different models. (b) - Relative error of the used methods with respect to FE results.	40
2.13	Radial MR valve configuration: (a) - Magnetic inductions B_{MR} in the valve channel obtained with the different models. (b) - Relative error of the used methods with respect to FE results.	40
2.14	Annular-Radial MR valve configuration: (a) - Magnetic inductions B_{MR} in the valve annular channel obtained with the different models. (b) - Relative error of the used methods with respect to FE results.	41
2.15	Annular-Radial MR valve configuration: (a) - Magnetic inductions B_{MR} in the valve radial channel obtained with the different models. (b) - Relative error of the used methods with respect to FE results.	41
3.1	Schematic representation and geometrical parameters for the annular MR valve configuration.	50
3.2	Schematic representation and main geometrical parameters used to describe the radial MR valve configuration.	55
3.3	Schematic representation and main geometrical parameters for the annular-radial MR valve configuration.	57
3.4	Schematic representation of the approach used to implement the proposed design methodology for an annular MR valve.	63
3.5	Comparison of the different dynamic ratios of the MR valves configurations. . .	65
3.6	Comparison of the different pressure densities of the MR valves configurations. . .	66
3.7	Comparison of the different reactivities of the MR valves configurations.	67
3.8	Comparison of the different efficiencies of the MR valves configurations.	68
4.1	(a) - Causality for an effort determined/imposed by the element A . (b) - Causality for a flow determined/imposed by the element A . In both the cases element A supplies power to element B	76
4.2	Schematic representation of and electromagnet.	78
4.3	Convenient integration path chosen.	79
4.4	Bond graph representation of the electromagnet transducers imposing preferred integrative causalities on its ports.	80
4.5	Bond graph of the electromagnet transducer further detailed introducing the gyrator describing the coil. Integrative causalities are imposed on its ports.	80

4.6	Bond graph model of the electromagnet.	81
4.7	From left to right: common equivalent representation of a permeance, bond graph representation of the corresponding 1-port C energy storage (with integrative causality) and associated characteristic equation.	82
4.8	Bond graph model of the electro-magnetic domains for the annular valve.	83
4.9	Graphical representation of the annular valve characteristic depending on the independent variable chosen.	84
4.10	Bond graph model of a fast switching element used to model the annular valve.	85
4.11	Schematic representation of the equivalent hydraulic circuit used to model the annular valve.	86
4.12	Assumed variation of the channel volume due to the apparent increase of the channel length.	87
4.13	Evolution in aggregate microstructure of MR fluid. Flow positive direction is from top to bottom, while exciting magnetic field horizontal. The Mason numbers in the images are: (a) - ∞ (field-off), (b) - 0.16, (c) - 0.018, (d) - 0.0016, (e) - 0.00014. The channel dimensions are $w = 1.2$ mm and $h = 0.3$ mm [8].	88
4.14	Bond graph model of the hydraulic domain for a general MR valve.	89
4.15	Complete bond graph model of the annular MR valve.	90
4.16	Results from the first experimental session described for unidirectional flow rate. (a) - Measured induced voltage. (b) - Pressure drop and flow rate.	93
4.17	Results from the second experimental session described for which bidirectional flow rate is imposed. (a) - Measured induced voltage. (b) - Pressure drop and flow rate.	94
5.1	Diabetes mellitus is responsible for a variety of foot pathologies contributing to the complications of ulceration and amputation. Multiple pathologies may be implicated, from vascular disease to neuropathy and mechanical trauma [6].	100
5.2	Neuropathic ulcer in typical position under second metatarsal head [10].	101
5.3	State of the art offloading techniques for the diabetic foot treatment (images freely available online).	102
5.4	Definition of the Regions of Interest, zone with high ulceration risk and the discretisation of the foot plantar to locate the variable stiffness modules.	104
5.5	Sagittal view of the sole with a representation of the intended offloading strategy.	104
5.6	Typical non-linear stress-strain characteristic of the foot plantar tissue under the metatarsal heads. Modified from [15].	105
5.7	Phases of the gait cycle (modified from [20]).	107
5.8	Basic MR damper configuration.	108
5.9	The footwear with a controllable stiffness system made of bladders filled with MR fluid presented in [26].	110
5.10	Schematic representation of the configuration proposed to realise the soft MR pressure limiter.	111

List of Figures

5.11	Detailed cross-section and main dimensions of the bellow embedding a miniaturised sensor to measure the fluid pressure inside the deformable cushion. . .	112
5.12	Detailed representation of the miniature annular valve MR.	113
5.13	Detailed representation of the miniature radial valve MR.	114
5.14	The three main parts composing the plantar pressure limiter: SLA deformable cushion, an annular MR valve and base support with the reflow membrane (from left to right).	114
5.15	Detailed cross-section of the complete miniature soft MR plantar pressure limiter.	115
5.16	Comparison of the static measurements of the different subsystems under test.	116
5.17	Different events occurring in the performed test session.	117
5.18	Vertical deformations of the annular modules supplied with different current densities (dashed lines) and valve state with straight Boolean convention (red piecewise line).	118
5.19	Vertical deformations of the radial modules supplied with different current densities (dashed lines) and valve state with straight Boolean convention (red piecewise line).	119
5.20	3D concept of the intelligent footwear for diabetic patients with foot insensitivity embedding the developed miniature MR shock absorbers.	121
A.1	Schematic representation of an infinitesimal fluid element defined with respect to a cylindrical coordinate system.	129
B.1	Radial MR valve configuration: (a) - Nodes placement for the lumped magnetic model. (b) - Corresponding HFMEC.	137
B.2	Annular-Radial MR valve configuration: (a) - Nodes placement for the lumped magnetic model. (b) - Corresponding HFMEC.	139
C.1	Power junctions representation and related causality assignment.	142
C.2	Causality assignment for 1-port C elements.	144
C.3	Causality assignment for 1-port I elements.	144
C.4	Bondgraph representation of a 1-port R element.	145
C.5	(a) - Effort source. (b) - Flow source.	146
C.6	(a) - Transformer with imposed effort at the input. (b) - Modulated transformer with imposed flow at the input.	146
C.7	(a) - Gyrator with imposed effort at the input. (b) - Modulated gyrator with imposed flow at the input.	147

List of Tables

2.1	Optimal angles θ_i^* and θ_e^*	26
2.2	Maximum ($\max\{\varepsilon_{B_{MR}}\}$) and mean ($\bar{\varepsilon}_{B_{MR}}$) relative errors between FE analysis and analytical model results.	42
2.3	Maximum ($\max\{\varepsilon_L\}$) and mean ($\bar{\varepsilon}_L$) relative errors between FE analysis and analytical model results.	42
3.1	Intrinsic properties of the materials composing the valves structures. The fluid considered is the MRF132CG by Lord.	64
3.2	Maximum ($\max\{\varepsilon_{D_i}\}$) and mean ($\bar{\varepsilon}_{D_i}$) relative errors between FE analysis and analytical model results for the valves dynamic ranges D	65
3.3	Maximum ($\max\{\varepsilon_{\kappa_i}\}$) and mean ($\bar{\varepsilon}_{\kappa_i}$) relative errors between FE analysis and analytical model results for the valves pressure to volume ratios κ	66
3.4	Maximum ($\max\{\varepsilon_{\mathcal{R}_i}\}$) and mean ($\bar{\varepsilon}_{\mathcal{R}_i}$) relative errors between FE analysis and analytical model results for the valves reactivities \mathcal{R}_i	67
3.5	Maximum ($\max\{\varepsilon_{\mathcal{E}_i}\}$) and mean ($\bar{\varepsilon}_{\mathcal{E}_i}$) relative errors between FE analysis and analytical model results for the valves efficiencies \mathcal{E}_i	69
4.1	Energy domains and related bond graph variables.	75
4.2	Bond graph elements, corresponding representation and constitutive relations.	77
5.1	Different PPs distribution in diabetic [8] and healthy patients [9]. Pressures refer to the maxima measured in each region in barefoot condition.	101
5.2	MR valve requirements for the two design scenarios chosen.	112
5.3	MR valves parameters for the two design scenarios (geometrical dimensions are expressed in [mm]). The actual coil number of turns and measured resistances are also reported with respect to reference design values (given in parentheses).	113
5.4	Power consumption of the different shock absorbers tested.	120
B.1	Permeances for the MECs of the different MR valve configurations studied.	140

1 Introduction

Magneto-Rheological (MR) fluids are a particular kind of smart materials able to change their rheological properties, namely their internal yield stress, if excited by an external magnetic field. Based on this phenomenon, several power dissipating devices as brakes and clutches, dampers and valves have been developed. Although their features are well-known and MR-based systems are currently employed all over the world, it has been found that some design and modelling aspects are not clearly defined and require further investigation to be more comprehensively analysed.

In order to guide the reader throughout the developments discussed in the following chapters, which address the design and modelling of MR-based devices, focusing the attention on MR valves, a preliminary introduction to define the main features and the basic theory to describe MR fluids is required, which is the main content of this chapter.

1.1 Magnetism, Rheology and Fluid Mechanics

Magneto-Rheological (MR) fluids incorporate and relate in themselves several branches of physics. Electromagnetism, fluid mechanics and rheology have to be addressed when dealing with this particular kind of materials (Fig. 1.1).

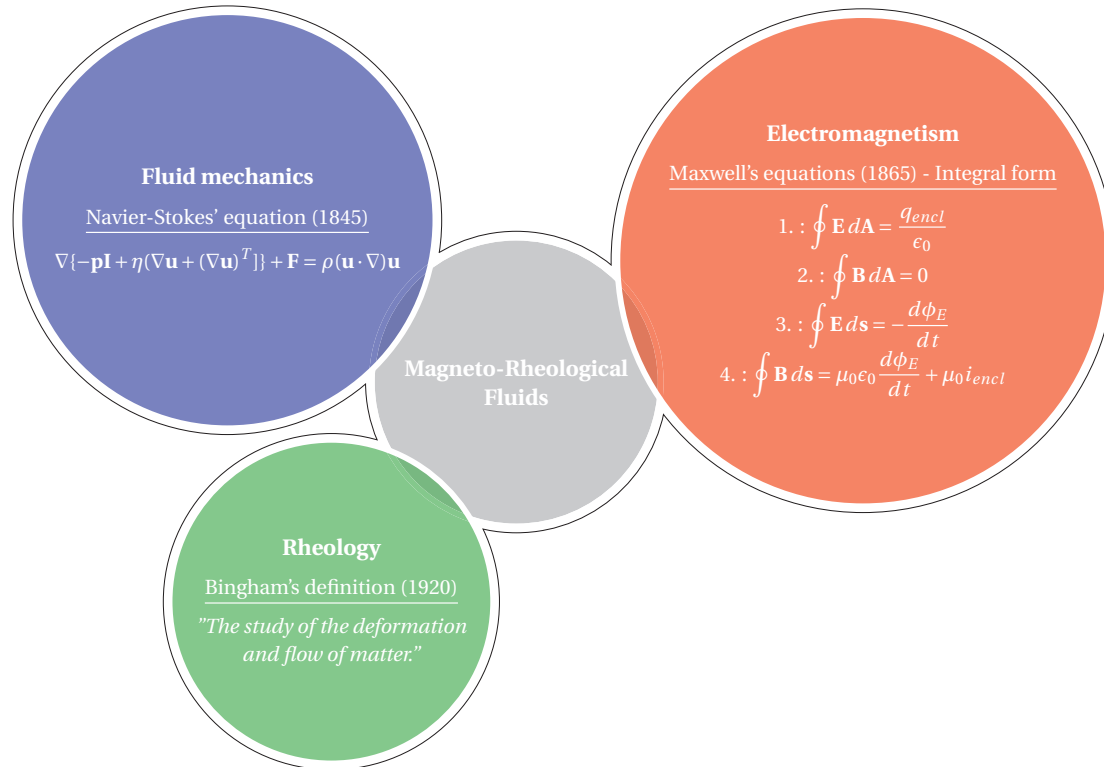


Figure 1.1 – Schematic diagram representing the different physics involved in the study of MR fluids.

Concerning electromagnetism and fluid mechanics, they are respectively described by mean of the Maxwell's and Navier-Stokes' equations. Rheology is a term relatively new and it has been coined by professor Bingham to define the branch of physics that deals with the deformation and flow of matter, especially the non-Newtonian flow of liquids and the plastic flow of solids [1].

In the following discussion, fluid mechanics will be used as the preamble to introduce the rheological behaviour and underline the relevant features of MR fluids, while electromagnetism will describe both the source of excitation inducing the material transition from the liquid to the semi-solid state and its magnetic properties.

1.2 Magneto-Rheological (MR) fluids

All existing fluids can be divided into two main categories depending on their particular rheological behaviour: *newtonian* and *non-newtonian* fluids (Fig. 1.2) [2].

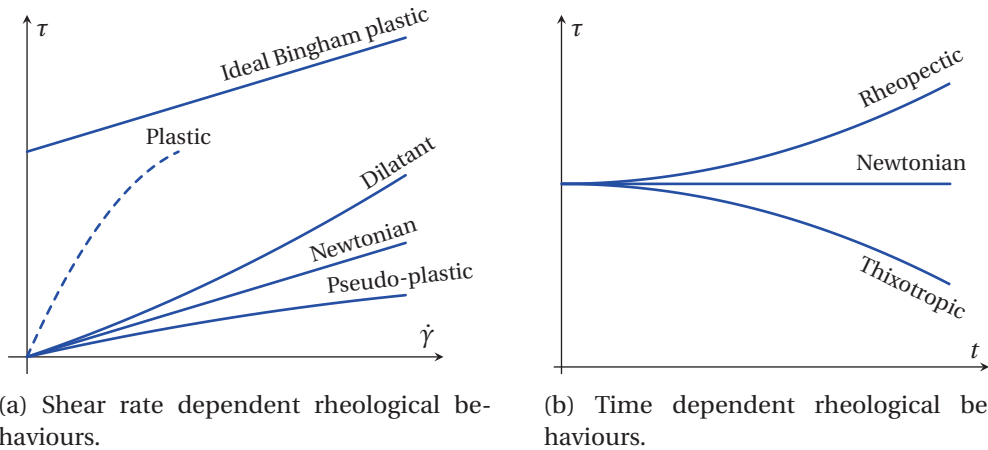


Figure 1.2 – Classification of existing fluids according to their different rheological behaviour.

Although a further classification can be performed on the *non-newtonian* category, all the *newtonian* fluids are satisfactorily described by the same relation. Furthermore, it is found that the definition of some *non-newtonian* liquids, as in the case of MR fluids, is given with respect to the general formulation of *newtonian* fluids. A preliminary introduction of their main features is thus required.

When a shear stress τ is applied to an infinitesimal newtonian fluid element (Fig. 1.3a), the resulting deformation can be described by the angle θ which defines the shear strain rate $\dot{\gamma}$. Moreover, if infinitesimal variations are assumed, the latter can be easily related geometrically

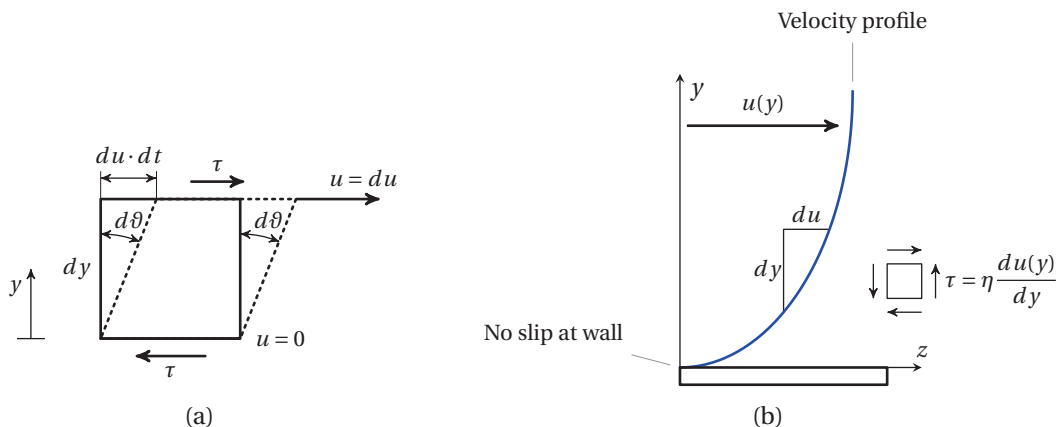


Figure 1.3 – (a) - Infinitesimal fluid element under an applied strain $\frac{d\theta}{dt}$. (b) - Velocity profile distribution near the wall for a Newtonian fluid.

Chapter 1. Introduction

with the velocity gradient along the direction orthogonal to the applied shear, which leads

$$\dot{\gamma} = \frac{d\vartheta}{dt} = \frac{du(y)}{dy} \quad (1.1)$$

where $u(y)$ is the fluid velocity profile along the coordinate y in the case of a planar geometry (Fig. 1.3b). This expression can be directly related to the shear stress by mean of the intrinsic fluid viscosity η , giving the well-known relation

$$\tau = \eta \frac{d\vartheta}{dt} = \eta \dot{\gamma}. \quad (1.2)$$

For what concerns MR fluids, they can be defined as smart materials composed by magnetic particles, with dimensions ranging from 1 to 20 μm , dispersed in a non-magnetic liquid carrier, usually oil or water [3]. The main property of MR fluids is the reversible capability of their constituting particles to be magnetised when exposed to moderate magnetic fields (lower than 200 kA/m) becoming nearly single domain magnets [4]: the induced particles interaction allows the formation of chain-like structures aligned parallel to the applied magnetic field (Fig. 1.4).

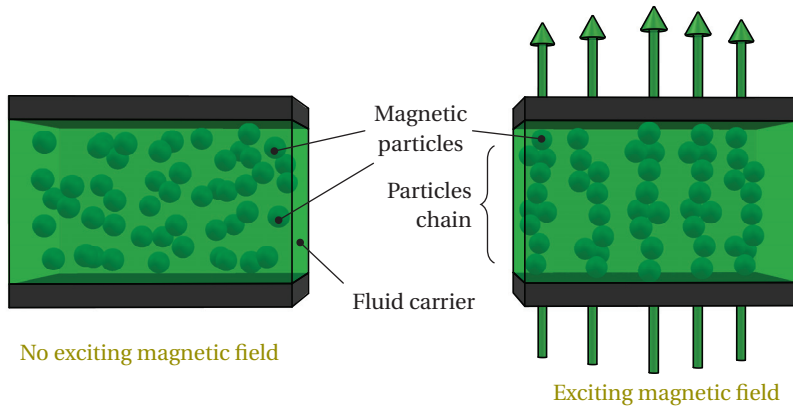


Figure 1.4 – Magneto-Rheological phenomenon.

The strength of the attractive forces between adjacent particles and, thus, the stability of the particles clusters are mainly related to the magnitude and distribution of the exciting magnetic field H [5]. In this respect, the description of the introduced phenomenon could be done at the microscopic level, considering the mechanical frictions due to fluid-particles interactions and the magnetic forces originating among the nearby magnetised particles. Nevertheless, this kind of modelling is intended to give a description which may result overdetailed, in particular if the main interest is related to the dimensioning of MR-based devices.

For this reason, in the following discussion the common macroscopic model of MR fluids will be used. The latter assumes that the fluid-particles and particles-to-particles interactions determine the raise of a magnetic field dependent yield stress $\tau_y(H)$ required to deform the particles clusters and obtain a variation of the fluid shear strain rate. For this reason, MR fluids

are defined as *non-newtonian* fluids and they are commonly described using the Bingham plastic model [1]

$$\begin{cases} \tau(H) = \tau_y(H) + \eta\dot{\gamma}, & \tau > |\tau_y| \\ \dot{\gamma} = 0, & \tau \leq |\tau_y|. \end{cases} \quad (1.3)$$

It results that the internal fluid shear stress is a function of both the shear strain rate and the exciting magnetic field (Fig. 1.5).

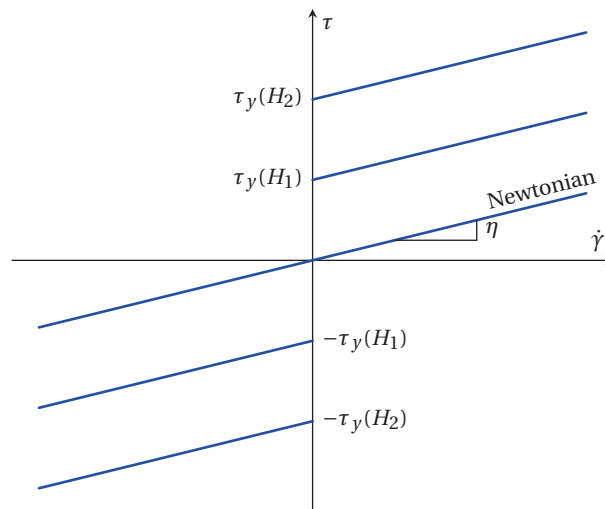


Figure 1.5 – Schematic representation of the Yield stress Vs Shear rate characteristic of a MR fluid

Given this preliminary introduction, it is interesting to address more precisely the magnetic and rheological properties of these smart materials. This will be the main topic discussed in the following section.

1.2.1 Typical properties of MR fluids

Hereunder, both the main magnetic and rheological features of MR fluids are presented. In particular, their introduction is given using as reference the experimental characteristics provided for the fluid MRF132CG produced by *Lord Corp* [6].

1.2.1.1 Magnetic properties

As for all the other existing ferromagnetic materials, for MR fluids a B-H curve can be defined as well. Such experimental characteristic provides, as its two main information, the saturation induction limit and the material relative permeability. In particular, considering that MR fluids are actually a mixture of a non-magnetic and a magnetic material, the first quantity can be only determined experimentally. On the contrary, the effective relative permeability of the MR

fluid can be determined using the Maxwell-Garnett rule [7]

$$\mu_{eff. MR} = \mu_m \frac{\mu_p(1 + 2\nu_p) - \mu_m(2\nu_p - 2)}{\mu_m(2 + \nu_p) + \mu_p(1 - \nu_p)} \quad (1.4)$$

where μ_m and μ_p are the relative permeability of the carrier medium and the magnetic particles respectively, while ν_p is the volume fraction of the inclusion (i.e. of the particles). In particular, in relation to the fact that the latter can be represented as perfect spheres, the value of this last parameter will always be $\nu_p \leq \frac{\pi}{3\sqrt{2}}$ ¹ [8] and, considering that the maximum relative permeability of the particles themselves is in the order of 10^3 , the maximum effective permeability of MR fluids is $\mu_{eff. MR} \leq 7$.

Figure 1.6 shows the experimental B-H curve provided for the MRF132CG. The slope of the characteristic at the origin (represented with a red dash-dotted line in the graph) allows to directly define the effective relative permeability of the MR fluid which, for the particular case considered, is $\mu_{MR} = 5.46$. Similarly, the trend of the B-H curve for the highest values of magnetic field can be approximated with a straight line (illustrated with a black dash-dotted curve in the plot) and its intersection with the ordinate axis defines the limit for the material saturation induction B_{MR} , which is 0.6 T.

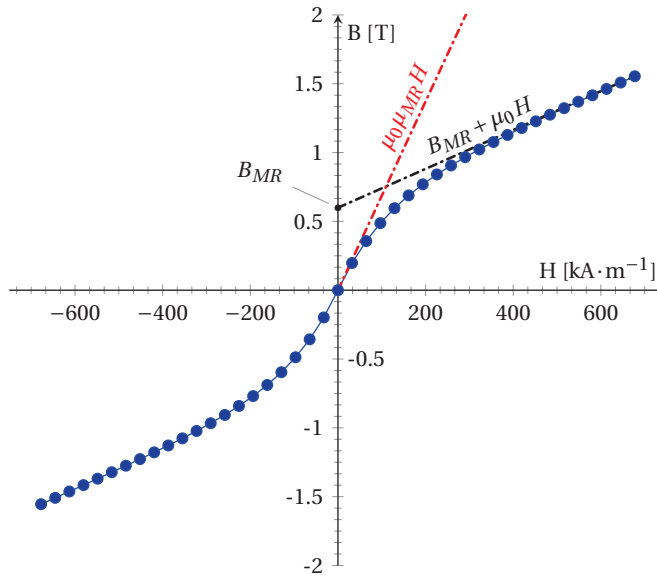


Figure 1.6 – BH characteristic for the MRF132CG.

1.2.1.2 Rheological properties

Although the general and most common formulation to define the behaviour of MR fluid has already been given with the Bingham model (1.3), in many cases this description results to be

¹This value is given considering the best possible packing of spheres, which result to be the *cubic close* and/or the *hexagonal packing*.

too simplistic. This is mainly related to the net discontinuity present in the model provided by Bingham which is a rough approximation of the reality and it may results difficult to handle, for example for the implementation in a Finite Element software. For these reasons, several alternative formulations have been proposed.

Among the possible regularisation models, the continuous Bingham-Papanastasiou formulation has proven to provide the best approximation of the ideal discontinuous model, being able to accurate describe the real fluid features while maintaining a reduced degree of complexity [9]. For simple shear in one dimension, the Bingham-Papanastasiou formulation states [10]

$$\tau = \tau_y \left[1 - \exp(-\nu |\dot{\gamma}|) \right] + \eta \dot{\gamma}. \quad (1.5)$$

Considering the relation between shear stress, viscosity and shear rate strain for a newtonian fluid (1.2), it is possible to define the non-linear magnetic field dependent viscosity according to the Papanastasiou formulation as

$$\eta = \frac{\tau_y(H)}{\dot{\gamma}} \left[1 - \exp(-\nu |\dot{\gamma}|) \right] + \eta_0 \quad (1.6)$$

where η_0 represents the viscosity of the fluid if the field induced yield stress is 0 (no external magnetic field applied). For MRF132CG, $\eta_0 = 0.092 \text{ Pa}\cdot\text{s}$, while the coefficient ν defines the degree of smoothing of the ideal model discontinuity. It's optimal value $\nu = 0.25$ has been found applying a regression algorithm to fit (1.6) to the experimental shear stress - strain rate characteristic for MRF132CG, which is displayed in Fig. 1.7.

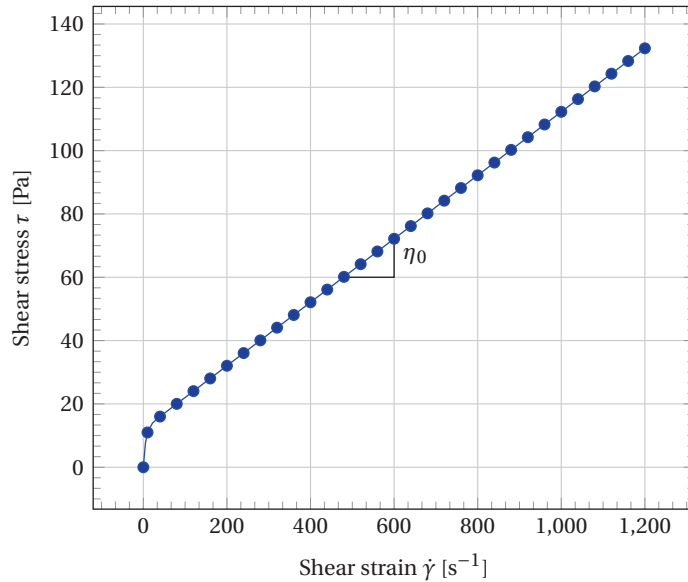


Figure 1.7 – Shear stress Vs Strain rate characteristic for the MRF132CG.

1.2.1.3 Magneto-Rheological properties

The probably most important feature of a MR fluid is its magnetic field dependent yield stress. As for many other experimentally obtained characteristics, it is common practice to try to provide an analytical model for the definition of $\tau_y(H)$ able to continuously describe the real behaviour of MR fluid while remaining relatively easy to implement. For what concerns MR fluids, the simplest analytical relation well-fitting the typical magnetic field dependent yield stress trend is [16]

$$\tau_y(H) = \alpha H^\beta. \tag{1.7}$$

It can be seen in Fig. 1.8, that a knee in the curve exists. This underlines that, starting from a certain value of magnetic field intensity, the obtainable yield stress tends to saturate. This can be justified considering that the ferromagnetic material which the fluid particles are made exhibits a saturation limit as well, that avoids the inter-particles forces to increase linearly. To further strengthen this consideration, if Fig. 1.6 and 1.8 are compared, it can be seen that the knees in the characteristics correspond. Furthermore, if only moderate magnetic fields are considered, it can be well observed that the first part of the curve exhibits an almost linear behaviour, which corresponds to impose the term β in (1.7) equal to 1 reducing the model to the straight dash-dotted black line shown in Fig. 1.8. In particular, for the MRF132CG, it results that $\alpha = 0.325 \text{ N} \cdot \text{A}^{-1} \cdot \text{m}^{-1}$. Although this approximation could appear rough, its quality may be considered sufficient for the initial design phases of a MR device assessing the feasibility of a particular solution and in the case that only moderate magnetic fields (below the material saturation limit) are allowed.

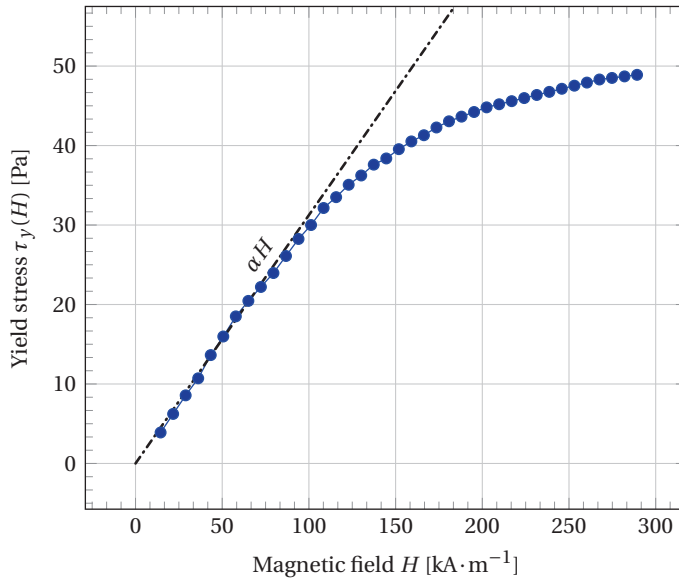


Figure 1.8 – Yield stress Vs Magnetic field characteristic for the MRF132CG.

Figure 1.8 displays the characteristic which is probably the most relevant in the definition of the MR phenomenon. Considering that the introduction given up to this point is considered successively exhaustive to develop all the concepts introduced in the following, it is now interesting to define how this particular rheological behaviour can be used as starting point for the design of real-life MR devices.

1.2.2 MR fluids operational modes

The introduced MR phenomenon can be used in four different operational modes which provide the basis for the design of all MR devices: *flow mode*, *shear mode*, *squeeze mode* [11] and *pinch mode* [12].

1.2.2.1 Flow mode

In this mode, the fluid flows through a channel while being crossed orthogonally by an external magnetic field (Fig. 1.9a). The resistance of the fluid to flow is controlled varying the magnetic field intensity and inducing, this way, the rise of a pressure drop ΔP across the considered duct. This operational mode is mainly used to design continuously controllable valves without any mechanical parts in relative motion to each other.

1.2.2.2 Shear mode

The fluid is constrained between two moving parts, called poles, while the exciting magnetic field is directed orthogonal to the latter (Fig. 1.9b). When a shear force, in opposite direction, is applied respectively to the two poles, their relative motion and shearing of the fluid in between are obtained. The resistance against the applied shear is related to the exciting magnetic field intensity. The main applications employing this principle of operation are brakes and clutches.

1.2.2.3 Squeeze mode

Similarly to what introduced before, for this operational mode the MR fluid is contained between two parallel poles and the exciting magnetic field is applied perpendicularly to them. A compression force is exercised on both the plates, determining the squeeze of the MR fluid because of the approach of the two poles (Fig. 1.9c). The magnetic field intensity can be used to modulate the squeeze resistive force and, consequently, the distance between the poles. Nevertheless, the actual range of controllable displacements is reduced to some percentage of the total pole distance when no exciting force is applied. On the contrary, the obtainable resistive force in the MR fluids are relevant, but highly non-linear. Shock absorbers and small amplitude vibrations dampers can be designed using this operating principle.

1.2.2.4 Pinch mode

In this mode, the fluid is forced to flow between two parallel walls which also carry the exciting magnetic field (Fig. 1.9d). Once encountering a non-magnetic spacer located in the lateral barriers, the magnetic path is forced to cross the fluid flow and, because of the transition of the fluid in the semi-solid state in this region and near the walls, an orifice generates in the middle of the channel. Controlling the magnetic field intensity, it is possible to control the orifice dimensions and, consequently, the fluid flow.

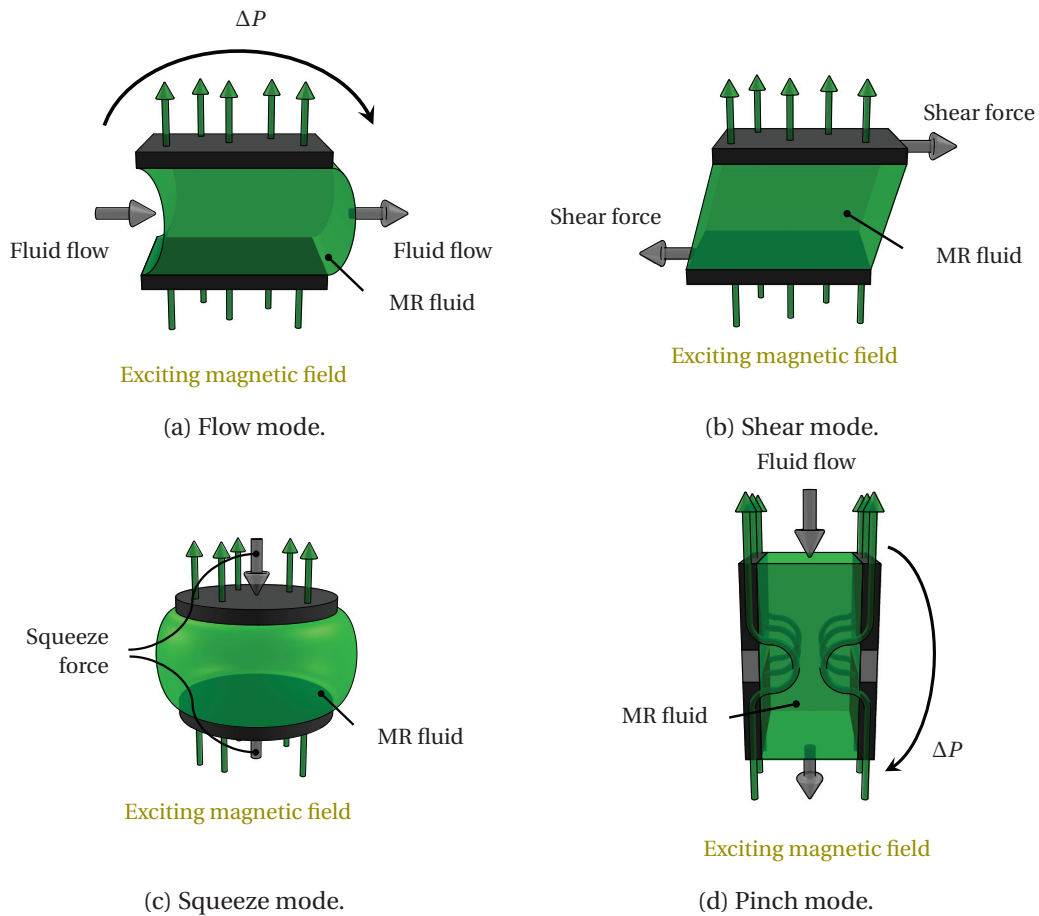


Figure 1.9 – MR fluid operational modes.

As previously introduced, MR valves are substantially based on the flow mode. Although real-life MR valves use mainly annular or radial channels which are quite different from the parallel plated geometry introduced above, the latter still represents the simplest implementation possible of flow mode. Furthermore, if some preliminary hypotheses are validated, Poiseuille's flow (i.e. flow between parallel plates) can be used as a good approximation for the definition of the mathematical expressions describing both annular and radial fluid flow. Mainly for this reason, the following part proposes the main features required to better understand the behaviour and the main features of MR fluid flowing between fixed parallel plates.

For a comprehensive derivation of all the analytical expressions given in the following section, refer to Appendix A.

1.2.3 MR fluid flow between fixed parallel plates

Figure 1.10 depicts the shear stress distribution and velocity profile associated to the Poiseuille's flow of MR fluid [13].

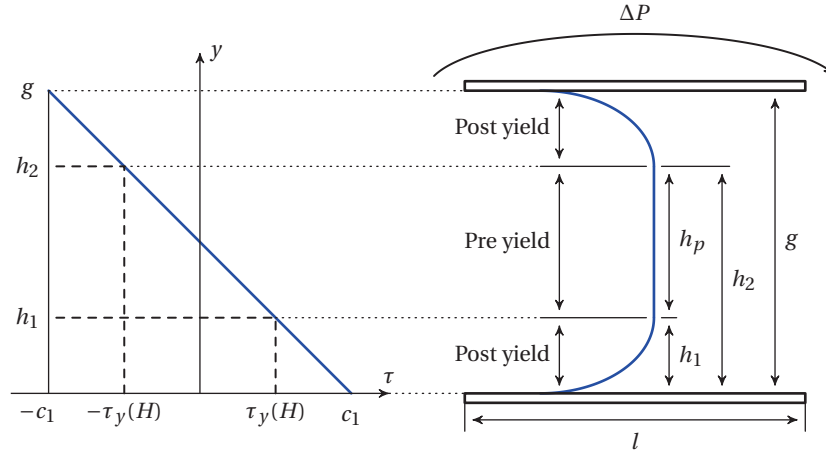


Figure 1.10 – Yield stress distribution and velocity profile for MR fluid flow between two parallel plates.

Although a linear and uniform distribution of the shear stress can be assumed across the total channel width, which is the same case of newtonian fluids, the velocity profile rather assumes a particular shape which is different from the usual parabola proper of newtonian fluids [2]. More in details, an area with a flat velocity profile can be easily individuated in the center of the channel, underlining that in this region the MR fluid form a plug moving at constant velocity [14]. This specific trend can be explained considering that the non-linear characteristic of Bingham fluids given in (1.3) describes two distinct behaviours in relation to the value that the internal shear stress τ assumes with respect to the imposed magnetic field dependent yield stress $\tau_y(H)$. Two different regions can thus be defined

- one *pre-yield* region at the center of the channel, where $\tau \leq |\tau_y|$ and fluid velocity remains constant
- two *post-yield* regions near the walls of the channel, where $\tau > |\tau_y|$ and shear strain rate exists.

The thickness of the central plug region is particularly relevant and directly affects the pressure driven flow of MR fluids. Recalling what is defined in (A.15) we have that

$$h_p = \frac{2l\tau_y}{\Delta P}. \quad (1.8)$$

Consequently, if the fluid yield stress is 0 (no applied magnetic field) the plug thickness h_p reduces to 0 and the velocity profile across the channel assumes the regular newtonian fluids parabolic shape. In this case, the expression of the flow rate given in (A.19) is

$$Q = \frac{\Delta P g^3 w}{12\eta l} \quad (1.9)$$

where w is the width of the planar geometry in Fig. 1.10. On the contrary if the h_p is equal to g , the velocity profile in Fig. 1.10 flattens, suggesting that no flow rate exists. Consequently, combining this two situations and properly rearranging (1.8) and (1.9), it is possible to define the overall pressure drop driven MR fluid flow between two fixed parallel plates as

$$\Delta P = \Delta P_\eta + \Delta P_\tau = \frac{12\eta Q l}{g^3 w} + \frac{2\tau_y(H)l}{g}. \quad (1.10)$$

1.2.4 MR fluid flow through annular and radial channels

As previously introduced, MR valves, but MR devices in general, are commonly axisymmetric. This is related to the advantages that such geometry offers to satisfy the requirements of perpendicularity between fluid flow and magnetic field path. In fact, it is quite simple to build a geometry to drive the magnetic flux radially through an annular channel, or along the symmetry axis through a radial channel (Fig. 1.11).

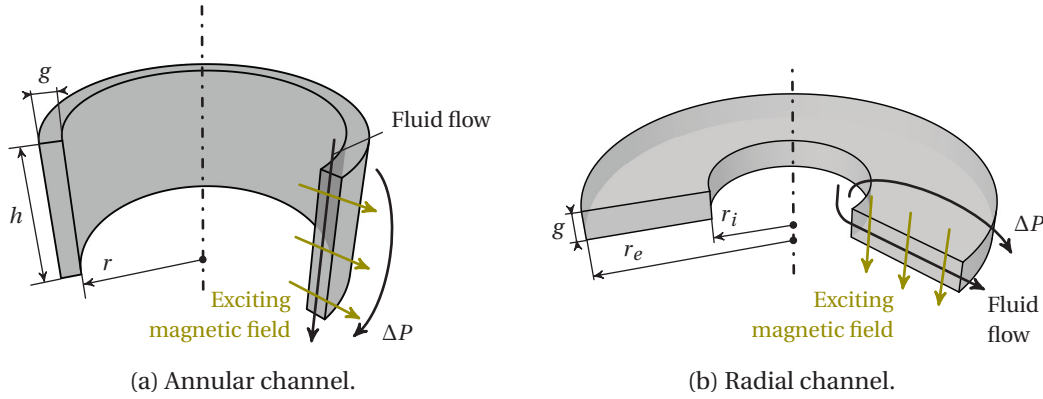


Figure 1.11 – The two main axisymmetric channel geometries considered.

If relation (1.10) is applied to the geometry displayed in Fig. 1.11a (this can be done only in reason of the assumption that $g \ll r$), we obtain the reference relation for the design of MR valves based on the annular channel

$$\Delta P = \Delta P_\eta + \Delta P_\tau = \frac{6\eta Q h}{\pi r g^3} + \frac{2\tau_y(H) h}{g}. \quad (1.11)$$

Moreover, the parallel plate approximation introduced to study the annular channel can be used as a starting point to define the total pressure drop for the radial channel geometry

displayed in Fig. 1.11b. In this case, we can define the pressure gradient as

$$\mathcal{P} \doteq -\frac{dp}{dr} = \frac{\Delta P}{r_e - r_i} \quad (1.12)$$

which, for the same reasons introduced before, gives

$$\Delta P_\tau = \frac{2\tau_y(H)(r_e - r_i)}{g}. \quad (1.13)$$

For what concerns the viscosity dependent pressure drop, we can rewrite (1.9) using the definition of the pressure gradient (1.12) and the equivalence $w = 2\pi r$, to obtain

$$Q = \left(-\frac{dp}{dr}\right) \frac{g^3 2\pi r}{12\eta}. \quad (1.14)$$

Integrating to determine the flow rate, we have

$$Q \int_{r_i}^{r_e} \frac{dr}{r} = - \int_{P_i}^{P_e} \frac{g^3 2\pi r}{12\eta} dp \quad \rightarrow \quad Q = \frac{\Delta P \pi r g^3}{6\eta} \ln\left(\frac{r_e}{r_i}\right) \quad (1.15)$$

and finally

$$\Delta P_\eta = \frac{6\eta Q}{\pi r g^3} \ln\left(\frac{r_e}{r_i}\right). \quad (1.16)$$

Thus, the reference relation for the design of MR valves based on radial configuration is [15]

$$\Delta P = \Delta P_\eta + \Delta P_\tau = \frac{6\eta Q}{\pi r g^3} \ln\left(\frac{r_e}{r_i}\right) + \frac{2\tau_y(H)(r_e - r_i)}{g}. \quad (1.17)$$

1.3 MR valve configurations

This section describes the particular features of the geometries chosen to implement the annular (Fig. 1.12), radial (Fig. 1.13) and annular-radial (Fig. 1.14) valve configurations. In particular, in reason of simplicity and clearness, only the relevant functional parts are schematically presented and auxiliary external supports are not shown.

1.3.1 Annular MR valve

This valve configuration is probably the simplest and, consequently, the most common [17]. Based on the annular channel, the fluid flow never undergoes changes of direction and two *active regions* (i.e. the areas where the fluid crosses the magnetic flux) can be defined. This geometry offers as main features the low complexity, easiness of manufacturing and assembling. Although Fig. 1.12 displays a configuration in which the coil is directly wrapped on the valve central magnetic core, for particular applications and depending on the design

requirements, it can be embedded on the external magnetic core as well.

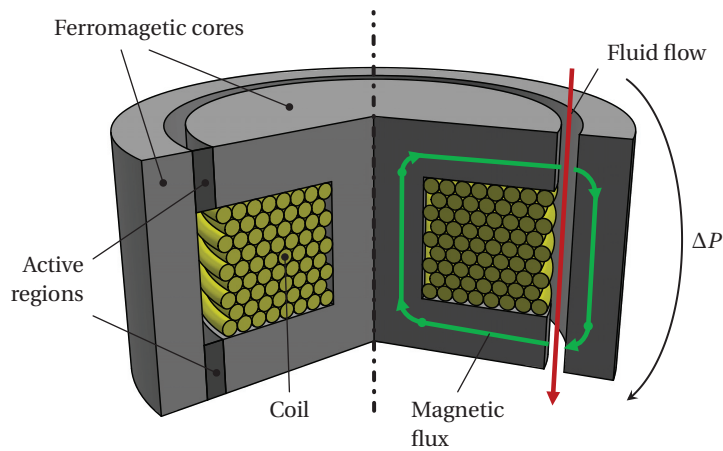


Figure 1.12 – Schematic representation and main elements for the annular MR valve configuration.

1.3.2 Radial MR valve

Because no direct reference of a similar valve geometry has been found in the existing literature, this configuration is firstly presented here and it can be considered, thus, novel.

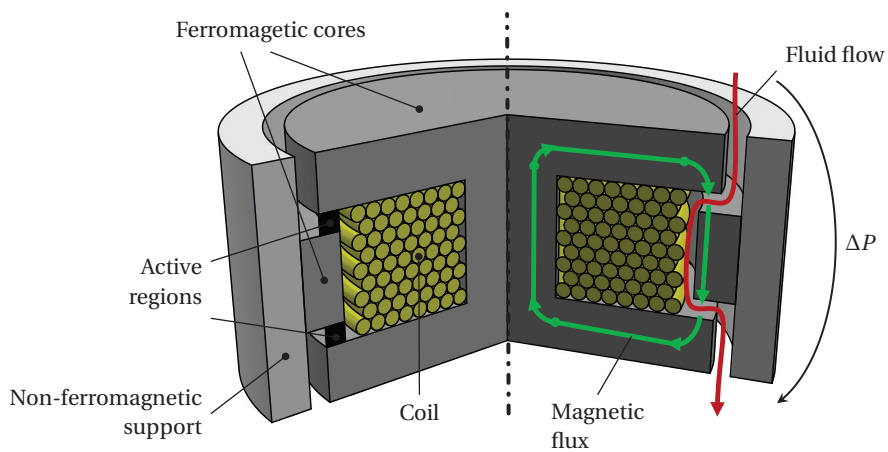


Figure 1.13 – Schematic representation and main elements for the radial MR valve configuration.

As for the annular configuration, two different active regions can be defined (Fig. 1.13). Nevertheless, for this geometry the fluid path is not straight all over and four changes in direction are required to carry it throughout the radial channels. Consequently, further pressure drops due to the fluid friction at the corners have to be considered in the case that high flow rates are expected.

1.3.3 Annular-Radial MR valve

The last configuration evaluated is the annular-radial valve (Fig. 1.14) [18]. This geometry consists of a total of four active regions, obtained with two annular and two radial channels. Some recent studies have been done concerning the design and modelling of this configuration which can be considered relatively new.

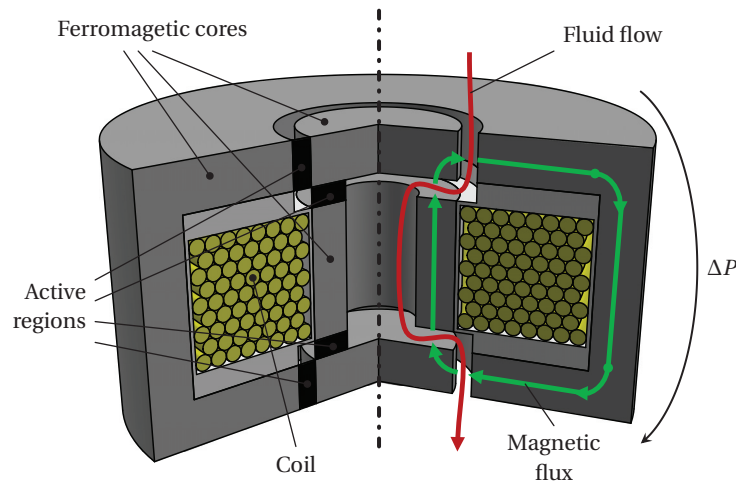


Figure 1.14 – Schematic representation and main elements for the annular-radial MR valve configuration.

As for the radial geometry, the fluid path have to be redirected four times in order to flow through both the annular and radial channels. Contrarily with respect to the two configurations introduced before, for the annular-radial valve the coil is located externally with respect to the active regions, mainly to improve the easiness of assembling. Concerning this last point, this geometry offers more challenges in its mounting. For example, the central magnetic core results to be "floating" in the schematic representation of Fig. 1.14. This suggests that some internal supports have to be inserted to fasten the constituting parts among them, increasing the structure complexity in the manufacturing and assembling processes.

1.4 Extension to generic MR-based devices

Although the functions that the different existing MR devices realise are different (i.e. pressure drops and flow rate control for MR valves, torque and rotational speed regulation for MR brakes and clutches, damping force and linear velocity control for MR shock absorbers), they have many aspects in common [19].

First of all, they can be generally classified as power dissipating devices. In fact, they are not able to perform real work (i.e. no displacement occurs when they are activated) and they are in this sense considered passive systems.

Moreover, all common MR devices are based on an axisymmetric structure. This is mainly due to the advantages in the realisation and integration of the different required functions

Chapter 1. Introduction

(shaping of the magnetic field and fluid flow, easiness of manufacturing and assembling, ...) that such a geometry offers.

Last, but not least, the same main constitutive elements can be found in the different devices families. For example, it can be noted that the core element of the basic damper structure displayed in Fig. 1.15a is represented by the MR annular configuration described in Fig. 1.12. Similarly, the MR disc brake geometry shown in Fig. 1.15b has been used as a source of inspiration for the conception of the MR radial valve discussed before.

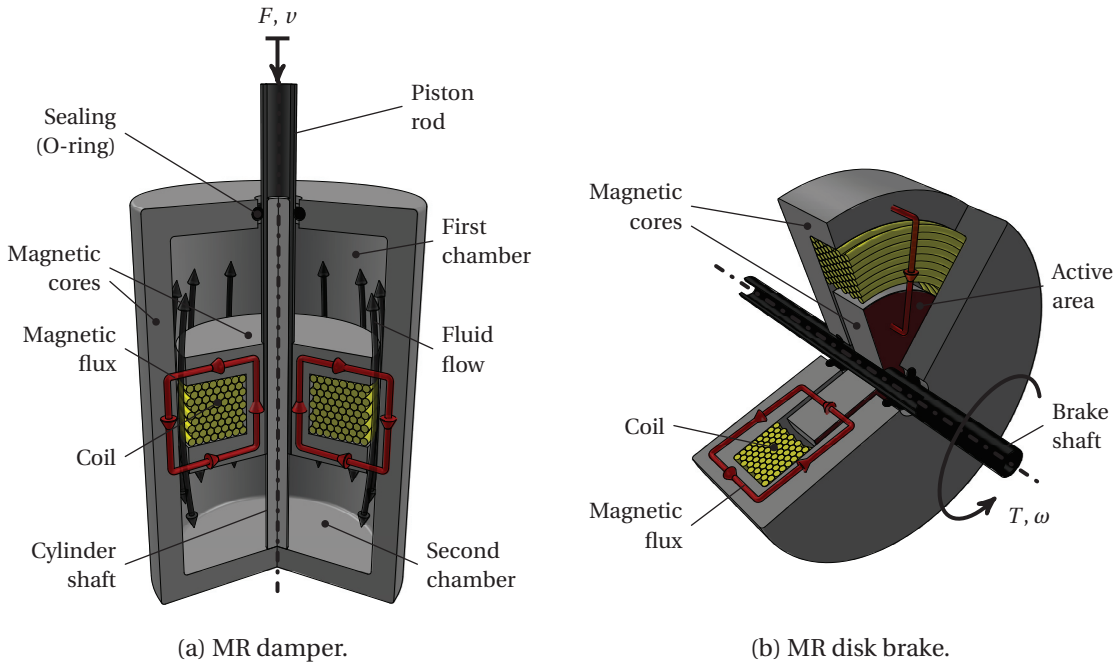


Figure 1.15 – The two basic configurations of the main MR devices other than MR valves.

This last consideration becomes even more evident if the basic constitutive equations defining each device are compared. In fact, for a common shock absorber configuration, we have that the damping force achievable can be expressed as [20, 21]

$$F = F_{\eta} + F_{\tau} = \frac{\eta S_{MR} v}{g} + \tau_y(H) S_{MR} \quad (1.18)$$

where S_{MR} represents the active surfaces (i.e. the surface on which the fluid and the magnetic flux cross orthogonally), v is the piston rod linear velocity and g is the gap in which the fluid flows from the first to the second chamber. If a MR disc brake is considered, we have that the overall braking torque can be expressed as [22, 23]

$$T = T_{\eta} + T_{\tau} = \frac{\eta S_{MR} \omega}{g} r_{disc}^2 + \frac{4}{3} \tau_y(H) S_{MR} r_{disc} \quad (1.19)$$

where ω is the angular velocity, r_{disc} is the external radius of the rotating disc and g is the thickness of the MR fluid layer of the active surface. It is well evident how (1.18) and (1.19) are

slightly different from the equations defining the total pressure drop for the annular, radial and annular-radial valves. This is easily justified considering that the basis phenomenon on which all MR devices are based is the same.

Consequently, because of all the mentioned reasons, the analytical approaches proposed, the considerations done and most of the outcomes obtained throughout the following chapters, which are focused on MR valves, can be easily and directly extended to all MR-based devices in general.

1.5 Content of the thesis

After the preliminary introduction given so far, chapter 2 will focus on the development of an improved equivalent magnetic modelling of MR valves, called High Fidelity Magnetic Equivalent Modelling (HFMEC), which can be generalised to all axisymmetric magnetic devices. The advantages of employing this method, which results to be low time consuming and easy to be implemented, are comprehensively discussed and validated comparing the model results with Finite Element Analysis outcomes.

Successively, chapter 3 will more specifically address the design and the comparison of the different MR valves configurations introduced in section 1.3. More in details, each of the studied valve topology is comprehensively analysed and the basic geometric relations required to constraint the design of each structure, both from the hydraulic and from the electromagnetic point of view, are defined. The set of design equations corresponding to the different valves configurations can be then solved for a specific given design scenario. In particular, the HFMEC developed in chapter 2 is used as the main tool to analyse and solve the magnetic circuit associated to the different valve topologies. In this respect, the development discussed do not only provide an analysis tool, but it is used to build a complete design routine. Last but not least, the different configurations addressed will be compared in terms of different defined figures of merit in order to give some further rules and hints for the design of MR valves.

Chapter 4 will then address the dynamic modelling of MR valves considering the annular configuration as the preferred geometry of reference. In particular, this topic will be developed using the Bond graph modelling technique that allows to address multi-physics systems in a relatively simple and well organised way while underlining the power exchanges of the different elements constituting the system under study. The work conducted with this particular modelling approach has brought out the feasibility to detect pressure or flow variations on MR valves by mean of magnetic flux analysis. In order to clarify the real presence of the expected phenomenon, test sessions on a manufactured MR annular valve are conducted with success and the potentialities of this sensing possibility, discussed here for the first time and which can be generalised to each MR-based system, are presented.

The design and modelling considerations introduced in the previous chapters will converge in chapter 5 and they will be used for the development of miniature soft MR shock absorbers to be embedded in a smart footwear. Considering that this final application is particularly intended

Chapter 1. Introduction

for diabetic patients with a high risk or a previous history of foot plantar ulcerations and foot neuropathy, an initial introduction of this disease is done, mainly with the aim to describe the correct background to define the system requirements. Successively, the decisional path which has carried to the definition of the final solution is described together with the expected advantages. The designed and manufactured miniature shock absorbers are finally tested to assess their reliability and the fulfilment of the imposed system requirements.

The research activities and the related results presented in this thesis do not pretend to definitely clarify and fix all points still open to question concerning MR systems. The final goal of this work is rather to provide some further elements and concepts to improve the design and modelling of MR-based devices.

Publications related to this chapter:

- D. Grivon, Y. Civet, Z. Pataky and Y. Perriard, *Bingham-Papanastasiou and Approximate Parallel Plates Models Comparison for the Design of Magneto-Rheological Valves*, *Advanced Intelligent Mechatronics (AIM)*, 2014 IEEE/ASME International Conference on, pp. 168-173, 2014.

Bibliography

- [1] H. A. Barnes, J. F. Hutton and F. R. S. Walters, *An Introduction to Rheology*, Elsevier Science Publisher, Third Impression, 1993.
- [2] F. M. White, *Fluid Mechanics - Seventh Edition*, McGraw-Hill Series in Mechanical Engineering, 2010.
- [3] L. Vékás, *Ferrofluids and Magnetorheological Fluids*, Advanced in Science and Technology, Vol. 54, pp. 127-136, 2008.
- [4] P. P. Phulé, *Magnetorheological (MR) Fluids: principles and applications*, Smart Materials Bulletin, Issue 2, pp. 7-10, 2001.
- [5] D. J. Klingenberg, F. van Swol, C. F. Zukosky, *Dynamic simulation of electrorheological suspensions*, Journal of Chemistry and Physics, No. 91, pp. 7888-7895, 1989.
- [6] Lord Corporation, Available online at <http://www.lord.com/>
- [7] A. Sihvola, *Electromagnetic mixing formulas and applications*, IEEE Electromagnetic Waves Series, vol. 47, pp. 63-68, 1999.
- [8] T. C. Hales, *A review of the Kepler conjecture*, Cornell University Library, May 2002.
- [9] I. A. Frigaard, C. Nouar, *On the usage of viscosity regularization methods for visco-plastic fluid flow computation*, Journal of Non-Newtonian Fluid Mechanics, No. 127, pp. 1-25, 2005.
- [10] T. C. Papanastasiou, *Flow of Materials with Yield*, Journal of Rheology, N. 31, pp. 385-404, 1987.
- [11] A. G. Olabi, A. Grunwald, *Design and application of magneto-rheological fluid*, Materials and Design, Vol. 28, Issue, 10, pp. 2658-2664, 2007.
- [12] F. D. Goncalves, J. D. Carlson, *An alternate operation mode for MR fluids - Magnetic Gradient Pinch*, Journal of Physics: Conference Series, No. 149, 2009.
- [13] N. M. Wereley and L. Pang, *Nondimensional analysis of semi-active electrorheological and magnetorheological dampers using the parallel plate models*, Smart Materials and Structures, No. 7, pp. 732-743, 1998.

Bibliography

- [14] R. W. Phillips, *Engineering Application of fluids with variable yield stress*, PhD Thesis, University of California, Berkeley, 1969.
- [15] G. Dai and R. Biron Bird, *Radial flow of a Bingham fluid between two fixed circular disks*, *Journal of Non-Newtonian Fluid Mechanics*, 8, pp. 349-355, 1981.
- [16] W. Li and H. Du, *Design and experimental evaluation of a magnetorheological brake*, *International Journal of Advanced Manufacturing Technology*, vol. 21, no. 7, pp. 508-515, 2003.
- [17] A. Grunwald and A. G. Olabi *Design of a magneto-rheological (MR) valve*. *Sensors and Actuators A*, No. 148, pp. 211-223, 2008.
- [18] H. X. Ai, D. H. Wang and W. H. Liao, *Design and Modelling of a Magnetorheological Valve with Both Annular and Radial Fluid paths*, *Journal of Intelligent Smart Material and Structures*, Vol. 17, April 2006.
- [19] M. R. Jolly, J. W. Bender, J. D. Carlson, *Properties and Applications of Commercial Magneto-Rheological Fluids*, SPIE 5th Symposium on Smart Structures and Materials, San Diego, CA, 15 March, 1998.
- [20] X. Zhang, W. Li, Y. Zhou, *A Variable Stiffness MR Damper for Vibration Suppression*, IEEE/ASME International Conference on Advanced and Intelligent Mechatronics, pp. 106-111, 2009.
- [21] G. Savioz, V. Ruchet, Y. Perriard, *Study of a Miniature Magnetorheological Fluid Actuator for Haptic Devices*, *Advanced Intelligent Mechatronics (AIM)*, International Conference on, pp. 1197-1202, 2010.
- [22] D. Senkal, H. Gurocak, *Compact MR-Brake with Serpentine Flux Path for Haptic Applications*, *EuroHaptics Conference and Symposium on Haptic Interfaces for Virtual Environment and Teleoperator Systems*, pp. 91-96, 2009.
- [23] X. Xu, C. Zeng, *Design of a Magneto-rheological Fluid Clutch Based on Electromagnetic Finite Element Analysis*, *International Conference on Computer Engineering and Technology*, Vol. 5, pp. 182-185, 2010.

2 High Fidelity Magnetic Equivalent Circuit for Axisymmetric Devices

The following chapter presents a reliable, accurate and computationally inexpensive design tool for magnetic modelling of axisymmetric electromagnetic devices, in which geometries commonly employed to build MR systems are included.

A novel semi-empirical Finite Element-based model for the computation of arc-shaped fringing fluxes occurring in axisymmetric geometries is introduced. If compared to existing approaches, the proposed method demonstrates to significantly reduce the error in the estimation of axisymmetric arc-shaped fringing permeances. The developed formulations have been used to extend traditional Magnetic Equivalent Circuits (MECs) for the three different configurations of MR valves introduced in section 1.3 to High-Fidelity Magnetic Equivalent Circuits (HFMECs) in order to take in consideration fringing and leakage fluxes and improve the overall magnetic models accuracy.

In order to prove the reliability of the introduced approach, the magnetic inductions B_{MR} crossing the MR fluid through the valves channels are computed solving the MECs and the improved HFMECs and they are then compared with Finite Element Analysis (FEA) results.

2.1 Introduction

Magnetic Equivalent Circuits (MECs) represent a tool commonly used in the initial dimensioning of electromagnetic devices [1, 2]. Magnetic permeances (or reluctances) associated with basic geometric elements of ferromagnetic cores used to drive the magnetic flux towards the desired air-gaps can be obtained using well-known and exact analytical expressions. Consequently, permeances networks can be built to model both the ferromagnetic cores and the most relevant air-gaps in the considered electromagnetic devices. Successively, the obtained equivalent circuits can be easily implemented on common analytical solvers. In particular, such approach results to be computationally inexpensive and low time consuming even in the case in which material non-linearities are taken into account and iterative solvers are employed. Furthermore, the derived models describe the influence that each geometrical parameter has on the final design, which represents a particularly useful information during the first dimensioning of a system [3]. Nevertheless, this modelling methodology seldom takes in consideration fringing and leakage fluxes which, depending on the particular geometry and features of the system under study, may have a huge impact in the determination of the relevant magnetic quantities.

On the contrary, Finite Element (FE) modelling actually represents the most accurate way to describe real systems and, consequently, magnetic devices. In spite of that, to precisely estimate the physical quantities of interest without the risk of rough errors, fine meshing is often required, in particular for miniaturised systems, resulting in high computational costs. Besides, considering that FE models do not explicitly define the relations between geometrical parameters and the system behaviour, such inconvenience becomes even more relevant in the case that multiple FE analyses are performed to build a sufficiently vast domain of experience to assess the influence of physical dimensions on a particular or initial design, which is the case in a feasibility study. A similar situation occurs if FE simulations are inserted in an optimisation routine for which the scope of the relevant parameters is too large and not well-defined. In this respect, improving magnetic equivalent circuits and consider leakage and fringing phenomena can represent a solution to approach the quality of FE analysis still remaining computationally inexpensive [4].

Modelling of magnetic field fringes occurring at the transition of magnetic domains with different relative permeability has been widely addressed for what concerns planar devices, both analytically or using semi-empirical FE-based models, the main difference being related to the approximations used to describe the magnetic field lines path. In the case of planar geometries, Roters [5] firstly proposed an analytical model to determine fringing permeances associated with air-gaps approximating the magnetic field paths with quarter-circles and straight lines, which led to the following definition of fringing permeance

$$\Lambda_{Rot} = \frac{\mu_0 \mu_r L}{\pi} \cdot \ln\left(1 + \frac{\pi X}{g}\right) \quad (2.1)$$

where μ_0 is the absolute vacuum permeability, μ_r is the relative permeability of the medium

crossed by the magnetic field lines, L is the depth of the geometry considered and X is the radius of the outer fringes taken into account [6].

A similar approximation has been used by Batdorff et al. [7] to include fringing phenomena in the magnetic modelling of axisymmetric electromagnetic actuators and obtain a High Fidelity Magnetic Equivalent Circuit (HFMEC). Nevertheless, considering the non-closed form solution of the integral required to exactly compute the fringing permeances for non-planar geometries, they provided an analytical solution obtained through a linearisation of the function to be integrated. Furthermore, the approach introduced by Batdorff cannot be easily applied to systems in which, for example, fringes cross magnetic domains with a different permeability, which is the case of the MR devices.

To overcome such limitations, section 2.2 proposes a semi-empirical FE-based definition of the fringing permeances associated with the quarter-circles describing the magnetic field lines distribution at the interface of magnetic domains with different relative permeability. Successively, section 2.3 introduces the computation of the permeances required to build the MECs and the ones required to extend the latter to HFMECs. Finally, section 2.4 presents the resulting magnetic inductions in the valves channels obtained solving the associated MECs and HFMECs and these values are compared with results from FE simulations to define the reliability of the proposed approach.

2.2 Finte Element Based semi-empirical modelling

As previously introduced the most intuitive way to represent fringes path is by mean of quarter-circles and straight lines. Figure 2.1 depicts the result of using such approximation to describe fringes originating at the interface of an annular air-gap.

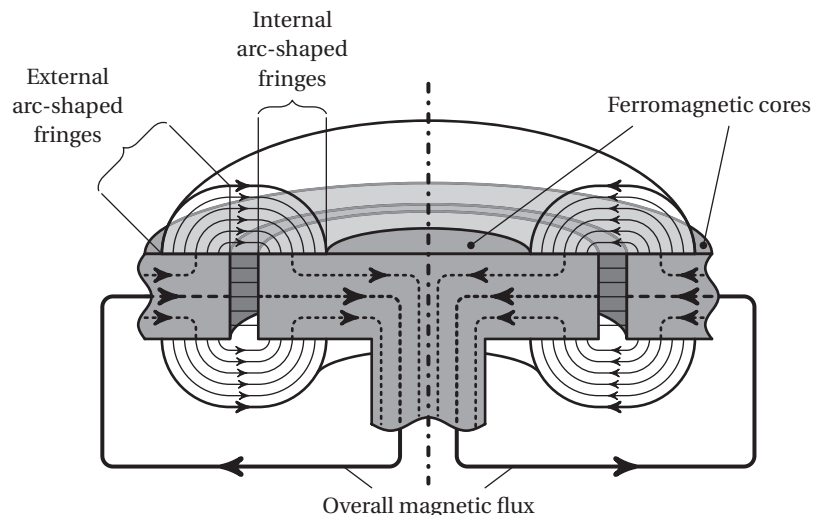


Figure 2.1 – Cross-sectional schematic representation of the fringes approximation in the case of an annular air gap.

Chapter 2. High Fidelity Magnetic Equivalent Circuit for Axisymmetric Devices

The tridimensional geometries obtained through the revolution of the aforementioned approximated paths describe the flux tubes for which determine the fringing permeances of interest. In particular, the latter can be split in 3 different elementary parts which can be combined successively to obtain the overall fringing permeances:

- internal fringing permeance Λ_{int} associated to internal arc-shaped fringes
- external fringing permeance Λ_{ext} associated to external arc-shaped fringes
- cylinder or disc permeances located inbetween the aforementioned ones in case the magnetic field direction develops respectively axially or radially.

Although analytical formulations exist for the computation of cylinder and disc permeances, it is not the case for permeances Λ_{int} and Λ_{ext} . A novel approach for their determination is presented hereinafter.

If only the arc-shaped parts of the overall fringes are addressed, infinitesimal flux tubes associated with quarter-circles magnetic field lines result in quarters of hollow toroids (Fig. 2.2).

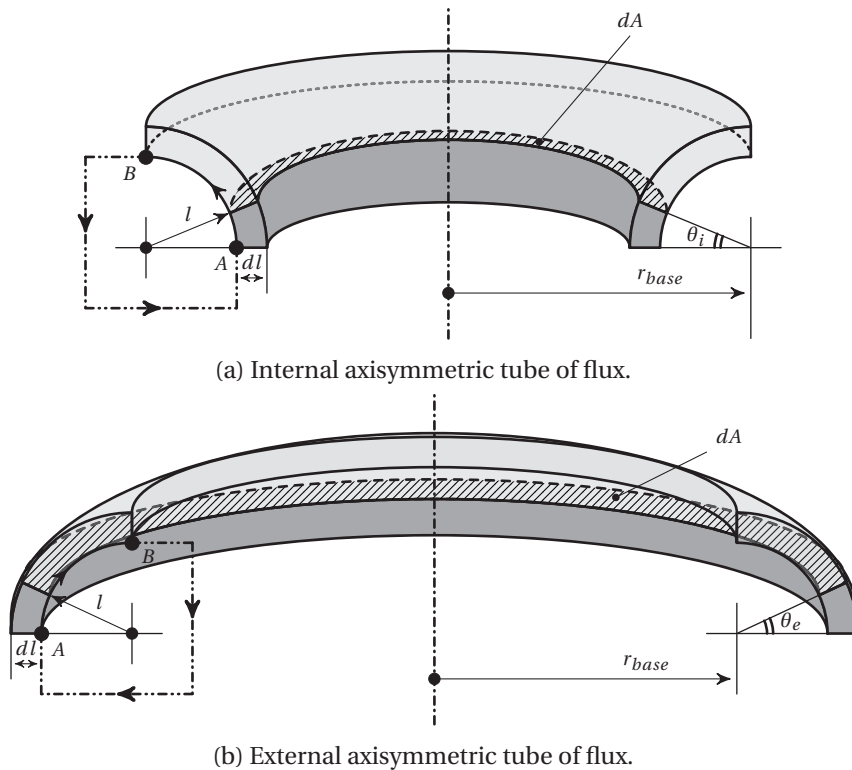


Figure 2.2 – Cross-sectional representation of infinitesimal quarter of hollow toroids for the flux tubes associated with internal and external arc-shaped fringes.

In the following treatment, the magnetic potential drop associated with the dashed lines

2.2. Finte Element Based semi-empirical modelling

connecting points A and B in Fig. 2.2a and 2.2b is neglected and only the shadowed geometries will be addressed.

The permeance of a flux tube on which a magnetic potential Θ_{AB} is imposed can be expressed as [7]

$$\Lambda_{AB} = \mu_0 \mu_r \int_A \frac{dA}{l_{AB}} = \frac{\phi}{\Theta_{AB}} \quad (2.2)$$

where l_{AB} is the length of the magnetic field lines orthogonal to the infinitesimal area elements dA and ϕ is the magnetic flux circulating in the flux tube. If this definition is applied to geometries described in Fig. 2.2a and 2.2b, we have respectively

$$\begin{aligned} \Lambda_{int} &= \mu_0 \mu_r \int_0^{\pi/2} \int_{L_i}^{L_o} \frac{dA}{l_{AB}} = \\ &= \mu_0 \mu_r \int_0^{\pi/2} \int_{L_i}^{L_o} \frac{2\pi [r_{base} - l \cos(\theta_i)]}{\theta l} dl d\theta \end{aligned} \quad (2.3)$$

$$\begin{aligned} \Lambda_{ext} &= \mu_0 \mu_r \int_0^{\pi/2} \int_{L_i}^{L_o} \frac{dA}{l_{AB}} = \\ &= \mu_0 \mu_r \int_0^{\pi/2} \int_{L_i}^{L_o} \frac{2\pi [r_{base} + l \cos(\theta_e)]}{\theta l} dl d\theta. \end{aligned} \quad (2.4)$$

where L_i and L_o define respectively the inner and outer radii of the complete tube of flux intended to represent the overall fringing phenomenon considered.

Unfortunately, as previously introduced, such integrals are improper and do not have a converging solution.

To solve such problem, Batdorff et al. [7] proposed a partial linearization of the function to be integrated. Differently, because of the width of the integration intervals, the presented approach proposes rather the approximation of the functions to be integrated with simpler ones based on the definition of an optimal area $A(\theta^*)$. The parameter θ^* represents the optimal angle (which can be either internal or external) for which the approximated integrals better fit the exact value of the permeances associated with the tubes of flux previously described.

Considering the introduced approximation, (2.3) and (2.4) simplify in

$$\begin{aligned}\Lambda_{int} &= 4\mu_0\mu_r \int_{L_i}^{L_o} \left[\frac{r_{base}}{l} - \cos(\theta_i^*) \right] dl = \\ &= 4\mu_0\mu_r \left[\underbrace{r_{base} \cdot \ln\left(\frac{L_o}{L_i}\right)}_{\Lambda_A} - \underbrace{(L_o - L_i) \cos(\theta_i^*)}_{\Lambda_B} \right]\end{aligned}\quad (2.5)$$

$$\begin{aligned}\Lambda_{ext} &= 4\mu_0\mu_r \int_{L_i}^{L_o} \left[\frac{r_{base}}{l} + \cos(\theta_e^*) \right] dl = \\ &= 4\mu_0\mu_r \left[\underbrace{r_{base} \cdot \ln\left(\frac{L_o}{L_i}\right)}_{\Lambda_A} + \underbrace{(L_o - L_i) \cos(\theta_e^*)}_{\Lambda_B} \right].\end{aligned}\quad (2.6)$$

In order to find an optimal value of θ^* , the infinitesimal permeances $d\Lambda$ associated with the quarter-circles defined in Fig. (2.2) are modeled in a FE software and analyses are successively conducted varying the geometrical dependent parameters r_{base} and l to obtain a relevant domain of experience. A non-linear regression algorithm is used to define the value of θ^* for which (2.5) and (2.6) better fit the FE results. The two values of the optimal angles found are reported in the table hereafter.

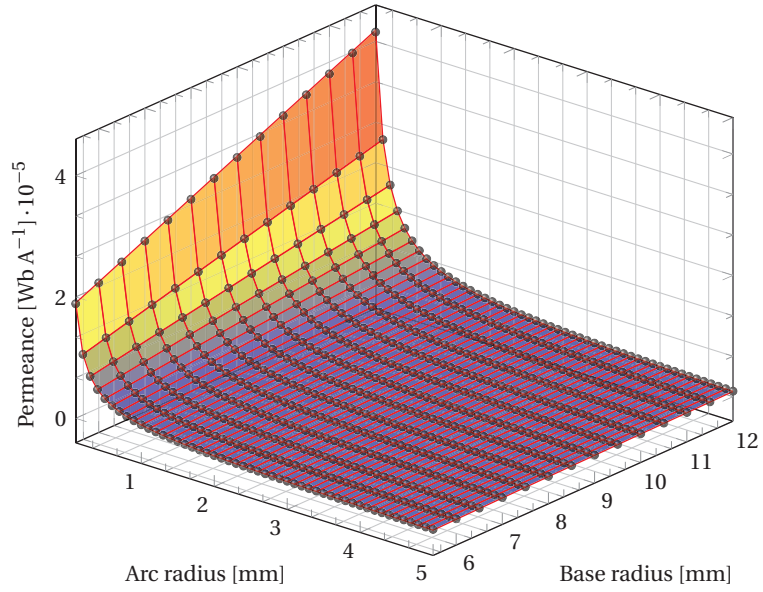
θ_i^*	θ_e^*
55,04°	43,46°

Table 2.1 – Optimal angles θ_i^* and θ_e^* .

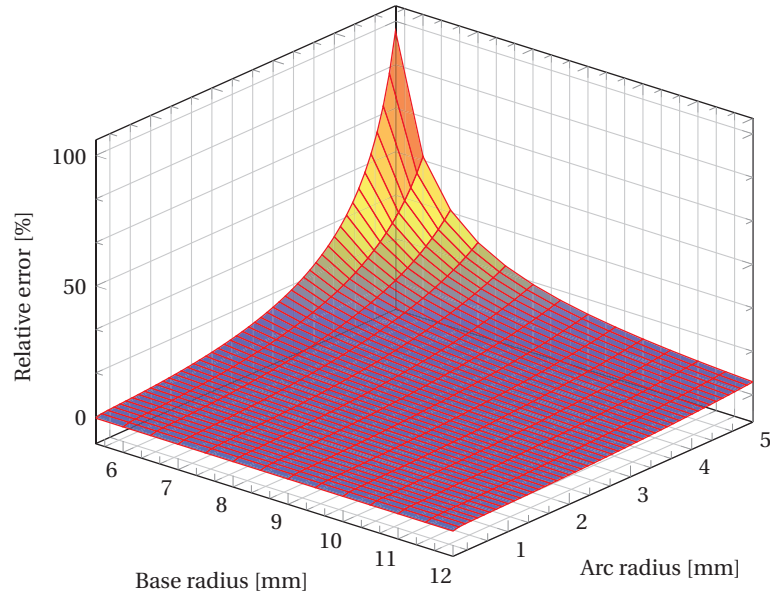
Figures 2.3 and 2.4 depict the fitting of the proposed model with respect to the FE analysis results and the corresponding relative errors. If Fig. 2.3a and 2.4a are evaluated, it can be noted that the proposed relations (represented with black circles) well fit the trend defined by FE results (color scaled surface) over the whole domain considered. Furthermore, the linear dependence of the permeances with the base radius r_{base} is well evident, which is quite straightforward considering that the introduced formulae result to be revolution integrals. On the contrary, if the corresponding relative errors are addressed (Fig. 2.3b and 2.4b), it can be seen that the quality of the introduced models decreases the more the base radius r_{base} reduces and the radius of the considered arc fringes l increases.

In particular, Fig. 2.3b suggests that the proposed approximations are no more valid for the estimation of infinitesimal arc-shaped permeances originating nearby (or even at) the symmetry axis of the considered geometries (the displayed relative error at this point reaches 100%). This result can be explained considering that, as this condition is reached, the areas crossed by the magnetic flux at $\theta_i = 0$ and for $\theta_i = \pi/2$ are highly different. Consequently, the value of the optimal angle θ_i^* previously defined (well matching situations where areas for $\theta_i = 0$ and for $\theta_i = \pi/2$ are slightly different) appears to be wrong.

Figure 2.3b underlines that, although all the considerations previously discussed for the estimation of $d\Lambda_{int}$ can be equally applied for the the external infinitesimal permeances, the



(a) Proposed model (black circles) Vs FE analysis fitting.

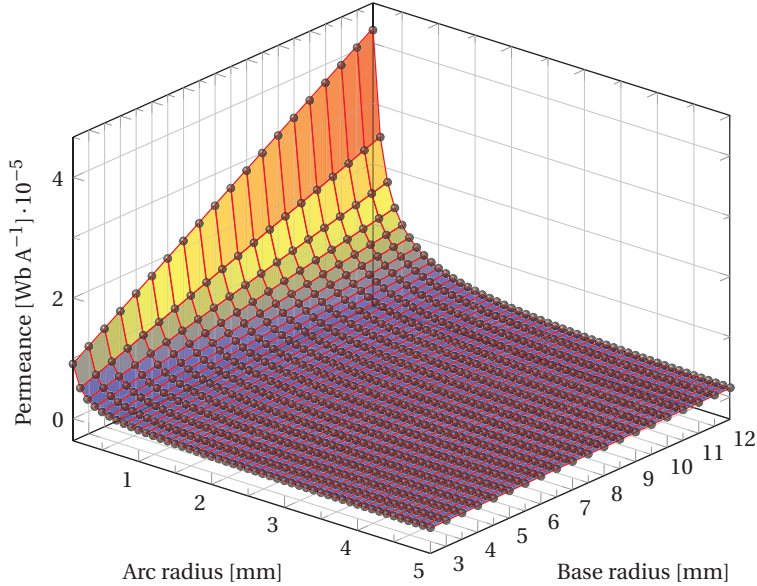


(b) Corresponding relative errors.

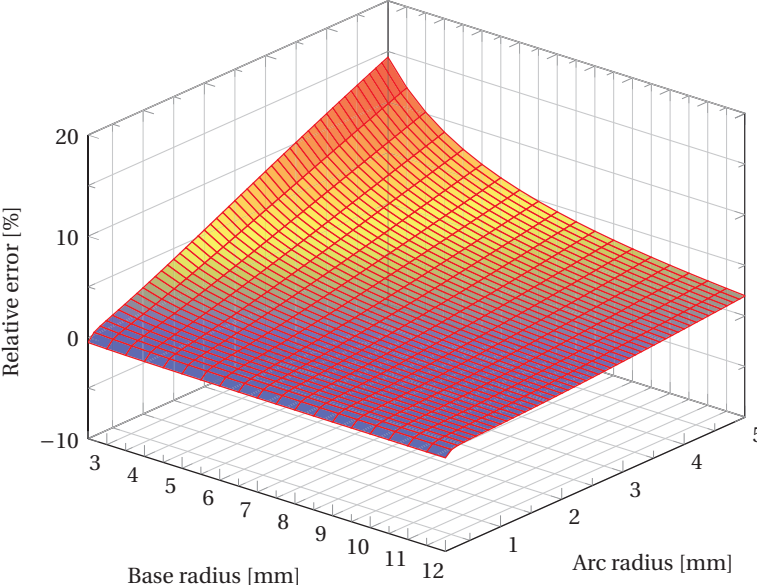
Figure 2.3 – Infinitesimal internal arc-shaped permeances $d\Lambda_{int}$.

approximation used to determine $d\Lambda_{ext}$ exhibits an overall higher quality and lower mean error. This is due to the fact that the more both r_{base} and l increase the more the areas crossed by the magnetic flux for $\theta_e = 0$ and for $\theta_e = \pi/2$ are similar and they approach to the optimal area defined by θ_e^* .

Moreover, considering that Fig. 2.3a and 2.4a shows the infinitesimal contributions rather than the overall permeances and that the corresponding relative errors are higher where $d\Lambda_{int}$ and $d\Lambda_{ext}$ assume the lowest values (almost one degree of magnitude lower than the maximum



(a) Proposed model (black circles) Vs FE analysis fitting.



(b) Corresponding relative errors.

Figure 2.4 – Infinitesimal external arc-shaped permeances $d\Lambda_{ext}$.

values obtained when $l \rightarrow 0$) the large relative error depicted is remarkably smoothed in the computation of the overall permeances Λ_{int} and Λ_{ext} , which strengthens the validity of the proposed modelling.

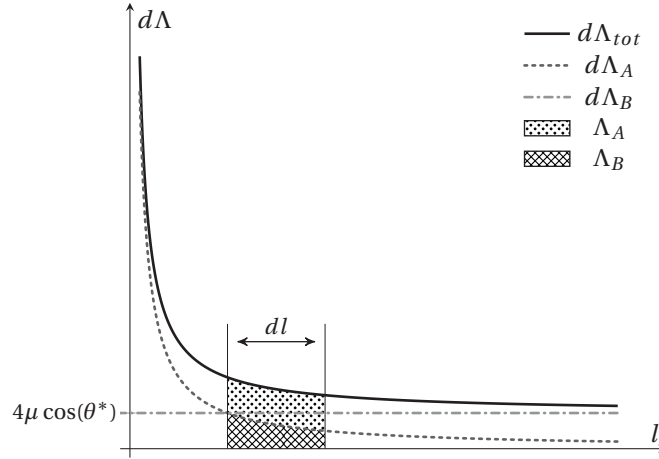


Figure 2.5 – Graphical representation of the contribution of the infinitesimal permeances $d\Lambda_A$ and $d\Lambda_B$.

The last introduced relations (2.5) and (2.6) are still associated with an improper integral, not converging for $L_i = 0$. In order to overcome this problem, it can be noted that the contribution of the term Λ_B in (2.5) and (2.6) becomes the more negligible, with respect to Λ_A , the more $L_i \rightarrow 0$, as shown in Fig. 2.5. The computation of the fringing permeance in such case is analogous to the situation described by Roters [5]. In fact, for $L_i \rightarrow 0$ it results that

$$\pi[(r_{base} + L^*)^2 - r_{base}^2] = \pi(2r_{base}L^* + L^{*2}) \approx 2\pi r_{base}L^* \quad (2.7)$$

which underlines that the area crossed by the magnetic field lines remains constant for the overall magnetic path length considered, with $\theta_{i,e} = [0, \pi/4]$. In particular, L^* defines the outer radius of the arc fringing permeance for which Λ_B becomes negligible. This threshold is considered achieved when $d\Lambda_B = d\Lambda_A \cdot 10^{-2}$, obtaining from relations (2.5) or (2.6)

$$L^* = \lim_{dl \rightarrow 0^+} \left[\frac{dl}{\exp\left(\frac{\cos(\theta^*) dl}{r_{base}}\right)} \right] \cdot 10^{-2} = \lim_{dl \rightarrow 0^+} \left[\frac{1}{\frac{\beta}{r_{base}} \exp\left(\frac{\cos(\theta^*) dl}{r_{base}}\right)} \right] \cdot 10^{-2} = \frac{r_{base}}{\cos(\theta^*)} \cdot 10^{-2}. \quad (2.8)$$

Consequently, it can be addressed with the same approach introduced by Roters [5], according to which the series of permeances associated with two quarters-circles and one straight line is computed as

$$\Lambda_{Rot} = 2\mu_0\mu_r r_{base} \ln\left(1 + \frac{\pi L^*}{g}\right) \quad (2.9)$$

where g is the air gap for which the fringing phenomenon occurs.

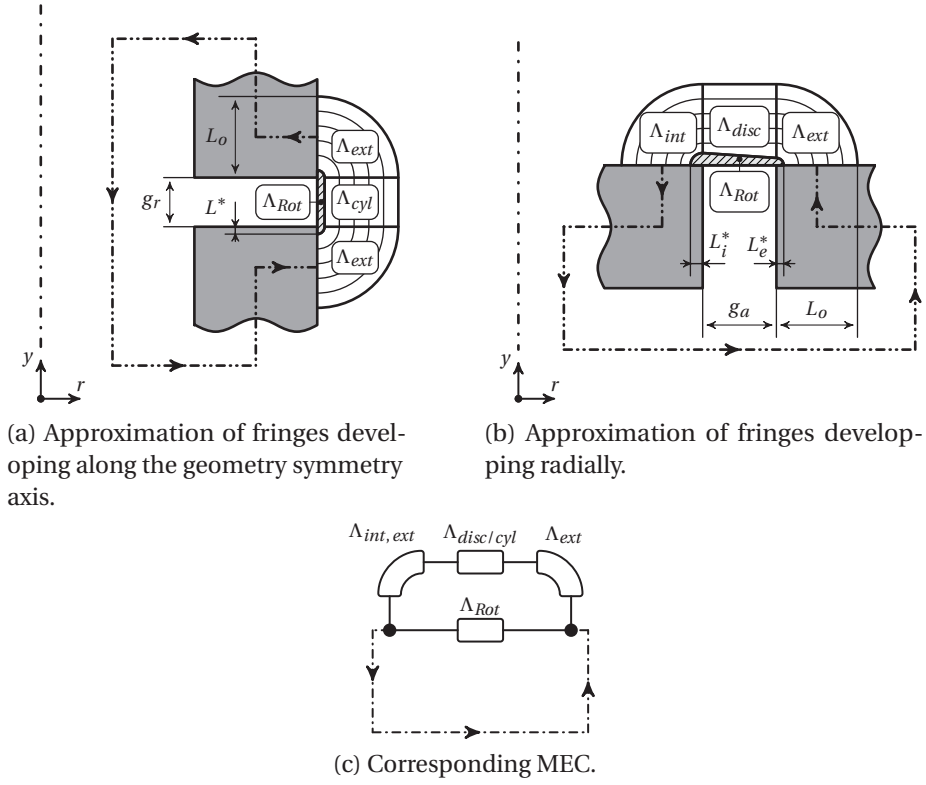


Figure 2.6 – Graphical representations of the different permeances contributions to model fringes originating at magnetic domains interfaces.

Figure 2.6a shows a schematic representation used to describe a typical situation for which fringing originates at the interface between a ferromagnetic region and an air gap along the axial direction. Nevertheless, although the introduced approach is correct for the computation of Λ_{tot} for the situation depicted in Fig. 2.6a, if the fringing permeance develops radially, as presented in Fig. 2.6b, some further considerations on the permeance geometric boundaries have to be introduced to extend the validity of the proposed approach. In fact, the computation of the permeance Λ_{Rot} given in (2.9) assumes that the flux of tube area does not change along the magnetic path. To maintain this condition, it results that the parameters L_i^* and L_e^* depicted in Fig. 2.6b have to be related as follows

$$L_e^* = \frac{L_i^* r_g}{(r_g + g_a)}. \quad (2.10)$$

In this case, illustrated in Fig. 2.7, the permeance of a disc with a thickness $h(r)$ varying proportionally with its radius can be found considering the definition of reluctance

$$\mathcal{R}_{disc.var.} = \int_{r_i}^{r_o} \frac{1}{2\pi\mu_0\mu_r r h(r)} dr = \int_{r_i}^{r_o} \frac{1}{2\pi\mu_0\mu_r [h_0 + \omega r] r} dr \quad (2.11)$$

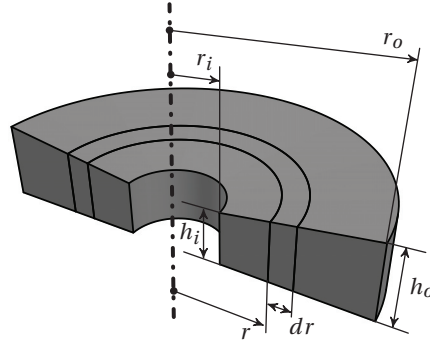


Figure 2.7 – Disc geometry with a thickness increasing proportionally with its radius.

and considering that ϖ is the coefficient defining the slope of the non horizontal disc side defined as

$$\varpi = \frac{h_o - h_i}{r_o + r_i} \quad (2.12)$$

we have that (2.11) reduces to

$$\mathcal{R}^{disc. var.} = \frac{1}{2\pi\mu_0\mu_r} \ln\left(\frac{r_o h_i}{r_i h_o}\right) \quad (2.13)$$

and consequently

$$\Lambda^{disc. var.} = \frac{2\pi\mu_0\mu_r}{\ln\left(\frac{r_o h_i}{r_i h_o}\right)}. \quad (2.14)$$

Finally, for both the considered cases, the MEC modelling the permeances described in Fig. 2.6a and 2.6b is the same and it is represented in Fig. 2.6c. Thus, the overall fringing permeance illustrated can be computed as

$$\Lambda_{tot} = \Lambda_{Rot} + \left(\frac{1}{\Lambda_{int, ext}} + \frac{1}{\Lambda_{disc/cyl}} + \frac{1}{\Lambda_{ext}} \right)^{-1} \quad (2.15)$$

where $\Lambda_{disc/cyl}$ are the permeances of a the disc/cylinder located in-between the two considered arc-shaped fringing permeances.

In order to define the reliability of the methodology introduced in this section, the fringing permeances described in Fig. 2.6a and 2.6b are computed both using the introduced approach and the relations defined in [5] and [7]. The results are then compared with the values obtained through FE simulations in which the same structures described in Fig. 2.2 have been modelled in order to rebuilt the same case study used for the determination of the analytical formulations. Figures 2.8a and 2.8b show the relative errors of the different approaches computed with respect to FEA results. The external radius L_o defining the plots x axes is

respectively referred to Fig. 2.6a and 2.6b.

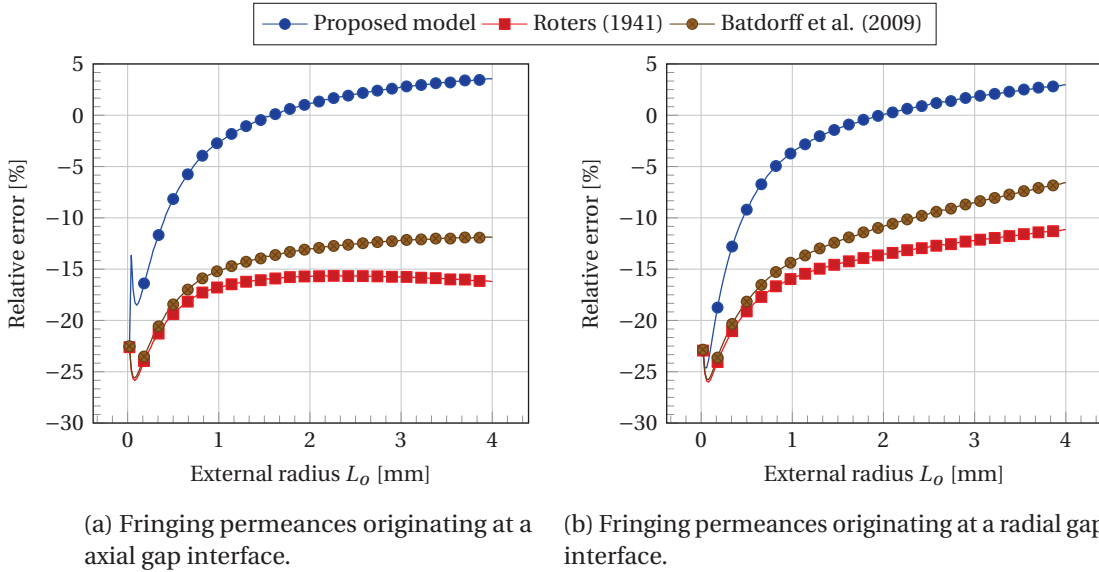


Figure 2.8 – Relative errors of the existing methods and the proposed model for the fringing permeance computation with respect to FEA results.

In particular, it can be seen that all the models are affected by a large error in the estimation of the fringing permeances for small values of L_o . This result can be explained considering that, in such situation, all the models reduce to a similar permeance expression, as already discussed for the definition of (2.9). Nevertheless, the proposed model demonstrates to be able to correct such initial inaccuracies and reduce the relative error more rapidly and with an overall higher degree of accuracy if compared to the evaluated existing methods.

2.3 HFMEC of MR valves

As previously introduced, the electromagnetic devices on which the proposed modelling will be applied consist in MR valves. In particular, the three configurations that have been presented in chapter 1 will be addressed, the main difference being related to the geometry of the valve active regions where magnetic field lines cross the fluid. Nevertheless, for the sake of brevity and clarity, only the annular configuration will be referred in the following section, the same approach being easily applicable to the other two remaining configurations. The complete schemes as well as the definitions introduced hereafter are anyway derived and reported for the radial and annular-radial configurations in the Appendix B.

A particular relevance has to be given to the fact that all the valves domains which are included neither in the ferromagnetic cores nor in the non-ferromagnetic coil and support regions are filled with MR fluid. Consequently, these regions exhibit a relative permeability μ_r ranging from 4 up to 7 depending on the particular fluid considered. Such a specific feature further justifies the need to model fringing and leakage fluxes external to the magnetic cores. In fact,

the higher values of μ_r in these regions enhance the leakage of magnetic flux, which tends to distribute more easily in the domains surrounding the magnetic cores. The main consequence is a reduction in the magnitude of the magnetic induction B_{MR} in the valves active regions, which represents the most relevant design parameter for the considered devices.

2.3.1 Permeances Calculation

In order to define a magnetic equivalent circuit, nodes have been placed on each valve configuration to break the real circuit in basic magnetic elements for which it is possible to easily determine the associated permeances. In particular, the number of distinct parts evaluated represents a compromise between the desired level of accuracy and the complexity of the overall model achieved, this last parameter being directly related with the computational time required to solve the equivalent circuit.

As previously introduced, HFMECs represent an extension of traditional MECs. Thus, the initial step to be performed is the determination of a standard lumped magnetic equivalent circuit for each analysed structure. All the coils depicted are assumed to have a square cross-section. Because all the addressed geometries are axisymmetric, cylinders and discs can be used to split the main magnetic circuit into basic magnetic elements in relation to the associated direction of the magnetic flux, which is respectively axial or radial. Nodes are placed at the interface of such domains following the mean flux path approximation [7], according to which

- the induction distribution is uniform all over each section orthogonal to the magnetic flux
- the magnetic field lines length is defined by an average path
- each flux direction variation is represented by a square angle.

Following this convention, the main nodes describing MECs can be obtained. The light grey sections displayed in Fig. 2.9a represent the bodies taken in consideration to define the permeances required to build the lumped magnetic equivalent circuit.

Such approximation can be easily extended to take into account leakage fluxes and fringes as described in section 2.2, obtaining this way improved HFMECs. In particular, it must be underlined that all the studied geometries are not only axisymmetric, but a symmetry plane orthogonal to the y coordinate and containing the origin also exists. This means that the permeances associated with an opposite y are equal.

2.3.2 MEC Permeances

Considering the nodes placement of Fig. 2.9a, all the permeances required to build the MECs associated to the evaluated geometries can be easily determined. The resulting networks,

which take into account only white filled elements labeled Λ_i , are displayed in Fig. 2.9b. In particular, due to the aforementioned considerations regarding the double symmetry of the considered structures, only half of the permeances have to be computed for each configuration.

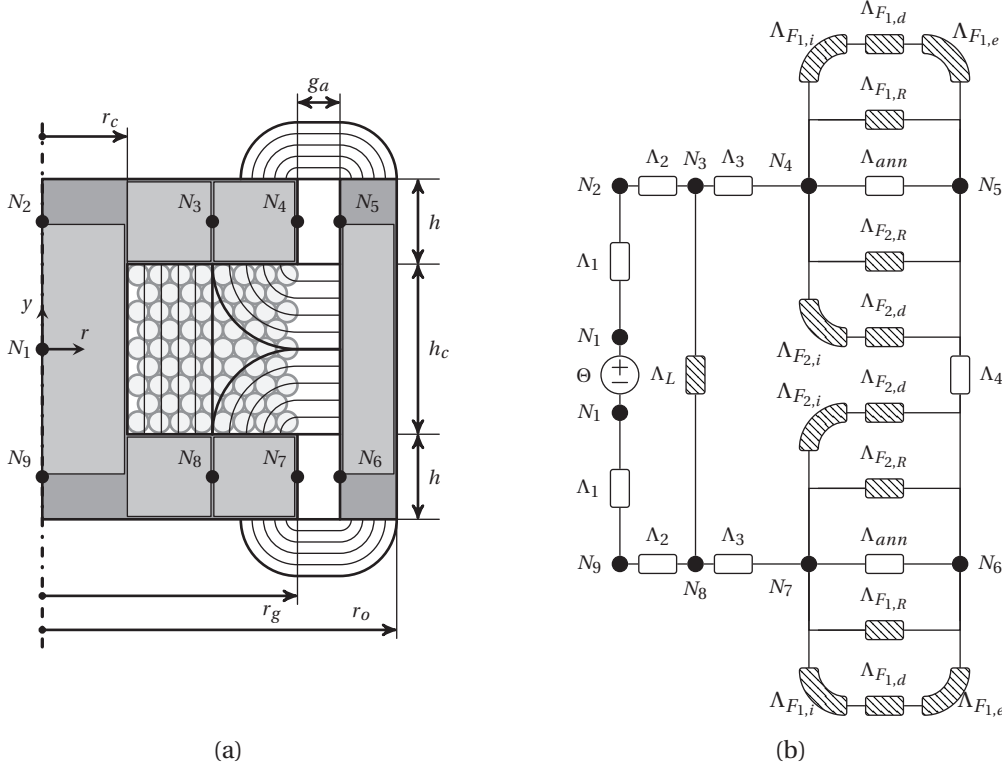


Figure 2.9 – **Annular MR valve configuration:** (a) - Nodes placement for the lumped magnetic model. (b) - Corresponding HFMEC.

Cylinder permeances (Fig. 2.10a) are crossed by a magnetic flux directed along the symmetry axis direction and can be simply computed applying (2.2) as

$$\Lambda_{cyl} = \mu_0 \mu_r \frac{\pi(r_o^2 - r_i^2)}{h} \quad (2.16)$$

where r_o and r_i represent respectively the outer and the inner radius of the considered tube of flux and h is its total height. Thus, the complete expression for the permeances of cylindrical magnetic domains depicted in Fig. 2.9a are

$$\Lambda_1 = \mu_0 \mu_{Fe} \frac{2\pi r_c^2}{h + h_c} \quad (2.17)$$

$$\Lambda_4 = \mu_0 \mu_{Fe} \frac{\pi[r_o^2 - (r_g + ga)^2]}{h + h_c}. \quad (2.18)$$

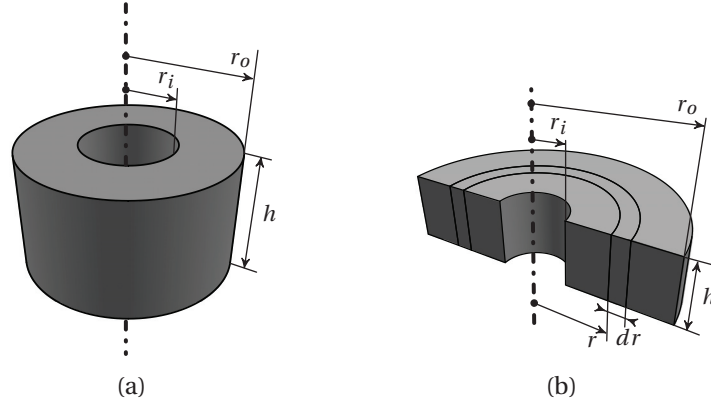


Figure 2.10 – Elementary domains for the computation of MEC permeances: (a) - Cylindrical geometry. (b) - Disc geometry.

Disc permeances (Fig. 2.10b), for which the direction of the magnetic flux is radial, have to be computed considering the reluctance expressed as

$$\mathcal{R}_{disc} = \int_{r_i}^{r_o} \frac{1}{2\pi\mu_0\mu_r r h} dr = \frac{1}{2\pi\mu_0\mu_r h} \ln\left(\frac{r_o}{r_i}\right) \quad (2.19)$$

which leads to the following permeance

$$\Lambda_{disc} = \mu_0\mu_r \frac{2\pi h}{\ln\left(\frac{r_o}{r_i}\right)}. \quad (2.20)$$

Consequently, to complete the list of permeances defining the MEC of the annular configuration, we have

$$\Lambda_2 = \mu_0\mu_{Fe} \frac{2\pi h}{\ln\left(1 + \frac{w_c}{2r_c}\right)} \quad (2.21)$$

$$\Lambda_3 = \mu_0\mu_{Fe} \frac{2\pi h}{\ln\left[r_g / \left(r_c + \frac{w_c}{2}\right)\right]} \quad (2.22)$$

$$\Lambda_{ann} = \mu_0\mu_{MR} \frac{2\pi h}{\ln\left(1 + \frac{g_a}{r_g}\right)} \quad (2.23)$$

where $w_c = r_g - r_c$ is the coil width.

2.3.3 HFMEC Permeances

To extend MECs to HFMECs, fringing and leakage permeances have to be computed.

2.3.3.1 Fringing permeances

Fringing phenomena, which are graphically represented in Fig. 2.9a are modelled through the approach defined in section 2.2. In particular, as appears straightforward considering the graphical representations given, the most external arc fringes are assumed to be tangent to the outer domain boundary from which themselves originate. Following this consideration, geometrical parameters to be inserted in (2.5) and (2.6) can be easily determined. In particular, if the first group of fringes Λ_{F_1} originating over and above the magnetic structure is addressed we have

$$\Lambda_{F_1} = \Lambda_{F_{1,R}} + \left(\frac{1}{\Lambda_{F_{1,i}}} + \frac{1}{\Lambda_{F_{1,d}}} + \frac{1}{\Lambda_{F_{1,e}}} \right)^{-1}. \quad (2.24)$$

Considering (2.9) and (2.10), it results that

$$L_{F_{1,i}}^* = \frac{r_g}{\cos(\theta_i^*)} \cdot 10^{-2} \quad L_{F_{1,e}}^* = \frac{r_g \cdot L_{F_{1,i}}^*}{(r_g + g_a)}.$$

Consequently, we have

$$\Lambda_{F_{1,R}} = 2\mu_0\mu_{MR} r_g \ln \left(1 + \frac{\pi L_{F_{1,i}}^*}{g_a} \right) \quad (2.25)$$

$$\Lambda_{F_{1,i}} = 4\mu_0\mu_{MR} \left\{ r_g \ln \left[\frac{r_o - (r_g + g_a)}{L_{F_{1,i}}^*} \right] - [r_o - (r_g + g_a) - L_{F_{1,i}}^*] \cos(\theta_i^*) \right\} \quad (2.26)$$

$$\Lambda_{F_{1,d}} = \frac{2\pi\mu_0\mu_{MR}}{\ln \left[\frac{(r_g + g_a)(r_o - r_g - g_a - L_{F_{1,i}}^*)}{r_g(r_o - r_g - g_a - L_{F_{1,e}}^*)} \right]} \quad (2.27)$$

$$\Lambda_{F_{1,e}} = 4\mu_0\mu_{MR} \left\{ (r_g + g_a) \ln \left[\frac{r_o - (r_g + g_a)}{L_{F_{1,e}}^*} \right] + [r_o - (r_g + g_a) - L_{F_{1,e}}^*] \cos(\theta_e^*) \right\}. \quad (2.28)$$

For what concerns the permeances for the second group of fringes, which are internal to the magnetic structure and cross both the valve coil and the MR fluid, we have

$$\Lambda_{F_2} = \Lambda_{F_{2,R}} + \left(\frac{1}{\Lambda_{F_{2,i}}} + \frac{1}{\Lambda_{F_{2,d}}} \right)^{-1} \quad (2.29)$$

$$\Lambda_{F_{2,R}} = 2\mu_0\mu_{MR} r_g \ln \left(1 + \frac{\pi L_{F_{1,i}}^*}{g_a} \right) \quad (2.30)$$

$$\Lambda_{F_{2,i}} = 4\mu_0 \left[r_g \ln \left(\frac{w_c}{2L_{F_{1,i}}^*} \right) - \left(\frac{w_c}{2} - L_{F_{1,i}}^* \right) \cos(\theta_i^*) \right] \quad (2.31)$$

$$\Lambda_{F_{2,d}} = \frac{2\pi\mu_0\mu_{MR}}{\ln \left[\frac{(r_g + g_a)(w_c/2 - L_{F_{1,i}}^*)}{r_g(w_c/2 - L_{F_{1,e}}^*)} \right]} \quad (2.32)$$

2.3.3.2 Leakage permeances

To comprehensively describe all the magnetic paths depicted in Fig. 2.9a, leakage permeances defined as Λ_L have to be computed. Although for the previously introduced computation of fringing permeances it has been assumed that all the coil windings were enclosed in the considered magnetic paths, for the leakage permeances only the current actually linked by the magnetic flux will be taken into account, as proposed in [6]. More in detail, it can be seen from Fig. 2.9a that, in order to avoid the overlap with the internal fringing permeance, the external boundary of the leakage permeance can be located at

$$r^* = \frac{r_g + r_c}{2}. \quad (2.33)$$

If a uniform distribution of conductors is assumed for the coil and if the magnetic potential drop in the ferromagnetic core is considered negligible, applying the Ampere's Law follows

$$\oint H dl = H_z(r) h_c = i_{enclosed} = Ni \frac{r^* - r}{r^* - r_c} \quad (2.34)$$

where H_z is the magnetic path parallel to the geometry symmetry axis, N is the coil number of turns and r is the radial coordinate. Considering that the energy stored in a magnetic inductor matches the actual energy contained in the magnetic field that the inductor creates itself, it is possible to write

$$E = \frac{1}{2} Li^2 = \frac{1}{2} \Lambda N^2 i^2 = \frac{1}{2} \int_V \vec{B} \cdot \vec{H} dV = \frac{1}{2} \int_V \mu_0 H^2 dV. \quad (2.35)$$

Combining the two last relations introduced, we obtain for the computation of the leakage permeance

$$\begin{aligned}\Lambda_L &= \frac{\mu_0}{N^2 i^2} \int_{r_c}^{r^*} \frac{N^2 i^2}{h_c^2 (r^* - r_c)^2} (r^* - r) 2\pi r h_c dr = \\ &= \frac{2\pi\mu_0}{h_c (r^* - r_c)^2} \int_{r_c}^{r^*} (r^* - r)^2 dr = \\ &= \frac{\pi\mu_0}{6 h_c} (r^* - r_c)(r^* + 3r_c). \quad (2.36)\end{aligned}$$

As previously stated, the leakage permeances crossing the coil in the radial and annular-radial valves can be derived in the same way. Consequently, they can be expressed by mean of (2.36) and the only parameter to be redefined is r^* .

All the complete formulations defining the permeances associated to the different MR valves configurations studied are presented in Appendix B.

2.3.3.3 Circuit solution

After having defined all the required permeances to build the desired magnetic equivalent model, the circuit can be solved considering as source of excitation the overall magnetic potential provided by the coil

$$\Theta = J\chi S_{coil} \quad (2.37)$$

where J is the supplying current density, χ represent the coil filling factor and S_{coil} is the coil cross- sectional area. The magnetic flux ϕ_i circulating in the different branch permeances can be determined either by creating a branch list or using successive topological transformations [9]. The average flux density associated to a particular branch permeance Λ_i can be easily determined considering the average branch permeance cross-section A_i

$$B_i = \frac{\phi_i}{A_i} \quad (2.38)$$

which allows to find the related relative permeability $\mu_{r,i}$. Considering that the ferromagnetic media crossed by the magnetic field have a nonlinear B-H characteristic, a simple iterative solver routine is implemented to determine the value of $\mu_{r,i}$ for each permeance (Fig. 2.11). Convergence is achieved when the maximum among the relative errors between the permeabilities found for one iteration and the previous ones is below an imposed value of relative tolerance.

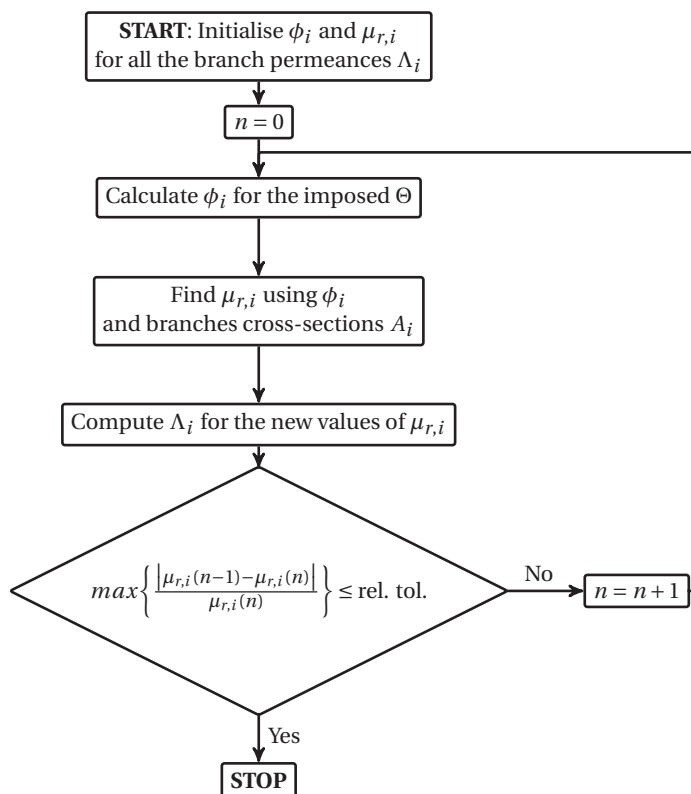


Figure 2.11 – Iterative solution flow chart used to solve the magnetic circuits for nonlinear permeability materials.

2.4 Results

In order to assess the improvement provided by the proposed modelling approach, the magnetic inductions in the valves gaps B_{MR} and the inductances associated to each configuration obtained solving the MECs and HFMECs are compared to FE analysis results. In particular the magnetic flux densities B_{MR} are used to estimate the quality of the magnetic modelling at the interface between the ferromagnetic cores and the valves channels (for which fringing leakage fluxes are most relevant) while the value of inductances discriminates the quality of the overall modelling (comprising how saturation is managed).

For each configuration, 20 different valves are dimensioned to achieve an imposed value of magnetic induction in the valves channels, which is fixed to be $B_{MR} = 0.5$ T. The dimensioning and the definition of the geometrical parameters is done accordingly to the design routine that will be discussed in the following chapter. The volume variation between the smallest and largest valve set specimens is of approximately 10 times.

Figures 2.12, 2.13, 2.14 and 2.15 (these two last sets of figures describing respectively the annular and radial channels of the annular-radial configuration) compare the different magnetic inductions B_{MR} in the valves gaps for the three different geometries studied obtained from MECs and HFMECs and FEA results.

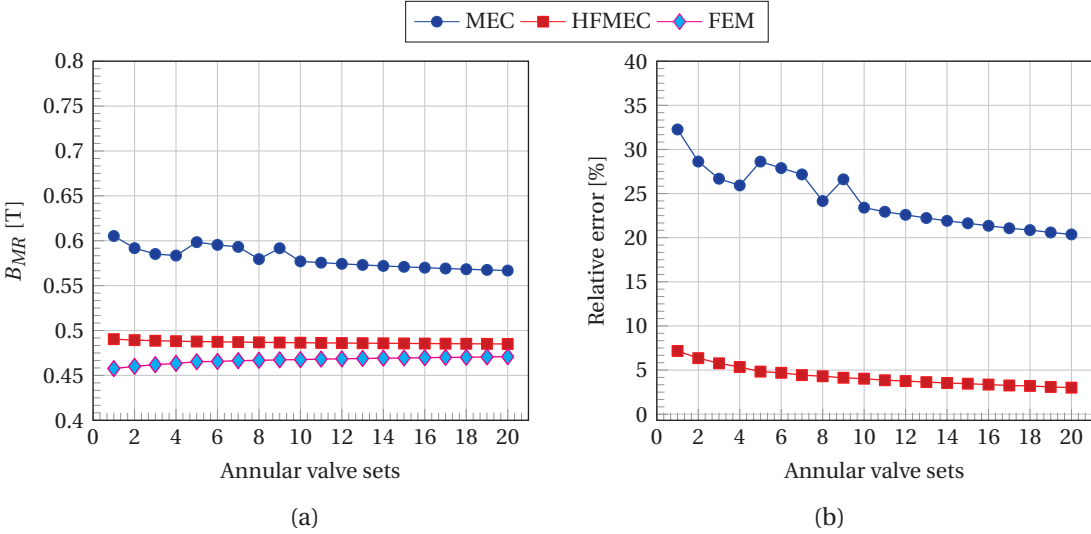


Figure 2.12 – **Annular MR valve configuration:** (a) - Magnetic inductions B_{MR} in the valve channel obtained with the different models. (b) - Relative error of the used methods with respect to FE results.

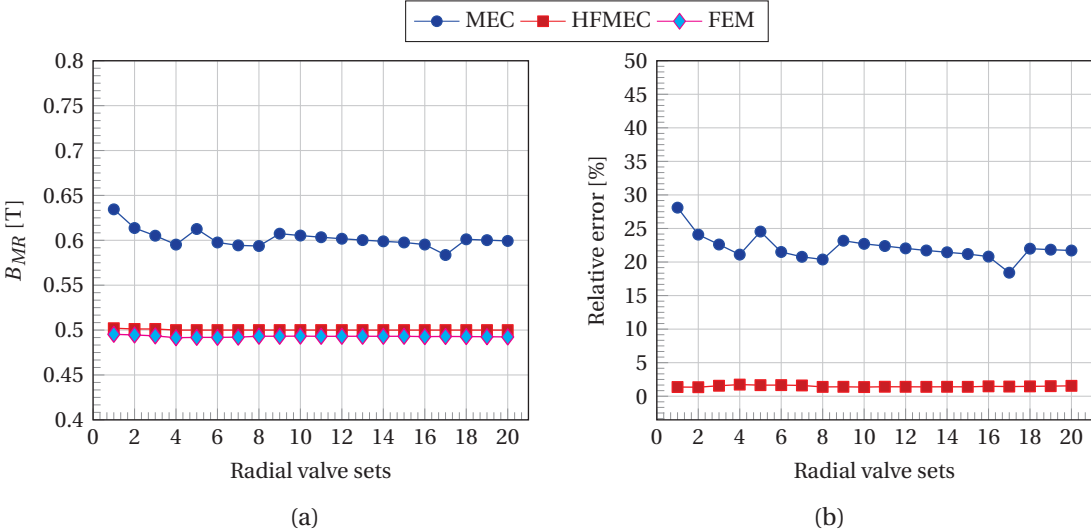


Figure 2.13 – **Radial MR valve configuration:** (a) - Magnetic inductions B_{MR} in the valve channel obtained with the different models. (b) - Relative error of the used methods with respect to FE results.

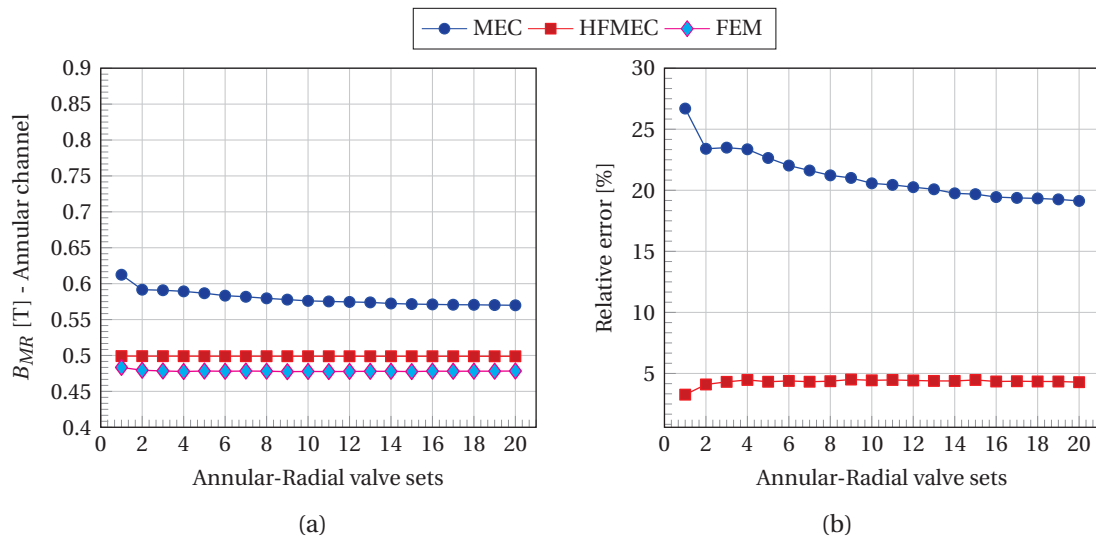


Figure 2.14 – **Annular-Radial MR valve configuration:** (a) - Magnetic inductions B_{MR} in the valve annular channel obtained with the different models. (b) - Relative error of the used methods with respect to FE results.

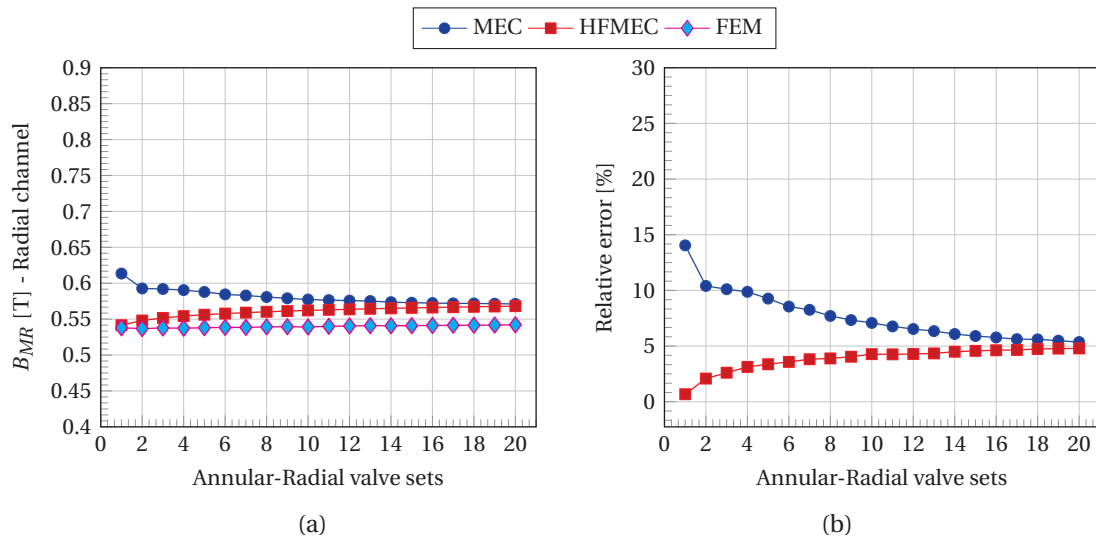


Figure 2.15 – **Annular-Radial MR valve configuration:** (a) - Magnetic inductions B_{MR} in the valve radial channel obtained with the different models. (b) - Relative error of the used methods with respect to FE results.

Chapter 2. High Fidelity Magnetic Equivalent Circuit for Axisymmetric Devices

As a further indicator of the accuracy of the proposed modelling, the average relative errors related to the magnetic flux density in the valves channels are reported in Table 2.2.

	Annular		Radial		Annular-Radial			
	$max\{\varepsilon_{B_{MR}}\}$ [%]	$\bar{\varepsilon}_{B_{MR}}$ [%]	$max\{\varepsilon_{B_{MR}}\}$ [%]	$\bar{\varepsilon}_{B_{MR}}$ [%]	$max\{\varepsilon_{B_{MR},a}\}$ [%]	$\bar{\varepsilon}_{B_{MR},a}$ [%]	$max\{\varepsilon_{B_{MR},r}\}$ [%]	$\bar{\varepsilon}_{B_{MR},r}$ [%]
MEC	32.2	24.3	28.1	22.1	26.7	21.1	14.1	7.6
HFMEC	7.2	4.3	1.7	1.5	4.5	4.3	4.8	3.9

Table 2.2 – Maximum ($max\{\varepsilon_{B_{MR}}\}$) and mean ($\bar{\varepsilon}_{B_{MR}}$) relative errors between FE analysis and analytical model results.

The following table lists the relative errors related to the determination of the inductances associated to the different magnetic structures analysed.

	Annular		Radial		Annular-Radial	
	$max\{\varepsilon_L\}$ [%]	$\bar{\varepsilon}_L$ [%]	$max\{\varepsilon_L\}$ [%]	$\bar{\varepsilon}_L$ [%]	$max\{\varepsilon_L\}$ [%]	$\bar{\varepsilon}_L$ [%]
MEC	32.2	36.8	92.2	87.6	175.7	170.2
HFMEC	6.5	5.9	2.8	0.6	4.5	5.5

Table 2.3 – Maximum ($max\{\varepsilon_L\}$) and mean ($\bar{\varepsilon}_L$) relative errors between FE analysis and analytical model results.

The quality of the high-fidelity modelling proposed with respect to traditional MECs is observable considering the relative errors in the determination of the magnetic flux density in the valves channels depicted in Fig. 2.12b, 2.13b and 2.14b.

If the results related to the annular configuration are more deeply analysed (Fig 2.12) it can be seen how the proposed approach provides a high level of accuracy in the modelling of magnetic phenomena, namely fringing fluxes, at the valve channels boundaries and the relevant improvement with respect to the MECs.

Focusing on the radial configuration results (Fig. 2.13) the improvement provided by the HFMECs are even more relevant. This outcome can be explained considering that, because of the particular radial valve geometry, a higher amount of fringes crosses the MR fluid if compared to the annular valve with a consequent higher relative influence of fringing fluxes on the overall magnetic flux (Fig. B.1a). This interpretation also explains the large average relative error in the computation of the inductance L (Table 2.3). MECs, which do not take into account fringing fluxes, provide a drastic overestimation of the total reluctance of the studied magnetic structure (fringing paths increase the overall permeance of the magnetic circuit) and a consequent underestimation of the inductance. Moreover, it has been found that the introduction of the leakage permeance Λ_L in the MECs produces a reduction in the

relative error estimation of L of less than 3%, which underlines the dominant effect of fringing fluxes through a magnetic domain with a high relative permeability.

The same considerations done for the radial valves can be extended to annular-radial valves. The only difference is that, because of the particular geometry chosen to implement the annular radial configuration, fringes related to the radial channel originate nearby the axis of symmetry and the overall magnetic flux is directly shared between the ferromagnetic core and the central MR fluid channel (Fig. B.2a). This causes the aforementioned underestimation of the total structure permeance to be even more relevant.

The error in the estimation of the magnetic flux inductions in both the valve channels is similar and reduced to acceptable values with HFMECs, while the error distribution between annular and radial channel is not equal. This can be explained considering that, in reason of a design assumption that will be justified in the following chapter, the reluctances of all the valve channels are imposed to be the same. This implies that, because MECs consider only one magnetic path, the magnetic flux densities are also the same. Once again, the contribution of the fringing permeance associated to the radial channel, which is more relevant than the one related to the annular channel, is crucial and it results in the consistent overestimation of the magnetic flux density in the radial active region.

After having compared the estimation of the relevant magnetic quantities, it is interesting to compare the computational times required to solve the HFMECs and FE models of each configuration. For what concerns the FE analysis, mesh generation and model solution have been found to be the tasks more expensive in terms of execution time. In particular, an extremely fine mesh will affect, namely increase, the running time of both the mesh generator and the solver with a consequent bias of the intended comparison. In order to solve this issue, the automatic mesh generation routine proposed by the employed FE software is chosen. Moreover, the resolution is set to the maximum value for which a finer mesh would not improve the solution accuracy.

The mean gain in the computational time, which is similar for all evaluated configurations, is about 200 times, this value underlining the cost efficiency of the proposed modelling approach.

2.5 Summary and conclusion

In this chapter, a novel semi-empirical FE-based model of fringing fluxes occurring in axisymmetric electromagnetic devices has been firstly discussed. In particular, starting from the approximation describing fringes originating at the interface of domains with different magnetic permeability with quarter-circles and straight lines, an analytical expression for the computation of the associated permeances in the case of axisymmetric geometries is presented. Because of the non-closed form solution of the integral associated with the proposed formulations, FE analyses combined with a regression algorithm are used to define semi-empirical approximations able to solve the non-convergence problem. The reliability of the proposed method has been demonstrated and the accuracy improvement for the estimation

Chapter 2. High Fidelity Magnetic Equivalent Circuit for Axisymmetric Devices

of arc-shaped fringing permeances with respect to existent approaches is consistent.

Successively, the MECs associated with three different magneto-rheological valves configurations are extended to HFMECs following the presented derivation to take into account fringing and leakage fluxes. If compared with FEAs, the error in the determination of the magnetic induction magnitude in the valves channels (B_{MR}) has been reduced to a maximum of 4.3% in the worst case analysed (corresponding to the annular configuration). The proposed model has proven to be a reliable, accurate and computationally inexpensive tool for the modelling of axisymmetric electromagnetic devices.

Publications related to this chapter:

- D. Grivon, Y. Civet, Z. Pataky and Y. Perriard, *High-Fidelity Magnetic Equivalent Circuit Modelling of Axisymmetric Magneto-Rheological Devices*, Magnetics, IEEE Transactions on, Accepted for Publication.
- D. Grivon, Y. Civet, Z. Pataky and Y. Perriard, *Design and comparison of different Magneto-Rheological valves configurations*, Advanced Intelligent Mechatronics (AIM), 2015 IEEE International Conference on, pp. 818-823, Busan, 2015.

Bibliography

- [1] V. Ostović, *A Simplified Approach to Magnetic Equivalent Circuit Modelling of Induction Machines*, Industry Applications, IEEE Transactions on, Vol. 24, No. 2, April 1988.
- [2] M. Amrhein and P. T. Krein, *3-D Magnetic Equivalent Circuit Framework for Modeling Electromechanical Devices*, Energy Conversion, IEEE Transactions on, Vol. 24, No. 2, June 2009.
- [3] C. Chillet and J.-Y. Voyant, *Design-Oriented Analytical Study of a Linear Electromagnetic Actuator by Means of a Reluctance Network*, Magnetics, IEEE Transactions on, Vol. 37, No. 4, July 2001.
- [4] C. Pompermaier, K. F. J. Haddad, A. Zambonetti, M. V. Ferreira da Luz and I. Boldea, *Small Linear PM Oscillatory Motor: Magnetic Circuit Modeling Corrected by Axisymmetric 2-D FEM and Experimental Characterization*, Industrial Electronics, IEEE Transactions on, Vol. 59, No. 3, March 2012.
- [5] H. C. Roters, *Electromagnetic Devices*. New York: Wiley, 1941.
- [6] J. Cale, S. D. Sudhoff and L.-Q. Tan, *Accurately Modeling EI Core Inductors Using a High-Fidelity Magnetic Equivalent Circuit Approach*, Magnetics, IEEE Transactions on, Vol. 42, No. 1, January 2006.
- [7] M. A. Batdorff and J. H. Lumkes, *High-Fidelity Magnetic Equivalent Circuit Model for an Axisymmetric Electromagnetic Actuator*, Magnetics, IEEE Transactions on, Vol. 45, No. 8, 2009.
- [8] M. Jufer, *Traité d'Electricité, Volume IX: Electromécanique*, Presses Polytechniques Universitaires et Romandes, 1995.
- [9] J. R. Brauer, *Magnetic Actuators and Sensors*, IEEE and John Wiley & Sons, Inc., Hoboken, 2006.

3 Design and Comparison of Different MR Valves Configurations

This chapter presents a design methodology for the dimensioning of MR valves. In this sense, the main contribution of the contents developed henceforth concerns the analytical relations defined to comprehensively describe the valves configurations under study. The latter have been used to build a reliable, easy to implement and cost efficient routine to quickly design different magneto-rheological valves. These features are particularly interesting in the case of a feasibility study, to compare the advantages/drawbacks that each configuration offers with respect to the others, to identify the best geometry for a particular application or to provide a starting specimen on which apply an optimisation routine or from which build a more precise Finite Element model.

In order to implement the proposed design methodology, the most relevant analytical relations required to comprehensively describe the three valves configurations under study, namely the annular, radial and annular-radial MR valves, are firstly given. Successively, the derived expressions are used as a basis to design MR valves able to satisfy the imposed design requirements for what concerns both the fluidic and the electromagnetic part.

An analytical model is developed for each of the geometries of interest and four evaluation criteria as the volume to maximum sustainable pressure ratio, the dynamic range, the efficiency and the valve reactivity are used to compare the performances of the different valves designs. In particular, the derived analytical relations allow to dimension each valve typology imposing the maximum sustainable pressure drop, the free flow rate (i.e. the flow rate when the valve is off), the dynamic range and the maximum current density supplying the exciting coil. Finite Element analysis are performed to validate the results obtained from the analytical models derived and a comprehensive discussion on the comparison of the different figures of merit is done.

3.1 Introduction

Chapter 1 has given the main concepts to understand the rheological principles on the basis of MR systems and it has provided an initial presentation of the three different MR valves configurations studied. Nevertheless, in this first introduction only their main features characterising the hydraulic part only, i.e. the achievable pressure drop ΔP and its relation with the intensity of the magnetic field H and the flow rate Q through the valves channels, has been discussed.

On the contrary, chapter 2 has provided a reliable analytical model to accurately solve the magnetic part of each of the studied geometries in order to precisely obtain the magnetic induction magnitude B_{MR} imposed in the valves active regions.

This chapter synthesises the concepts presented so far to provide a comprehensive design procedure to address simultaneously the two main physics included in a MR systems and build a structure able to simultaneously satisfy some imposed constraints for both the electro-magnetic and hydraulic parts.

Regarding this last aspect, [1] and [2] have reported a methodology to dimension, compare and optimise different MR brakes configurations on the basis of analytical models successively validated using Finite Element analysis. As already introduced in chapter 2, one of the most interesting features of using an analytical model is the possibility to underline how the variation of the involved geometrical parameters affects the device performances. This last point assumes an even higher relevance considering the complexity of the design scenario due to the correlation of the several parameters involved which have different and sometimes opposite effects. Although these works appear interesting for what concerns the methodological approaches proposed, it is found that the analytical models on their bases are a bit rough, at least for what concerns the modelling of the magnetic part. In fact, the common practice is to consider only the active regions, where the exciting magnetic path crosses the MR fluid, for the description of the magnetic circuit associated to the structures under analysis. In this respect, this way to proceed offers as main advantage a relatively low complexity, but it occurs, as main drawback well-illustrated in the previous chapter, in high errors in the estimation of all the magnetic related quantities (i.e. the average flux densities, inductances, saturation zones in the magnetic circuits,...) with the risk of finally relying on inconsistent results.

On the contrary, for what concerns MR valves, a common design practice is to dimension the fluidic part considering the well-known analytical relations introduced in chapter 1, while the magnetic part is usually designed using FE analysis [3, 4, 5]. This modus operandi is remarkably time consuming especially for the sake of a first evaluation to define the most suitable design for a particular application.

In this respect, the combination of the HFMEC presented in chapter 2 with extended formulations presented hereafter is intended to fill this lack of modelling and complete the analytical design methodology for the dimensioning and for the evaluation of MR valves and, more in general, MR devices based on similar geometries.

3.2 Evaluation criteria for MR valves

In order to evaluate and compare the performances of the valves configurations under analysis and following a similar approach to the one proposed in [2], four different evaluation criteria such as the dynamic range, the sustainable pressure to volume ratio, the efficiency and the reactivity have been defined. In particular, their expressions will be given as a function of the magnetic flux density in the valves active regions B_{MR} which represents the most relevant parameter in the proposed design methodology.

Pressure to Volume Ratio

In order to take into consideration the physical dimensions of the valves, the pressure to volume ratio κ (i.e. the pressure density) is obtained dividing the maximum magnetic field induced pressure drop $\Delta P_{\tau_{max}}$ by the total valve volume V_{tot} .

Dynamic Range

The dynamic range D is defined as the ratio between the maximum magnetic field induced pressure drop $\Delta P_{\tau_{max}}$ and the off-state viscosity dependent pressure drop ΔP_{η} . This figure of merit defines the valve range of operation, having as extrema respectively a situation of *free flow* and the condition of *no flow*.

Efficiency

The ratio between the maximum field induced sustainable pressure drop $\Delta P_{\tau_{max}}$ and the electrical power consumption W_{Joule} (Joule losses in the coil) gives the valve efficiency \mathcal{E} . This criterion defines the amount of energy required to impose and maintain a value of magnetic flux density in the valves channels high enough to sustain an imposed pressure drop.

Reactivity

The valve reactivity \mathcal{R} is constrained by the electromagnetic circuit time constant and the fluid time response. In this regard, the activation time required by a MR fluid to switch from the liquid to the semi-solid state is less than 1 ms [6]. Thus, it can be considered negligible with respect to the time required to reach the desired exciting magnetic field in the valve channel. In particular, the latter is related to the coil time constant τ_{coil} which depends on the coil features (wire cross-section and coil dimensions determining its resistance) and on the magnetic reluctance associated with the coil itself (defining its inductance).

3.3 MR valves analysis

In this section, the three MR valves configurations under study will be analysed. Using as the first case of study the annular valve geometry, the relevant analytical formulations are derived. Successively, the same approach is transferred to the radial and annular-radial geometries. The performed investigation assumes as starting points

- magnetic flux conservation, which assumes that the same magnetic flux circulates in all the elements composing the magnetic circuit of interest (no leakage or fringing fluxes are considered in these initial formulations)
- the definition of the desired magnetic induction B_{MR} over the MR fluid surface and the maximum allowed magnetic induction in the iron cores B_{iron} .

The values of magnetic flux density are chosen to never exceed the induction saturation threshold of the materials and always remain within the first part of the B-H characteristics, which can be approximated with the linear relation $H = \mu_0\mu_r B$, and for which the values of magnetic induction in the structure achievable with a certain imposed magnetic potential are maximised. More in details, the first approximation may result a bit rough, but it allows to initially focus the attention only on the valves channels. Furthermore, as clearly underlined, it is a merely starting point which can be successively improved, if judged necessary and if improved modelling tools are available, as it will be demonstrated later on.

3.3.1 Annular MR valve

Figure 3.1 depicts the geometrical parameters required to completely define an annular MR valve configuration.

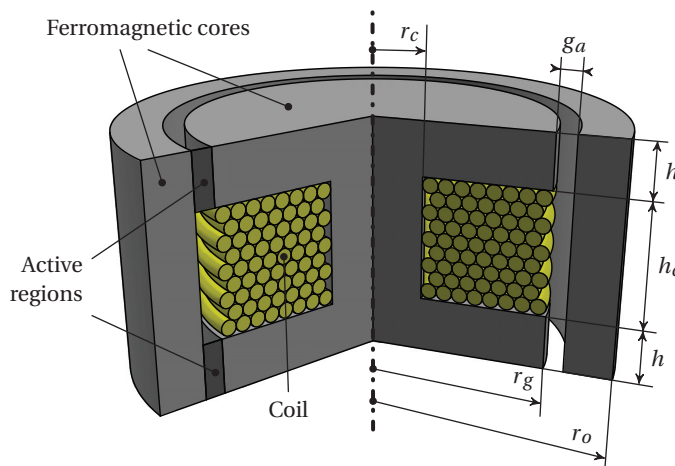


Figure 3.1 – Schematic representation and geometrical parameters for the annular MR valve configuration.

In this case, by mean of relation (1.11) we can define the maximum achievable pressure drop ΔP as

$$\Delta P = \underbrace{\frac{2c\tau_y(H)(2h)}{g_a}}_{\Delta P_\tau} + \underbrace{\frac{12\eta Qh}{g_a^3 \pi r_g}}_{\Delta P_\eta} \quad (3.1)$$

where ΔP_τ is the field induced dependent pressure drop, ΔP_η is the viscosity dependent pressure drop with no exciting magnetic field, η is the off-state fluid viscosity, Q is the valve flow rate, c is a fluid coefficient ranging from a minimum value of 2 ($\Delta P_\tau/\Delta P_\eta \approx 1$) up to a maximum value of 3 ($\Delta P_\tau/\Delta P_\eta \geq 100$), while the remaining geometrical parameters are referred to Fig. 3.1.

Pressure to volume ratio

In the definition of $\Delta P_{\tau_{max}}$, the magnetic field dependent yield stress $\tau_y(H)$ gives one of the most relevant contributions. As already introduced in section 1.2.1, its commonly non-linear characteristic can be approximated, for moderate values of induction over the fluid surface lower than saturation, with the linear relation

$$\tau_y(H) = \alpha H_{MR} \quad (3.2)$$

It is important to remind that H_{MR} represents the actual intensity of the magnetic field across the active surface of the valve channels and it is assumed to be perpendicular to the fluid flow. In this respect, the Ampère's Law relates all the main magnetic quantities

$$\Theta_T = \int J dA = Ni = \oint H dl = Hl = \frac{B}{\mu_0\mu_r} l = \frac{\phi}{S} \frac{l}{\mu_0\mu_r} = \phi_T \cdot \mathcal{R}_T \quad (3.3)$$

stating that the overall source of the magnetomotive force Θ_T , represented by a coil with N turns supplied with a current i , is responsible of the rise of a magnetic flux ϕ_T circulating in the associated magnetic circuit of total reluctance \mathcal{R}_T .

By mean of (3.3), the magnetic flux crossing the MR fluid can be easily related to the magnetic potential drop across the valve channel Θ_{MR} , this last quantity being geometrically related to H_{MR} . We have that

$$\Theta_{MR}(t) = \phi_{MR}(t) \cdot \mathcal{R}_{MR} \quad (3.4)$$

where \mathcal{R}_{MR} is the reluctance of the only active regions while ϕ_{MR} is the magnetic flux actually crossing the MR fluids. In particular, Θ_{MR} can be seen as a fraction of the overall magnetic potential created by the exciting coil. In this sense, it is possible to define

$$\Theta_{MR}(t) = \sigma \Theta_T(t), \quad \text{with } 0 \leq \sigma \leq 1. \quad (3.5)$$

Chapter 3. Design and Comparison of Different MR Valves Configurations

The value of σ is related to the equivalent model employed to describe the real magnetic circuit of the structure under study. For example, if only the MR valve channels are considered for the estimation of the overall system reluctance and the magnetic potential drop in the ferromagnetic cores is neglected, the value of σ equals 1. On the contrary, to improve the description of the actual magnetic behaviour of the devices under analysis, the parameter σ can be estimated using the High-Fidelity Magnetic Equivalent Circuit discussed in chapter 2. The reluctance of the valve active regions can be found integrating radially the surface from r_g up to $r_g + g_a$ obtaining

$$\mathcal{R}_{MR} = \int_{r_g}^{r_g + g_a} \frac{2}{\mu_0 \mu_{MR} 2\pi r h} dr = \frac{\ln\left(1 + \frac{g_a}{r_g}\right)}{\mu_0 \mu_{MR} \pi h} \quad (3.6)$$

which, assuming $r_g \gg g_a$, can be well approximated as

$$\mathcal{R}_{MR} = \frac{g_a}{\mu_0 \mu_{MR} \pi r_g h}. \quad (3.7)$$

The surface of the MR fluid crossed by the magnetic flux ϕ_{MR} is considered to be

$$S_{MR} = 2\pi r_g h. \quad (3.8)$$

By mean of (3.4), (3.7) and (3.8) we obtain a simplified expression of the magnetic potential drop across the annular MR channel, which is

$$\Theta_{MR} = \frac{2g_a}{\mu_0 \mu_{MR}} B_{MR} = 2g_a H_{MR}. \quad (3.9)$$

Combining this last relation with (3.2) and with the first term of (3.1) we obtain the following expression for the maximum sustainable pressure as a function B_{MR}

$$\Delta P_{\tau_{max}} = \frac{4ch\alpha}{\mu_0 \mu_{MR} g_a} B_{MR}. \quad (3.10)$$

Once defined the desired maxima inductions for the iron cores and the MR fluid, it is possible to define the maximum induction ratio

$$\zeta = B_{MR} / B_{iron}. \quad (3.11)$$

Then, considering the assumption of magnetic flux conservation, the iron and the MR active surface can be related as follows

$$S_{iron} = \zeta \cdot S_{MR} \quad (3.12)$$

which gives

$$S_{iron} = 2\pi \left(r_g + \frac{g_a}{2} \right) h \zeta \approx 2\pi r_g h \zeta. \quad (3.13)$$

If we want to define the thickness of the outer magnetic core, we have that

$$\pi[r_o^2 - (r_g + g_a)^2] B_{iron} = 2\pi r_g h B_{MR} \quad (3.14)$$

which, through (3.11), gives us the external radius

$$r_o = \sqrt{(r_g + g_a)^2 + 2 r_g h \zeta}. \quad (3.15)$$

In order to minimize the coil mean radius \bar{r}_c , the coil internal radius r_c has to be minimized too. This condition is achieved when r_c guarantees the minimal iron surface in the centre of the valve to avoid saturation

$$r_c = \sqrt{2 r_g h \zeta}. \quad (3.16)$$

The last unconsidered variable to completely define the valve geometry under discussion is the coil aspect ratio, i.e. the ratio between its width w_c and its height h_c . No explicit relation can be established to determine this value which represents a design choice mainly related to the dimensional and feasibility constraints of the final application. In particular, it will affect the overall power consumption and time response as well as the valve dynamic range and the total volume. To discuss this parameter it is useful to consider the required coil cross-section S_{coil} to obtain an overall magnetic potential

$$\Theta_T = J \chi S_{coil} \quad (3.17)$$

where χ is the coil filling factor. Combining the latter with the equations (3.5) and (3.9) we obtain

$$S_{coil} = \frac{1}{\sigma} \frac{2 g_a}{\mu_0 \mu_{MR} J \chi} B_{MR}. \quad (3.18)$$

Once S_{coil} is known, the ratio between the coil height and the coil width can be established being, as aforementioned, a design choice. For all the main cases discussed in this work, it is assumed that the coil height equals the coil width, this choice representing a good compromise between the reduction of the coil volume (i.e. of the coil mean radius \bar{r}_c) and its influence on the valve performances. The total volume of the valve can be now determined as

$$V_{tot} = \pi[(r_g + g_a)^2 + 2 r_g h \zeta] (2h + h_c) \quad (3.19)$$

required to finally define the valve pressure to volume ratio κ .

Dynamic range

The ratio between (3.10) and the second term of (3.1), gives us the valve dynamic range

$$D = \frac{\Delta P_{\tau_{max}}}{\Delta P_{\eta}} = \frac{c g_a^2 \pi r_g \alpha}{\mu_0 \mu_{MR} 3 \eta Q} B_{MR}. \quad (3.20)$$

It must be underlined that this a simplified formulation which describes what happens only in the active regions. In order to determine the correct values of the dynamic range, the pressure drop related to the inactive part of the channel in correspondence to the coil has to be added.

Efficiency

In order to determine the valve efficiency, the power consumption has to be determined. The latter can be obtained considering the Joule losses in the coil

$$W_{Joule} = R_w \cdot i^2 \quad (3.21)$$

with the coil resistance R_w depending on the coil parameters

$$R_w = \rho \frac{l_w}{S_w} = \rho \frac{2\pi \bar{r}_c N}{S_w} \quad (3.22)$$

where N is the coil number of turns, ρ is the copper resistivity, \bar{r}_c is the mean radius of the coil and S_w is the wire cross-section. Substituting (3.22) in (3.21) and considering that it is common practice to express the coil current supply as current density $J = i/S_w$ we obtain

$$W_{Joule} = 2\pi \bar{r}_c \rho J \Theta_T \quad (3.23)$$

which defines the required power supply as a function of the total magnetomotive force.

By mean of relations (3.5) and (3.6), we can now define the power consumption as a function of B_{MR}

$$W_{Joule} = 2\pi \bar{r}_c \rho J \frac{\Theta_{MR}}{\sigma} = \frac{2\pi \bar{r}_c \rho J}{\sigma} \mathcal{R}_{MR} S_{MR} B_{MR} = \frac{1}{\sigma} \frac{4\pi \bar{r}_c g \rho J}{\mu_0 \mu_{MR}} B_{MR}. \quad (3.24)$$

Consequently, the efficiency of the system becomes

$$\mathcal{E} = \frac{\Delta P_{\tau_{max}}}{W_{Joule}} = \frac{c h \alpha \sigma}{2\pi \bar{r}_c g_a^2 \rho J}. \quad (3.25)$$

Reactivity

Regarding the valve reactivity, it mainly depends on the coil time constant related to the associated RL circuit [7] which can be expressed again as a function of the induction through

the MR fluid

$$\tau_{coil} = \frac{L}{R_w} = \frac{N^2}{\mathcal{R}_T} \frac{1}{R_w} = \frac{1}{\sigma} \frac{g_a}{\mu_0 \mu_{MR} \pi \bar{r}_c \rho J} \frac{B_{MR}}{\mathcal{R}_T} \quad (3.26)$$

which allows to determine

$$\mathcal{R} = \frac{\Delta P_{\tau_{max}}}{\tau_{coil}} = \frac{c \alpha 2 \pi \bar{r}_c h}{g_a^2} \rho J \sigma \mathcal{R}_T. \quad (3.27)$$

3.3.2 Radial MR valve

The following analysis is based on the same main steps presented in the previous section for the annular valve geometry.

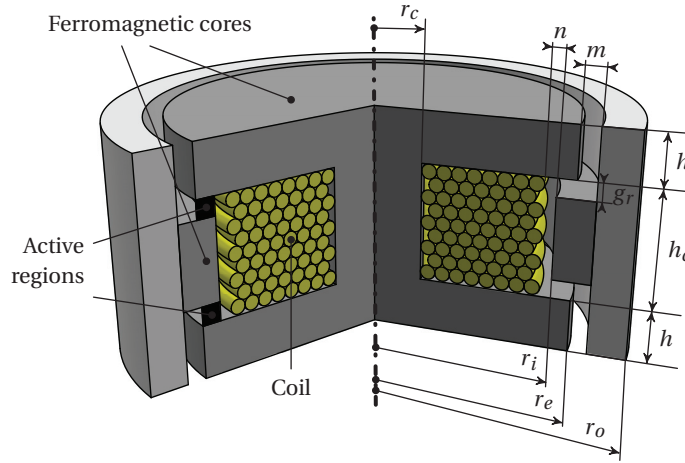


Figure 3.2 – Schematic representation and main geometrical parameters used to describe the radial MR valve configuration.

In relation to the geometrical parameters displayed in Fig. 3.2, the total pressure drop for this valve configuration is

$$\Delta P = \underbrace{\frac{2 c \tau_y(H) [2 (r_e - r_i)]}{g_r}}_{\Delta P_\tau} + \underbrace{\frac{12 \eta Q}{g_r^3 \pi} \cdot \ln \left(\frac{r_e}{r_i} \right)}_{\Delta P_\eta} \quad (3.28)$$

It must be underlined that this formulation takes into account only the pressure drops related to the radial active regions, while the annular channels having a width m and n at their entrances are not described. This implies that, in order to maintain the validity of the relations that will be defined further on, the latter have to be dimensioned in order to introduce a negligible viscosity dependent pressure drop with respect to the one considered for the active regions (i.e. the width n and m have to be large enough).

Pressure to volume ratio

If the magnetic path in the ferromagnetic cores is neglected, the remaining reluctance associated only with the MR channels is

$$\mathcal{R}_{MR} = \sum_{k=1}^n \frac{l_k}{\mu_0 \mu_{r,k} S_k} = \frac{2 g_r}{\mu_0 \mu_{MR} \pi (r_e^2 - r_i^2)}. \quad (3.29)$$

Consequently, following the same approach used for the annular configuration, it is possible to express the maximum field induced pressure drop as a function of the induction over the MR fluid surface as

$$\Delta P_{\tau_{max}} = \frac{4 c (r_e - r_i) \alpha}{\mu_0 \mu_{MR} g_r} B_{MR}. \quad (3.30)$$

In order to satisfy the conservation of magnetic flux, we have that the iron and MR surfaces must satisfy relation (3.12), which gives

$$h = \frac{\zeta}{2 r_i} (r_e^2 - r_i^2) \quad (3.31)$$

allowing to compute the total volume (the thickness of the external valve supports is not taken into account)

$$V_{tot} = \pi (r_e + l + m)^2 \left[\frac{\zeta}{r_i} (r_e^2 - r_i^2) + h_c \right]. \quad (3.32)$$

This last relation can be combined with (3.30) to define the valve pressure density κ .

Dynamic range

In order to define the real dynamic range, some considerations related to the particular fluid path have to be done. In particular, four variations of flow direction occur together with two sudden contractions and two sudden expansions of the valve ducts. The latter determine additional pressure drops that have to be taken into account for the determination of the overall viscosity dependent pressure drop P_η for a given flow rate Q . In this respect, it is common to introduce a loss coefficient ζ to take in consideration sudden contractions and sudden expansions [8]. In particular, experimental characteristics exist to define this parameter, which can also be determined empirically a posteriori for a particular structure. In our case, the value of ζ has been obtained as a correction factor using as reference FE analyses. Consequently, the overall dynamic range can be defined as

$$D = \frac{\Delta P_{\tau_{max}}}{(1 + \zeta) \Delta P_\eta} = \frac{1}{1 + \zeta} \cdot \frac{c (r_e - r_i) \pi g_r^2 \alpha}{\mu_0 \mu_{MR} 3 \eta Q \ln(r_e / r_i)} B_{MR}. \quad (3.33)$$

Efficiency

The valve power consumption can be determined with the same procedure used before obtaining the same expression. Hence, the valve efficiency is

$$\mathcal{E} = \frac{\Delta P_{\tau_{max}}}{W_{Joule}} = \frac{c(r_e - r_i)\alpha\sigma}{2\pi\bar{r}_c g_r^2 \rho J}. \quad (3.34)$$

Valve reactivity

Finally, the time constant of the coil is expressed by equation (3.26) and it can be used to determine the valve reactivity

$$\mathcal{R} = \frac{\Delta P_{\tau_{max}}}{\tau_{coil}} = \frac{c\alpha 2\pi\bar{r}_c (r_e - r_i)}{g_r^2} \rho J \sigma \mathcal{R}_T. \quad (3.35)$$

3.3.3 Annular-Radial MR valve

Figure 3.3 depicts a possible configuration for a MR valve with both annular and radial channels. In particular, in the following analysis it is assumed that the external radius of the radial gap equals the radius of the annular channel and the inner radius of the coil.

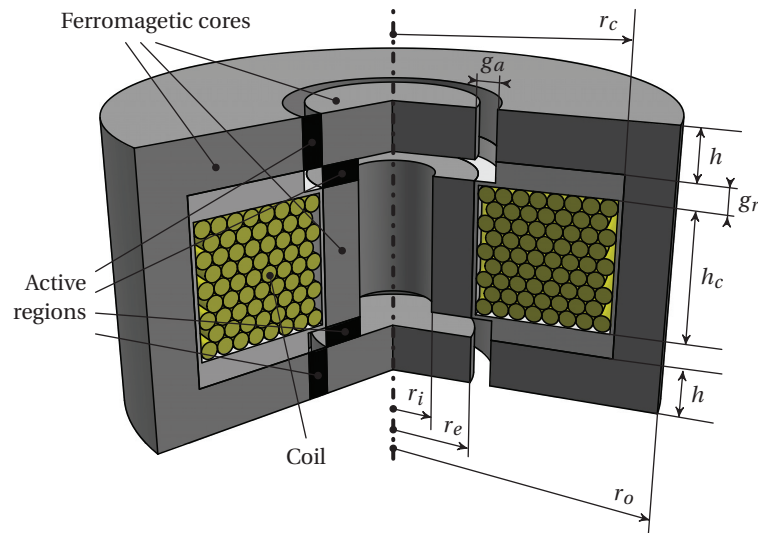


Figure 3.3 – Schematic representation and main geometrical parameters for the annular-radial MR valve configuration.

Pressure to volume ratio

In order to obtain the maximum performances from the MR phenomenon in both the valve channels, the magnitude of the magnetic induction crossing them is fixed to a value just below the saturation limit which must be equal in both the active regions

$$B_{MR,ann} = B_{MR,rad}. \quad (3.36)$$

Assuming the conservation of magnetic flux, equation (3.12) must be satisfied which leads

$$\pi(r_e^2 - r_i^2) = 2\pi r_i h \quad (3.37)$$

and consequently

$$h = \frac{(r_e^2 - r_i^2)}{2r_i}. \quad (3.38)$$

In accordance to the elementary relation (3.3) and considering that the source of magnetic potential is the same coil, it results that in order to satisfy relation (3.36) both the MR valve channel gaps must have the same reluctance

$$\frac{2g_r}{\mu_0\mu_{MR}\pi(r_e^2 - r_i^2)} = \frac{g_a}{\mu_0\mu_{MR}\pi r_i h} \Rightarrow h = \frac{(r_e^2 - r_i^2)}{2r_i} \frac{g_a}{g_r}. \quad (3.39)$$

This last relation and equation (3.38) can be both satisfied only if $g_a = g_r$. Thus, in the following developments both the channel gaps will be referred as g .

The maximum sustainable pressure drop is

$$\Delta P_{\tau_{max}} = \frac{4ch\alpha}{\mu_0\mu_{MR}g} [1 + 2r_i/(r_e + r_i)] B_{MR} \quad (3.40)$$

which underlines that, as somehow expected, the contribution of the two different channels to the overall sustainable pressure drop is almost the same. In fact we have that

$$\frac{2r_i}{r_e + r_i} = \frac{2r_i}{2r_i + \delta} \approx 1, \quad \text{for } \delta \ll r_i. \quad (3.41)$$

Similarly to what has been done previously, if the relations on the surfaces crossed by the magnetic path required to satisfy flux conservation and avoid saturation are imposed, we have that, considering the geometry depicted in Fig. 3.3, the total external radius r_o can be obtained as

$$r_o = \sqrt{(r_e + w_c)^2 + 2r_g h \zeta} \quad (3.42)$$

and for what concerns the total volume

$$V_{tot} = \pi [2r_e h \zeta + (r_e + w_c)^2] (2h + 2g + h_c) \quad (3.43)$$

where h_c and w_c define respectively the height and the width of the coil, which are assumed to be equal.

Dynamic range

Similarly to what discussed for the radial configuration, a loss factor ζ has to be introduced to take into account the losses related to the direction changes and the sudden contractions and expansions occurring along the whole fluid path. The dynamic range is thus given by

$$D = \frac{\Delta P_{\tau_{max}}}{(1+\zeta)\Delta P_{\eta}} = \frac{1}{1+\zeta} \cdot \frac{ch\alpha\pi g^2}{\mu_0\mu_{MR}3\eta Q} \cdot \frac{1+2r_i/(r_e+r_i)}{h/r_i + \ln(r_e/r_i)} B_{MR}. \quad (3.44)$$

Efficiency

In order to compute the power consumption as a function of the magnetic induction, the same procedure used in the previous section can be applied. In this case, we have that the total length of the magnetic field path crossing the MR fluid double and, consequently, the overall reluctance associated to the active regions increases of a factor 2. Thus, in order to maintain the same magnetic potential Θ_{MR} due to an equivalent increase of the length of the magnetic field path crossing the MR fluid, the Joule losses double, in reason of a proportional augmentation of the coil surface S_{coil} . This leads

$$W_{Joule} = \frac{1}{\sigma} \frac{8\pi\bar{r}_c g \rho J}{\mu_0\mu_{MR}} B_{MR} \quad (3.45)$$

and the valve efficiency becomes

$$\varepsilon = \frac{\Delta P_{\tau_{max}}}{W_{Joule}} = \frac{ch\alpha [1+2r_i/(r_e+r_i)] \sigma}{4\pi\bar{r}_c g^2 \rho J}. \quad (3.46)$$

Reactivity

The annular-radial valve time constant can be determined using the same approach previously introduced, which gives, by mean of (3.26)

$$\tau_{coil} = \frac{L}{R_w} = \frac{N^2}{\mathcal{R}_T} \frac{1}{R_w} = \frac{2g}{\mu_0\mu_{MR}\pi\bar{r}_c\rho J} \frac{B_{MR}}{\sigma\mathcal{R}_T}. \quad (3.47)$$

Finally, the valve reactivity is defined as

$$\mathcal{R} = \frac{\Delta P_{\tau_{max}}}{\tau_{coil}} = \frac{c\alpha\pi\bar{r}_c h}{g^2} \left(1 + \frac{2r_i}{r_e+r_i}\right) \rho J \sigma \mathcal{R}_T. \quad (3.48)$$

3.4 Design Methodology for MR Valves

The derived relations allow to solve the valves design for each configuration imposing as inputs (other than the fluid, the coil and iron intrinsic parameters) the pressure drop $\Delta P_{\tau_{max}}$, the dynamic range D , the flow rate Q and the current density J .

3.4.1 Design equations assuming magnetic flux conservation

Under the hypothesis of magnetic flux conservation, it is possible to write a characteristic system of equations for each valve configuration which can be easily solved employing an iterative nonlinear solver. For each system, the two first relations define the $\Delta P_{\tau_{max}}$ and D , while the third one takes in consideration simultaneously the coil dimensions and the constraints to avoid the saturation of the magnetic valve elements. For what concerns the annular valve, three different parameters (r_g , g_a and h) result to be unknown and have to be determined. Thus, a system of three equations has to be settled

$$\begin{cases} \Delta P_{\tau_{max}} = \frac{4ch\alpha}{\mu_0\mu_{MR}g_a} B_{MR} \\ D = \frac{cg_a^2\pi r_g\alpha}{\mu_0\mu_{MR}3\eta Q} B_{MR} \\ \left(r_g - \sqrt{2r_g h\zeta}\right)^2 = \frac{1}{\sigma} \frac{2g_a}{\mu_0\mu_{MR}J\chi} B_{MR}. \end{cases} \quad (3.49)$$

Considering the radial configuration, an approach similar to the aforementioned is used to determine the geometrical parameters g_r , r_i and r_e , but the system of equation is augmented to adequately dimension the gap n

$$\begin{cases} \Delta P_{\tau_{max}} = \frac{4c(r_e - r_i)\alpha}{\mu_0\mu_{MR}g_r} B_{MR} \\ D = \frac{1}{1+\xi} \cdot \frac{c(r_e - r_i)\pi g_r^2\alpha}{\mu_0\mu_{MR}6\eta Q \cdot \ln(r_e/r_i)} B_{MR} \\ \left(r_i - n - \zeta\sqrt{r_e^2 - r_i^2}\right)^2 = \frac{1}{\sigma} \frac{2g_r}{\mu_0\mu_{MR}J\chi} B_{MR} \\ \xi \cdot \frac{\Delta P_{\tau_{max}}}{D} = \frac{6\eta Q \left(\sqrt{\frac{1}{\sigma} \frac{2g_r}{\mu_0\mu_{MR}J\chi} B_{MR} - 2g_r}\right)}{\pi(r_i - n)n^3} \end{cases} \quad (3.50)$$

where ξ is a coefficient defining the relevance of the viscosity dependent pressure drop across the inner annular channel of width n with respect to the overall ΔP_{η} estimated for the valve active regions.

For what concerns the annular radial configuration, the unknown parameters are g , h , r_i and r_e which can be determined solving the following system

$$\left\{ \begin{array}{l} \Delta P_{\tau_{max}} = \frac{4ch\alpha}{\mu_0\mu_{MR}g} [1 + 2r_i/(r_e + r_i)] B_{MR} \\ D = \frac{1}{1+\zeta} \cdot \frac{ch\alpha\pi g^2}{\mu_0\mu_{MR}6\eta Q} \cdot \frac{1+2r_i/(r_e+r_i)}{h/r_i + \ln(r_e/r_i)} B_{MR} \\ h = \frac{r_e^2 - r_i^2}{2r_i} \\ \xi \cdot \frac{\Delta P_{\tau_{max}}}{D} = \frac{8\eta Q h_c}{\pi r_i^4} = \frac{16\eta Q \sqrt{\frac{1}{\sigma} \frac{2g}{(\mu_0\mu_{MR} J\chi)}} B_{MR}}{\pi r_i^4} \end{array} \right. \quad (3.51)$$

Similarly to what has been done for the radial configuration, a further constraint on the internal radius r_i has been added by mean of the last relation in (3.51) in order to impose a pressure drop across the most internal cylindrical duct affecting the less possible the overall dynamic range.

3.4.2 Design equations extension for the inclusion of HFMEC

As announced in the introduction of section 3.3 and recalled in subsection 3.4.1, the introduced design equations assume as a starting point the magnetic flux conservation. This hypothesis is required in the case that an equivalent magnetic circuit modelling the valve is missing (for example in the case that a rough approximation considering only the reluctance associated to the MR channels is done). Without this assumption, the systems of equations introduced in (3.49), (3.50) and (3.51) would be under-constrained and their solution undetermined.

On the contrary, in the case that more precise information on the magnetic circuit are available through the employing of an equivalent model, the relations previously defined can be improved. This can be done considering the actual magnetic fluxes crossing a particular valve section and the imposed limits of saturation induction. For example, if the annular geometry is considered (Fig. 3.1), the formulations defining the inner core radius r_c and the outer magnetic core r_o can be extended as follows

$$r_c = \sqrt{2r_g h \zeta} \quad \longrightarrow \quad r_c = \sqrt{\frac{\zeta \phi_T}{\pi B_{MR}}} \quad (3.52)$$

$$r_o = \sqrt{(r_g + g_a)^2 + 2r_g h \zeta} \quad \longrightarrow \quad r_o = \sqrt{\frac{\zeta \phi_{ext}}{\pi B_{MR}} + (r_g + g_a)^2} \quad (3.53)$$

where ϕ_T is the total magnetic flux which is assumed to completely cross the inner magnetic core, while ϕ_{ext} is the fraction traversing the external magnetic core, which are easily achiev-

able using the equivalent model introduced in chapter 2.

Moreover, the introduction of the HFMEC allows to precisely determine the value of σ defining the fraction of the overall magnetic potential drop actually participating to the creation of B_{MR} and improve the estimation of the related quantities derived in the previous sections.

3.4.3 Complete design routine

In reason of the considerations introduced so far, the overall implementation of the design routine is composed of two parts:

1. The valve geometry is initially dimensioned considering the formulations introduced in subsection 3.4.1 and assuming that the total magnetic potential drop is applied across the valve channels ($\sigma = 1$). Then, the remaining relevant geometric parameters are computed to comprehensively constrain the structure.
2. Once the geometry is completely defined, the HFMEC is used to determine the magnetic quantities of relevance (namely σ and the magnetic fluxes of interest) which are used to correct the previous design, as described in subsection 3.4.2. This last point is repeated till convergence is reached.

The threshold for convergence is defined by the relative error between the value of σ_n computed at the current iteration n and the value σ_{n-1} at the previous iteration cycle $n - 1$.

Figure 3.4 proposes a schematic representation which resumes the design methodology presented so far applied to the annular configuration.

3.4. Design Methodology for MR Valves

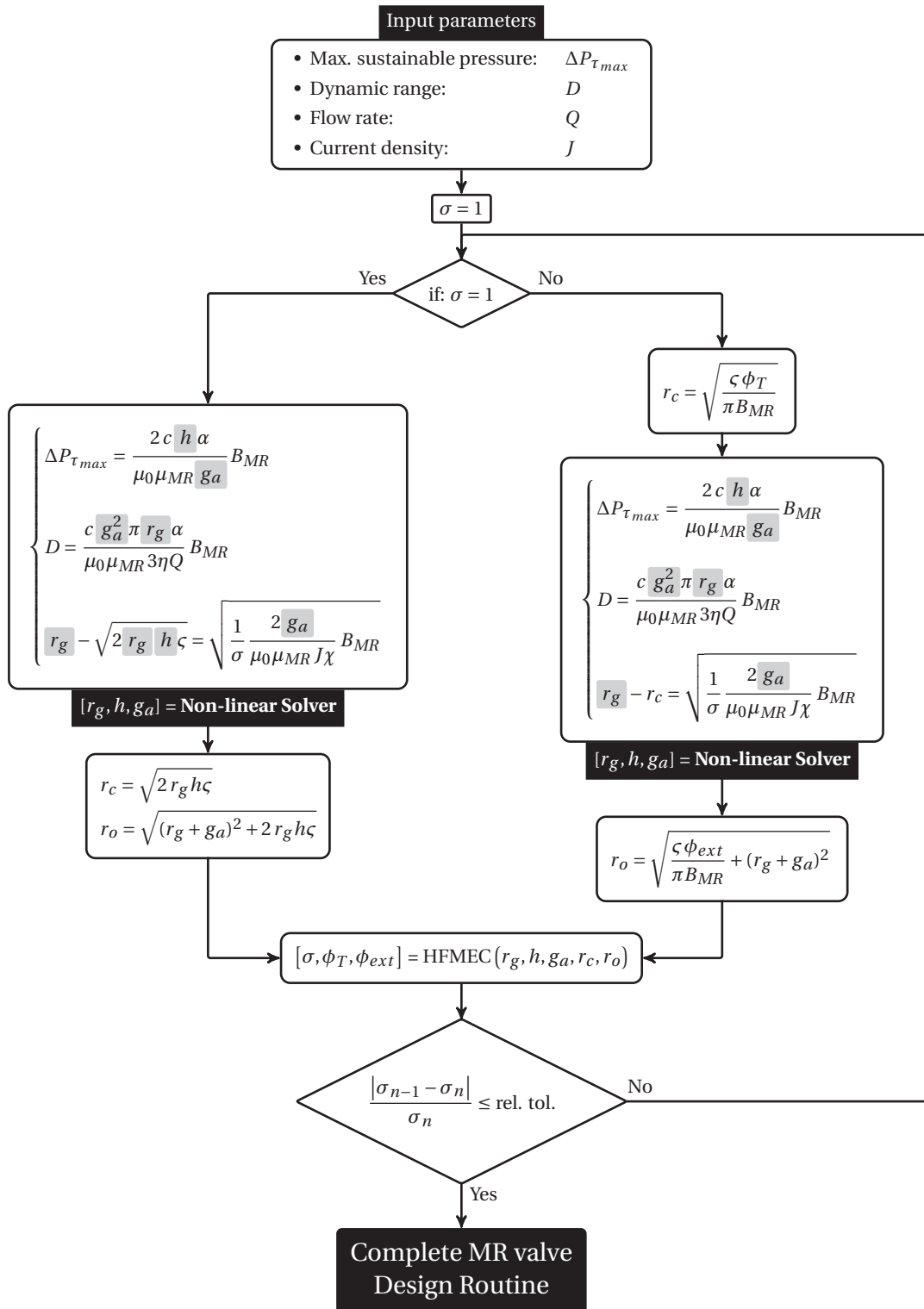


Figure 3.4 – Schematic representation of the approach used to implement the proposed design methodology for an annular MR valve.

3.5 Results

In order to compare the performances of the different valves typologies, the dimensioning routine discussed in the previous section is used to build two sets of valves for each configuration in order to fulfil some imposed design constraints.

For what concerns the design requirements, the flow rate has been fixed to be $Q = 0.1 \text{ [dm}^3 \cdot \text{s}^{-1}\text{]}$ and the current density imposed to $J = 6 \text{ [A} \cdot \text{mm}^{-2}\text{]}$ (this value is used to ensure the avoidance of overheating of the coil for uninterrupted supply), while the other input quantities are varied accordingly to the two following *design scenarios*:

1. D from 1 to 20 and ΔP_τ fixed to 700 kPa
2. D fixed to 10 and ΔP_τ from 700 kPa to 2 MPa.

The following table resumes the remaining design parameters required to complete the dimensioning equations. The latter mainly consist in the intrinsic properties of the materials composing the valve structures.

Name	Description	Value
B_{MR}	MR fluid saturation induction limit	0.5 [T]
B_{iron}	Iron saturation induction limit	1.7 [T]
χ	Coil filling factor	0.7
ρ	Copper resistivity	0.35 [$\Omega \cdot \text{m}$]
η	Viscosity	0.092 [$\text{Pa} \cdot \text{s}$]
c	Correction parameter	2.5
ζ	Loss coefficient	0.7
ξ	Relevance of ΔP_η for the non-active regions	0.05

Table 3.1 – Intrinsic properties of the materials composing the valves structures. The fluid considered is the MRF132CG by Lord.

The devices obtained from the dimensioning routine are modelled in a FE software. This means that the the same geometrical structures, physical properties and boundary conditions considered in the analytical routine are reproduced for the FE simulations. The obtained results are compared to the analytical models with respect to the figures of merit defined in section 3.2 in order to assess the reliability and determine the quality of the design methodology proposed.

Dynamic range

Figure 3.5 displays the trend of the dynamic ranges D_i with respect to the total valve volume V_{tot} of the valves obtained solving the *design scenario #1*, for which the maximum sustainable pressure drop $\Delta P_{\tau_{max}}$ is fixed to 700 kPa, while the imposed D is varied from 1 to 20 with increments of 1.

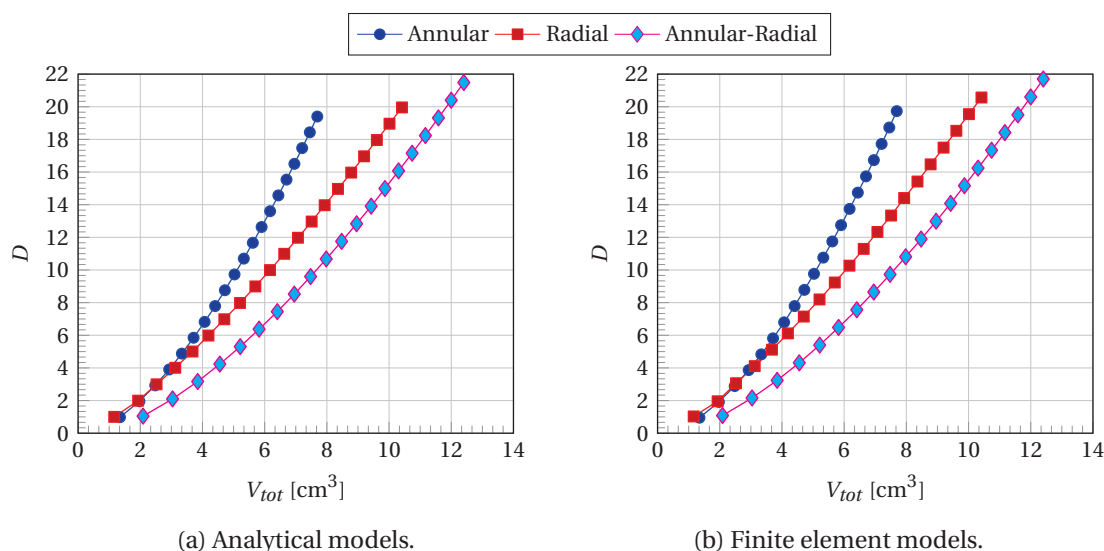


Figure 3.5 – Comparison of the different dynamic ratios of the MR valves configurations.

The main evidence provided by Fig. 3.5 is that annular and radial valves provide, in this order respectively and despite a slight difference, higher dynamic ratios with respect to annular-radial valves for the same valve volume.

For what concerns the comparison between analytical and FE models results, the characteristics appear to be almost equal and the maximum relative errors related to each valve configuration remain small, as shown in the following table.

Annular		Radial		Annular-Radial	
$\max\{\varepsilon_{D_i}\}$	$\bar{\varepsilon}_{D_i}$	$\max\{\varepsilon_{D_i}\}$	$\bar{\varepsilon}_{D_i}$	$\max\{\varepsilon_{D_i}\}$	$\bar{\varepsilon}_{D_i}$
[%]	[%]	[%]	[%]	[%]	[%]
3.2	1.1	3.1	2.3	3.5	1.5

Table 3.2 – Maximum ($\max\{\varepsilon_{D_i}\}$) and mean ($\bar{\varepsilon}_{D_i}$) relative errors between FE analysis and analytical model results for the valves dynamic ranges D .

Pressure to volume ratio

The characteristics of the pressure to volume ratios κ_i , i.e. the pressure densities, with respect to the overall valves volume corresponding to each configuration obtained with the analytical

Chapter 3. Design and Comparison of Different MR Valves Configurations

design routine and from FE analysis are shown in Figure 3.6. In particular, the valves sets compared in the following subsections have been obtained from the *design scenario #2* for which the dynamic ratio D has been fixed to 10 while the maximum sustainable pressure $\Delta P_{\tau_{max}}$ is varied from 700 kPa to 2 MPa with increments of 50 kPa.

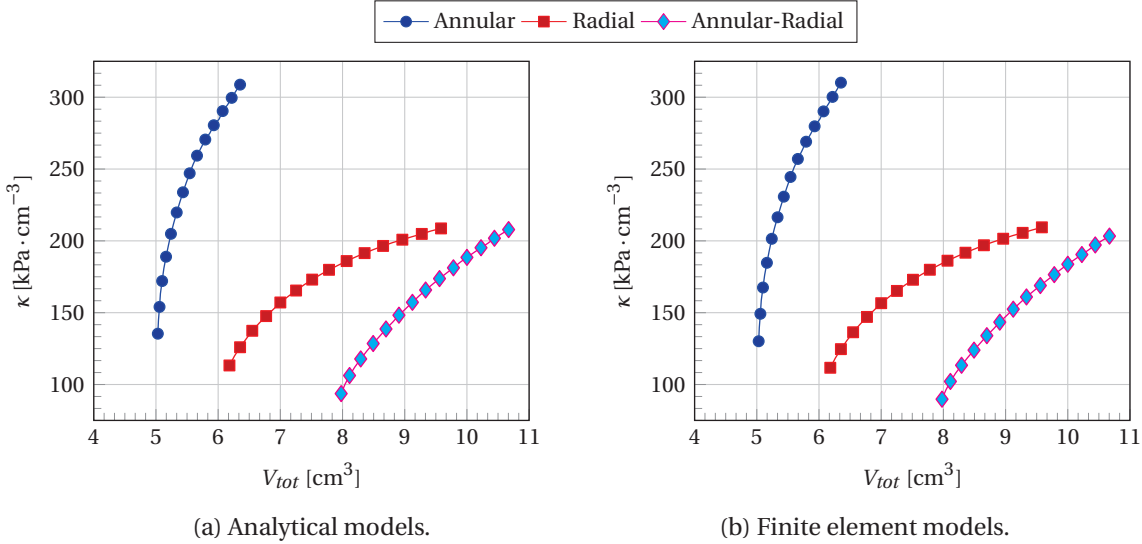


Figure 3.6 – Comparison of the different pressure densities of the MR valves configurations.

The annular configuration clearly offers the best pressure to volume ratio, being able to sustain high pressures still remaining relatively small. In fact, the range of maximum sustainable pressure $\Delta P_{\tau_{max}}$ is obtained without a large variation of the valve size.

On the contrary, for radial and annular-radial configurations the pressure density grows more slowly. A possible explanation of this trends can be done considering that the losses coefficients imposed to achieved the desired dynamic range irremediably affect the overall valve volume, drastically increasing it. Moreover, the inactive regions of the valves channels, namely the parts in which the fluid is supposed to not be crossed by relevant magnetic fields, are characterised by higher volumes which compromise again the pressure density.

Table 3.3 lists the mean and maximum relative errors computed comparing the analytical and FE model results.

Annular		Radial		Annular-Radial	
$max\{\varepsilon_{\kappa_i}\}$	$\bar{\varepsilon}_{\kappa_i}$	$max\{\varepsilon_{\kappa_i}\}$	$\bar{\varepsilon}_{\kappa_i}$	$max\{\varepsilon_{\kappa_i}\}$	$\bar{\varepsilon}_{\kappa_i}$
[%]	[%]	[%]	[%]	[%]	[%]
3.9	1.4	1.4	0.4	4.3	3.2

Table 3.3 – Maximum ($max\{\varepsilon_{\kappa_i}\}$) and mean ($\bar{\varepsilon}_{\kappa_i}$) relative errors between FE analysis and analytical model results for the valves pressure to volume ratios κ .

Reactivity

Figure 3.7 displays the trends of the reactivity \mathcal{R}_i related to the different valves configurations with respect to their volumes.

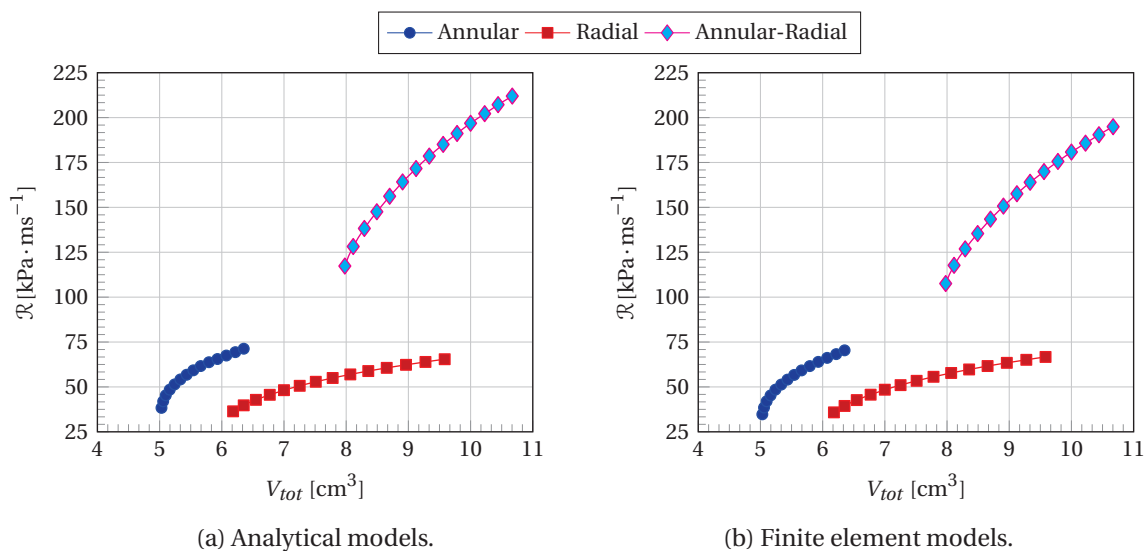


Figure 3.7 – Comparison of the different reactivities of the MR valves configurations.

To better specify the role of this figure of merit, it can be said that reactivity describes the time required for a certain valve to set a sufficiently high level of magnetic flux density B_{MR} in its channels to completely sustain a certain pressure. It must be underlined that, in order better define the real dynamic characteristic of the valves discussed, it should be necessary to evaluate simultaneously the electromagnetic and fluidic response. Nevertheless, information provided with this comparison may help to set initial considerations to choose one configuration with respect to another.

The annular-radial configuration clearly offers the higher reactivity with values which cannot be achieved with the other valves geometries. In fact, it can be observed that, even in the case of imposing a volume augmentation for the annular and radial configurations to extend the curves, the annular-radial reactivity characteristic will not be even crossed.

This outcome can be explained considering that four active regions are present in an annular-radial valve which results in a lower value of the overall permeance and, consequently, a lower

Annular		Radial		Annular-Radial	
$max\{\varepsilon_{\mathcal{R}_i}\}$	$\bar{\varepsilon}_{\mathcal{R}_i}$	$max\{\varepsilon_{\mathcal{R}_i}\}$	$\bar{\varepsilon}_{\mathcal{R}_i}$	$max\{\varepsilon_{\mathcal{R}_i}\}$	$\bar{\varepsilon}_{\mathcal{R}_i}$
[%]	[%]	[%]	[%]	[%]	[%]
10.4	4.9	1.9	1.1	9.1	8.9

Table 3.4 – Maximum ($max\{\varepsilon_{\mathcal{R}_i}\}$) and mean ($\bar{\varepsilon}_{\mathcal{R}_i}$) relative errors between FE analysis and analytical model results for the valves reactivities \mathcal{R}_i .

Chapter 3. Design and Comparison of Different MR Valves Configurations

coil time constant with respect to the annular and radial topologies, which present only two active regions. Table 3.4 lists the mean and maximum relative errors computed comparing the analytical and FE model results.

Efficiency

Figure 3.8 displays the trends of the efficiency \mathcal{E}_i related to the different valves configurations with respect to their volumes, which define the amount of power, i.e. Joule losses, required by the valve to sustain its maximum pressure $\Delta P_{\tau_{max}}$.

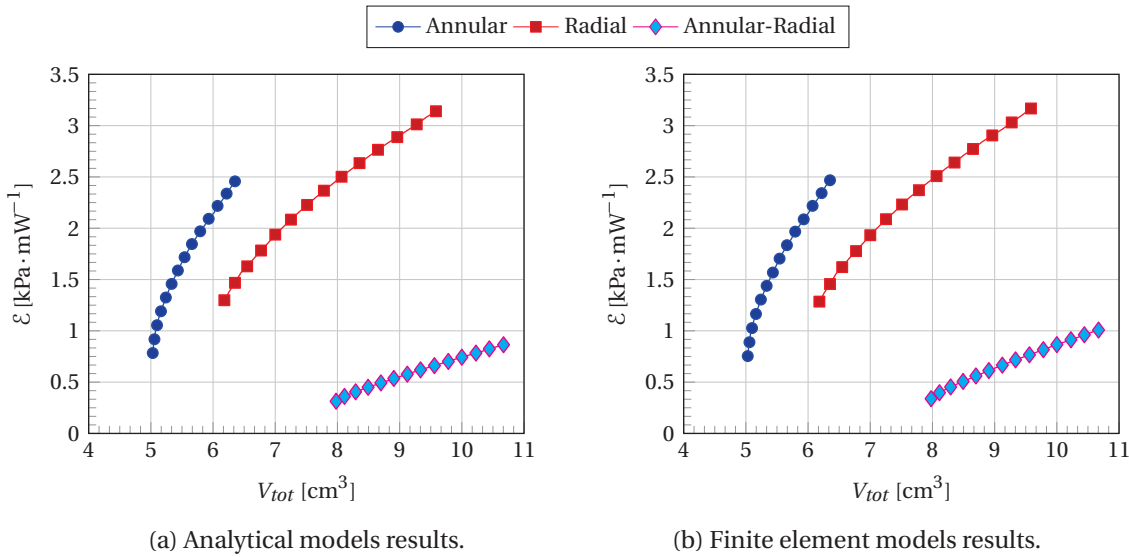


Figure 3.8 – Comparison of the different efficiencies of the MR valves configurations.

As expected, annular-radial valves are characterised by the worst efficiency. This is mainly due to the higher magnetic potential required to obtain the imposed B_{MR} in the four active regions. Moreover, the coil dimensions are bigger with respect to the other configurations for which the valve channels are located externally to the coil.

On the contrary, radial valves offer the best overall efficiency, but they are overtaken by the annular configuration if the overall valve volume is also considered.

Table 3.5 resumes the mean and maximum relative errors computed comparing the analytical and FE model results. In this respect, while for annular and radial configuration both the displayed errors remain low, this is not the case for the annular-radial configuration. This outcome is mainly related to the fact that the Joule losses of the analytical models are computed according to (3.45) in which only a value of B_{MR} appears. However, it has been shown through the comparison of the different magnitudes of B_{MR} given in section 2.4 that the assumption of having the same magnetic flux density in all the valves channels is not valid for annular-radial valves, and the magnitude of B_{MR} in their radial ducts is higher than the design target. This leads to an overall higher $\Delta P_{\tau_{max}}$ obtained through FE analysis which can explain the related large errors present in Table 3.5. Nevertheless, it has to be underlined that it is only the

Annular		Radial		Annular-Radial	
$\max\{\varepsilon_{\mathcal{E}_i}\}$	$\bar{\varepsilon}_{\mathcal{E}_i}$	$\max\{\varepsilon_{\mathcal{E}_i}\}$	$\bar{\varepsilon}_{\mathcal{E}_i}$	$\max\{\varepsilon_{\mathcal{E}_i}\}$	$\bar{\varepsilon}_{\mathcal{E}_i}$
[%]	[%]	[%]	[%]	[%]	[%]
3.4	1.3	1.1	0.4	14.3	12.5

Table 3.5 – Maximum ($\max\{\varepsilon_{\mathcal{E}_i}\}$) and mean ($\bar{\varepsilon}_{\mathcal{E}_i}$) relative errors between FE analysis and analytical model results for the valves efficiencies \mathcal{E}_i .

definition of \mathcal{E}_i given in (3.45) to be inaccurate. The HFMEC used to model the annular valve configuration has demonstrated to be able to well describe the magnetic induction levels in all the valve ducts. Consequently, it would be preferable to use the direct results from the HFMEC, rather than (3.45), for the computation of the overall valve efficiency.

3.6 Summary and conclusion

In this chapter the design and the comparison of three different MR valves configurations have been proposed. More in details, the analysis performed in the initial part of the chapter has allowed to define four different figures of merit, namely the dynamic range D , the pressure to volume ratio κ , the valves reactivity \mathcal{R} and their efficiency \mathcal{E} to compare the different configurations and give some further information to the reader in relation to their advantages and drawbacks.

The design methodology presented throughout this chapter has proven its reliability when the different figures of merit obtained directly using the defined analytical relations have been compared with FE analysis results. The main contribution to justify this high level of accuracy is related to the use of the HFMEC introduced in the previous chapter, which represents a fundamental element in the design routine proposed for the dimensioning of MR valves. In this respect, the methodology presented here completely fulfil the intended objectives of providing the main guidelines for the design, the analysis and the successive comparison of MR valves, while building a reliable tool for their dimensioning, in the perspective of a successive refinement/optimisation, if required.

Last but not least, another important aspect of the introduced approach, which lies under the main contents presented in this chapter, is related to the possibility of directly transfer it to the dimensioning of any MR-based device. In fact, both the principles and the main steps of the design methodology proposed have been put in place with a particular effort to allow easy extension to geometries and devices having similar features.

Publications related to this chapter:

- D. Grivon, Y. Civet, Z. Pataky and Y. Perriard, *Design and comparison of different Magneto-Rheological valves configurations*, Advanced Intelligent Mechatronics (AIM), ASME/IEEE International Conference on, pp. 818-823, Busan, 2015.

Bibliography

- [1] M. Avraam, M. Horodincea, I. Romanescu and A. Preumont, *Computer Controlled Rotational MR-brake for Wrist Rehabilitation Device*, Journal of Intelligent Material Systems and Structures, Vol. 21, pp. 1543-1557.
- [2] C. Rossa, A. Jaegy, J. Lozada and A. Micaelli, *Design Considerations for Magneto-rheological Brakes*, Mechatronics, IEEE/ASME Transactions on, Vol. 19, No. 5, October 2014.
- [3] J.-H. Yoo and N. Wereley, *Design of a High-Efficiency Magnetorheological Valve*, Journal of Intelligent Material Systems and Structures, Vol. 13, October 2002.
- [4] Q.-H. Nguyen, Y.-M. Han and N. M. Wereley, *Geometry optimisation of MR valves constrained in a specific volume using the finite element method*, Smart Materials and Structures, No. 16, 2007.
- [5] Q.-H. Nguyen, S.-B. Choi and N. M. Wereley, *Optimal design of magneto-rheological valves via a finite element method considering control energy and a time constant*, Smart Materials and Structures, No. 17, 2008.
- [6] C. S. Zhu, *The response time of magneto-rheological fluid squeeze film damper rotor system*, Key Eng. Material., pp. 1085-1088, 2007.
- [7] M. Jufer, *Traité d'Electricité, Volume IX: Electromécanique*, Presses Polytechniques Universitaires et Romandes, 1995.
- [8] F. M. White, *Fluid Mechanics - Seventh Edition*, McGraw-Hill Series in Mechanical Engineering, 2010.

4 Dynamic Modelling and Sensing Possibilities of MR Valves

In this chapter the dynamic modelling and the sensing possibilities of MR-based devices are addressed, using as privileged case of study MR valves. In particular, bond graph based physical system modelling is used to describe the studied system.

After an initial introduction containing a preliminary definition of bond graphs as well as the main motivations for which this analysis tool has been chosen, a summary discussion of the main features and rules governing of this modelling technique is given. The introduced notions are used for the dynamic modelling MR valves, choosing the annular configuration as the preferred topology under analysis.

Further than providing a description of the system, the bond graph methodology and analogies with well-known transducers will suggest the intrinsic sensing possibilities of MR-based devices. The latter will be firstly justified indirectly, i.e. discussing state of the art results present in literature on the behaviour of MR fluids. Finally, dedicated test sessions will provide experimental evidences of the expected phenomena.

4.1 The Bond Graph modelling approach

Bond graph modelling is an intuitive and graphical approach used to describe dynamic systems [1]. The different elements (subsystems and basic components) constituting the physical system under study are defined as the *nodes* of the bond graph while their interactions, which actually defines the instantaneous exchange of energy among the system elements, are depicted as interconnection edges called *power bonds*. Depending on the number of interactions occurring, each node has a certain number of *ports* to which the bonds are connected.

Among the main advantages brought by the successive steps required to build a complete bond graph model, we can list

1. the topological affinity between the bond graph representation and the physical structure of the system under study
2. an easy and comprehensive representation of the different physics involved using the same elements and generalised physic quantities
3. the possibility to derive the governing equations directly from the graphical representation obtained.

Thus, bond graph modelling offers at the same time a high level of abstraction, which allows for an intuitive and *qualitative* understanding of the system behaviour, while keeping the possibility to further extend the analysis through the definition of the differential equations describing *quantitatively* the phenomena involved, mainly for simulation or control purposes. This is a non-negligible advantage which is not so straightforward in other approaches used to describe dynamic systems, like for example the "*energy method*" of the Lagrange's equations. Last, but not least, the systematic bond graph construction through the aforementioned steps may bring out constitutive multi-physics relations which are not always straightforward. In this respect, bond graph modelling does not only represent an approach merely intended to describe real systems, but it can also be used as an investigation tool, this last aspect covering a particular relevance in the research work presented hereafter.

These are the main motivations which, together with a personal preference for intuitive graphical representation, justify the choice of this modelling approach.

4.1.1 Bond Graph Variables and Physical Analogies

As previously introduced, bond graphs describe the instantaneous power exchanges which take place in a physical system. The amount of power $P(t)$ flowing through a bond connecting the ports of two different elements can be expressed as

$$P(t) = e(t) \cdot f(t) \tag{4.1}$$

4.1. The Bond Graph modelling approach

where $e(t)$ and $f(t)$ represent respectively the *power conjugated variables* defining the *effort* and the *flow*. The *direct* or *classical* analogy, for which forces and voltage are efforts while velocities and current are flows, will be assumed henceforth.

Two additional *energy variables* are required to complete the list of physical quantities employed within the bond graph methodology, which are the *generalized displacement* q and the *generalized momentum* p

$$q(t) = q(t_0) + \int_0^t f(\tau) d\tau \quad (4.2)$$

$$p(t) = p(t_0) + \int_0^t e(\tau) d\tau. \quad (4.3)$$

These variables quantify the amount of energy that within a certain period is accumulated in an ideal energy store. Table 4.1 lists the power and energy variables related to the different physics encountered in the addressed system.

Energy domain	Effort e	Flow f	Generalized momentum p	Generalized displacement q
Translational mechanics	Force F [N]	Velocity v [m · s ⁻¹]	Momentum p [N · s]	Displacement x [m]
Electro -	Voltage u [V]	Current i [A]	Linkage flux λ [V · s]	Charge q [A · s]
Magnetics	Magnetomotive force Θ [A]	Magnetic flux rate $\dot{\phi}$ [Wb · s ⁻¹]	-	Magnetic flux ϕ [Wb]
Hydraulics	Total pressure P [N · m ⁻²]	Flow rate Q [m ³ · s ⁻¹]	Pressure momentum P_p [N · s · m ⁻²]	Volume V [m ³]

Table 4.1 – Energy domains and related bond graph variables.

4.1.2 Bond Graph Elements

In the following a summary presentation of the main bond graph elements that will be used to describe the studied system is given. Its objective is to introduce their graphical representation as well as summarise their features.

Bonds representation and computation causality

A sign convention denoting the reference orientation of power bonds is required to correctly represent power flow. Bonds connecting elements which supply power to the system are represented with an *half arrow* oriented apart from the element. On the contrary, for components employing the system power, the reference direction is defined positive if the bond is oriented towards the port.

The two power conjugated variables, i.e. the effort and the flow, are assigned to each bond connecting two power ports. In order to define a perspective of analysis we have to choose which power variable is imposed to one element and which one is derived from it. This is called an assignment of *computational causality*. A straight line perpendicular to the direction of the bond and placed on the same side of the element which defines the flow variable is the convention to represent the assignment of causality (Fig. 4.1).

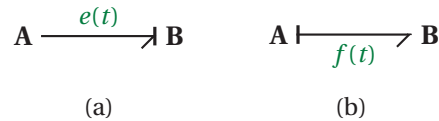


Figure 4.1 – (a) - Causality for an effort determined/imposed by the element **A**. (b) - Causality for a flow determined/imposed by the element **A**. In both the cases element **A** supplies power to element **B**.

Bond graph elements

Five different n -ports elements (i.e. elements with one or more ports) are used to build a bond graph:

1. **power junctions**: nodes used to split power coming from external sources to the system elements
2. **energy stores**: elements able to store energy under the form of generalised displacement (1-port C elements) or generalised momentum (1-port I elements)
3. **dissipators**: represent the energy losses in the system
4. **energy sources (or sinks)**: define the system boundaries and its interactions with the surrounding environment
5. **couplers**: transformers and gyrators are examples of n -ports elements converting energy with neither storing nor dissipating it.

Table 4.2 lists all the basic elements introduced together with their graphical representation and the main constitutive relations. A comprehensive description together with some illustrative examples are available in Appendix C.

4.1. The Bond Graph modelling approach

Element	Representation	Constitutive equations
0 - junction		$e_1 = e_2 = \dots = e_n$ $f_1 = f_2 + \dots + f_n$
1 - junction		$f_1 = f_2 = \dots = f_n$ $e_1 = e_2 + \dots + e_n$
Effort source		$S_e = E(t)$
Flow source		$S_f = F(t)$
Dissipator		$e(t) = \phi_R(f(t))$
		$f(t) = \phi_G(e(t))$
1-port C element		$e(t) = \phi_C^{-1} \left(\int_0^t f(\tau) d\tau \right), \quad q(t) = \phi_C(e(t))$
		$f(t) = \frac{d}{dt} \phi_C(e(t)) = \frac{d\phi_C}{de} \dot{e}(t)$
1-port I element		$f(t) = \phi_I^{-1} \left(\int_0^t e(\tau) d\tau \right), \quad p(t) = \phi_I(f(t))$
		$e(t) = \frac{d}{dt} \phi_I(f(t)) = \frac{d\phi_I}{df} \dot{f}(t)$
2-port TF element (Transformer)		$e_1(t) = m \cdot e_2(t)$
		$f_2(t) = m \cdot f_1(t)$
2-port GY element (Gyrator)		$e_1(t) = w \cdot f_2(t)$
		$e_2(t) = w \cdot f_1(t)$

Table 4.2 – Bond graph elements, corresponding representation and constitutive relations.

4.2 A useful case study: the electromagnet as a transducer

The 2-ports elements introduced so far (i.e. transformers and gyrators) satisfy the power conservation principle, conveying energy without neither consuming nor storing it. Differently, transducers are elements in which the conversion from one energy domain to another happens with energy storage in one, or both, the domains involved. This is possible through the assumption of energy conservation.

In order to better clarify this concept and the basic elements introduced so far, the example of an electromagnet (Fig 4.2) is given as a particularly useful and interesting case study [2]. In this respect, the concepts as well as the analysis steps presented in the following section will be directly transferred, mainly by mean of analogies, to the modelling of the MR valves.

Let's consider the schematic diagram of Fig. 4.2 and initially focus the attention on the electromagnetic part only. The overall energy in the electromagnet is given by the sum of the electric and mechanic energy acting at its interfaces (variables time dependence is implicit)

$$E = \int (F \cdot v + e \cdot i) dt. \quad (4.4)$$

Imposing two of the power variables, i.e. we fix e and v , we obtain

$$E = \int \left(F \cdot \frac{dx}{dt} + \frac{d\lambda}{dt} \cdot i \right) dt = \int F \cdot dx + \int i \cdot d\lambda. \quad (4.5)$$

The energy in the electromagnet is a function of the linkage flux λ and of the displacement x . In order to solve the integrals in (4.6) we must choose an integration path for each variable. Considering that, as previously remembered, conservation of energy is assumed, the result will be independent from the path and the most suitable for an easy computation has to be chosen [3]. Fig. 4.3 depicts a convenient integration path on the plane $\lambda - x$.

Integration along the first part of the path (1) gives 0 because the linkage flux is imposed to be zero (no current flows in the coil, thus no energy can be stored or exchanged). Considering

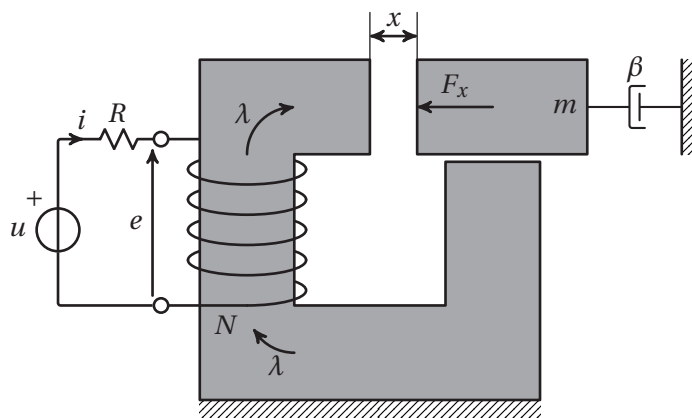


Figure 4.2 – Schematic representation of an electromagnet.

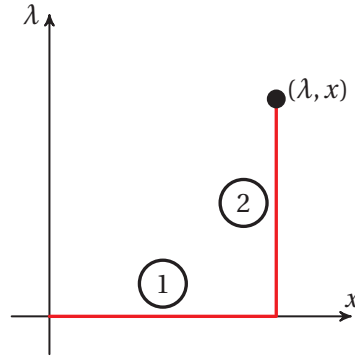


Figure 4.3 – Convenient integration path chosen.

the second part of the path (2), there is no change in the displacement and only the linkage flux varies. This leads to

$$E(\lambda, x) = \int i \cdot d\lambda. \quad (4.6)$$

Assuming that all the magnetic flux linked by the coil crosses the air gap of variable width x and if the magnetic potential drop in the iron cores can be considered negligible with respect to the one across the air gap, the coil current can be related to the magnetic flux ϕ by mean of the reluctance \mathcal{R} as follows

$$i = \mathcal{R} \frac{\phi}{N} = \mathcal{R} \frac{\lambda}{N^2}, \quad \text{where} \quad \mathcal{R} = \frac{x}{\mu_0 A}. \quad (4.7)$$

Inserting this last relation in (4.6) and solving the integral we obtain

$$E(\lambda, x) = \frac{1}{2} \frac{\lambda^2 x}{\mu_0 A N^2} \quad (4.8)$$

where A is the air gap cross-section. The derivation of the total energy stored in the electromagnet with respect to the energy variables x and λ gives us respectively

$$F_x = \frac{\partial E}{\partial x} = \frac{\lambda^2}{\mu_0 A N^2} = \frac{\mu_0 A (Ni)^2}{2x^2} \quad (4.9)$$

$$i = \frac{\partial E}{\partial \lambda} = \frac{\lambda x}{\mu_0 A N^2} \quad (4.10)$$

which represent the constitutive equations for the electromagnet. It is interesting to note that (4.9) relates the effort F and the generalised displacement x . This suggest that, on its mechanical side, the transducer behaves like a spring, storing mechanical energy in the structure, namely in the air gap, where the actual energy conversion takes place. Thus, this feature can be represented by a 1-port C element (see Table 4.2 or refer to C.2.1). For what concerns the electric side, the flow i and the generalised momentum p , i.e. λ , are related by (4.10), as typically 1-port I energy store does (see Table 4.2 or refer to C.2.2). Resuming all the consid-

Chapter 4. Dynamic Modelling and Sensing Possibilities of MR Valves

erations introduced so far, an electromagnet, which converts mechanical to electric energy storing them in its structure, can be represented by the following bond graph element.



Figure 4.4 – Bond graph representation of the electromagnet transducers imposing preferred integrative causalities on its ports.

It can be noted that both the power bonds are directed towards the transducer symbol, underlining that the main difference of this component with 2-ports power conservative elements listed in Table 4.2, is related to its capability to store energy rather than merely convey it.

The description of the electromagnet given up to this point can be further detailed if we consider that the coil wrapped around the magnetic core can be modelled as a gyrator which converts the energy from the electric to the magnetic domain. Its constitutive relations are

$$\Theta = Ni \quad (4.11)$$

$$e = N\dot{\phi}. \quad (4.12)$$

The latter allow to more precisely define the nature of the energy stored in the magnetic structure

$$E(\phi, x) = \frac{1}{2} \frac{x}{\mu_0 A} \phi^2 \quad (4.13)$$

which derived with respect to the magnetic flux ϕ and the displacement x gives

$$F_x = \frac{dE}{dx} = \frac{1}{2\mu_0 A} \phi^2 = \frac{\mu_0 A (Ni)^2}{2x^2} \quad (4.14)$$

$$\Theta = \frac{dE}{d\phi} = \frac{x}{\mu_0 A} \phi. \quad (4.15)$$

While (4.9) and (4.14) lead to, as expected, the same result, we have that both the sides of the transducer relate an effort (F for the mechanical and Θ for the magnetic part) with the corresponding generalised displacement (respectively x and ϕ). That is, both the ports can be represented by a C energy store. Consequently, the graph in Fig. 4.4 has to be modified with the introduction of the gyrator modelling the coil and the new defined 2-port transducer depicted hereafter.

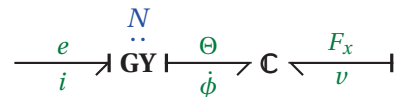


Figure 4.5 – Bond graph of the electromagnet transducer further detailed introducing the gyrator describing the coil. Integrative causalities are imposed on its ports.

Finally, combining (4.11), (4.12) and (4.15) we can determine the induced voltage e as

$$e = \frac{N^2 \mu_0 A}{x} \frac{di}{dt} - \frac{N^2 \mu_0 A i}{x^2} \frac{dx}{dt}. \quad (4.16)$$

The concept of transduction relies on this last relation which underlines how the variables at the transducers boundaries are linked among them. This implies that the signals of the mechanical domain can be *transduced* in the electrical domain.

A complete bond graph model can be built if we consider that all the components of the electrical domain (the voltage source, the resistor and the coil) share the same current i , namely the same flow. Consequently, they can be connected using a 1-junction. The mechanical elements that have to be considered describe the moving part of the electromagnet. The mass is taken into account by an inertial component, while the coulomb friction between the different electromagnet parts are modelled by a viscous damper, i.e. a mechanical dissipator. All the mechanical elements are characterised by the same velocity, i.e. the same flow, and, consequently they are connected by a 1-junction. The system interfaces with the surroundings are represented by two effort sources which account for the supply voltage u imposed to the coil and the force F_x acting on the electromagnet mover. The complete bond graph of the electromagnet is depicted in Fig. 4.6.

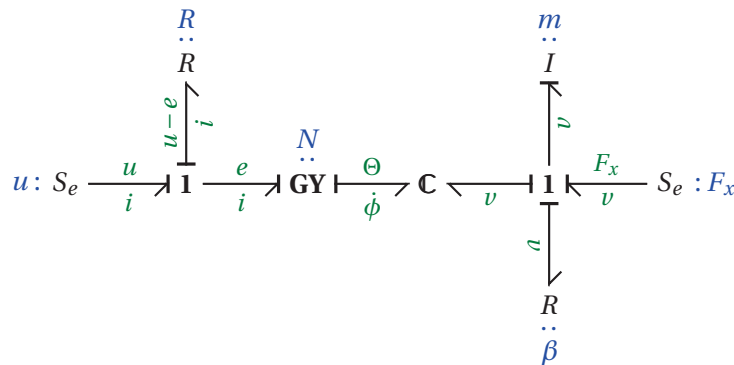


Figure 4.6 – Bond graph model of the electromagnet.

4.3 Bond Graph modelling of MR valves

After having introduced the elementary notions related to basic bond graph elements, the discussion can now focus on the modelling of the studied system. Initially, mainly for reasons of clarity, the two different physical domains encountered in MR valves, namely the hydraulic and the electro-magnetic, will be addressed separately and successively they will be joined in order to build a complete bond graph model describing the overall system. For what concerns this last step, the example of the electromagnet has been fundamental to suggest the synthesis of the two different models into a unique bond graph.

The comprehensive scenario given by the built model will allow to obtain at the same time an overview of the whole system and a detailed view of the phenomena occurring in the different physical domains, while maintaining a high level (i.e. macroscopic) description. Last, but not least, it can be anticipated that the analysis conducted to define a MR valve bond graph will lead, as probably the most interesting scientific result, to the identification of the sensing possibilities of MR valves, which can be generally extended to every MR-based device. Although three different types of MR valves have been addressed throughout the previous chapters, only annular MR valves will be treated hereafter, the approach used being applicable to all the other two configurations and leading to bond graphs having exactly the same topology, but different values of the element parameters in relation to different geometrical structures.

4.3.1 Electro-magnetic domain modelling

Chapter 2 has discussed in detail the magnetic modelling of MR valves. In particular, a permeance network has been built to describe each magnetic structure corresponding to a certain valve topology.

Addressing more specifically the annular valve, the equivalent circuit represented in Fig. 2.9b can be transferred to a bond graph model [4] for which the different magnetic potentials Θ_i are the efforts, while the flows are represented by the variation of the magnetic fluxes $\dot{\phi}_i$ (Table 4.1). Consequently, recalling the definition of 1-port C energy store, we have that permeances can be represented as depicted in Fig. 4.7.

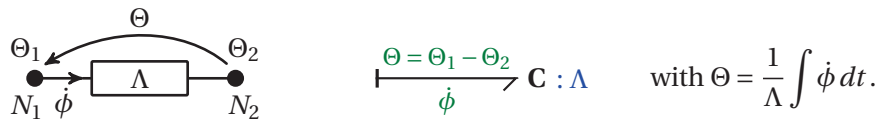


Figure 4.7 – From left to right: common equivalent representation of a permeance, bond graph representation of the corresponding 1-port C energy storage (with integrative causality) and associated characteristic equation.

It is interesting to note that, as already introduced discussing the electromagnet system, magnetic elements store energy under the form of magnetic flux ϕ , which represents the energy variable in magnetic systems, i.e. the generalised displacement for the magnetic domain. This evidence further strengthens the concept that leakage and fringing fluxes do not represent losses in the magnetic circuit. Furthermore, it helps to clarify the common misunderstanding, which may originate because of the analogy with electric circuits and the transposition of the Ohm’s law used to deal with magnetic circuits, that reluctances are dissipators. Losses in magnetic circuit are due to Eddy currents originating among the magnetic domains of the material itself which rise for high exciting frequencies. Magnetic losses will not be considered in the following analysis. Figure 4.8 shows the bond graph representation of the permeance network defined in chapter 2 for the annular valve.

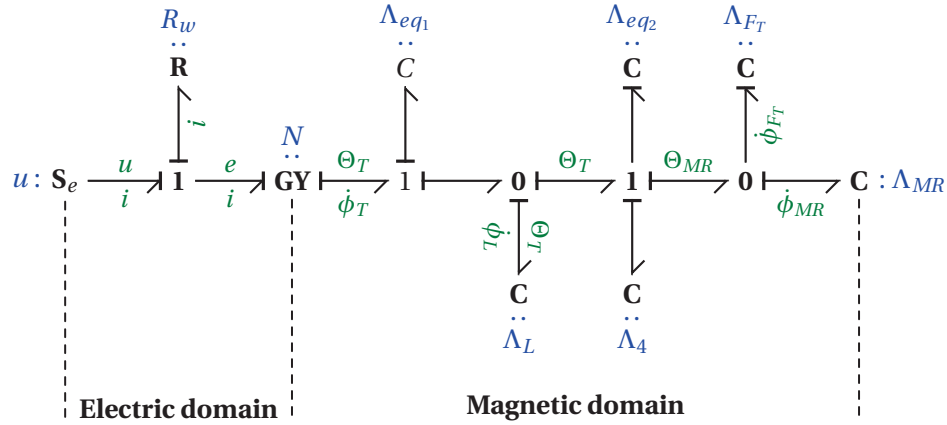


Figure 4.8 – Bond graph model of the electro-magnetic domains for the annular valve.

The equivalent permeances displayed in the bond graph model, which are obtained from topological simplifications, are respectively (their complete formulation has been presented in 2.3)

$$\Lambda_{eq1} = \left(\frac{2}{\Lambda_1} + \frac{2}{\Lambda_2} \right)^{-1} \quad \Lambda_{eq2} = \frac{\Lambda_3}{2} \quad \Lambda_{FT} = \frac{1}{2}(\Lambda_{F1} + \Lambda_{F2}) \quad \Lambda_{MR} = \frac{\Lambda_{ann}}{2}.$$

To enhance the understanding of the bond graph represented in Fig. 4.8 some of the relevant power conjugated variables are displayed on the respective power bonds. The coil represented by the gyrator imposes the magnetic flux rate $\dot{\phi}_T$ to the magnetic structure. Remembering that 0-junctions impose the same efforts and share the input flow, while 1-junctions realise the dual function, we have that the same magnetic potential drop is applied to Λ_{eq1} , Λ_L and the remaining circuit, in which the $\dot{\phi}_T$ is shared. The last 1-junction imposes the same magnetic flux rate to its linked elements and finally, we have that the latter is shared between the fringing permeances Λ_{FT} and the permeance of the annular MR channels. It is not a case that the end-effector of the magnetic part of the represented bond graph is Λ_{MR} . In fact, although all the permeances contribute to the magnetic energy storage, the amount of magnetic flux stored in the valve channels is of particular relevance because it is where the actual electromechanical conversion occurs.

4.3.2 Hydraulic domain modelling

In order to define the bond-graph model of the MR valve hydraulic domain, it is useful to recall the definition of the overall pressure drop across an annular MR valve given in (3.1)

$$\Delta P = \frac{2c\tau_y(H)(2h)}{g} + \frac{12\eta Qh}{g^3\pi r_g} = \Delta P_\tau + R_\nu Q \quad (4.17)$$

where R_ν is the hydraulic resistance of the valve due to the channel geometry and fluid viscosity. A graphical representation of this characteristic is given in Fig. 4.9a. If, inversely to

what considered up to this point, we express the flow rate through the valve Q as a function of the total pressure drop ΔP , we obtain the curve depicted in Fig. 4.9b.

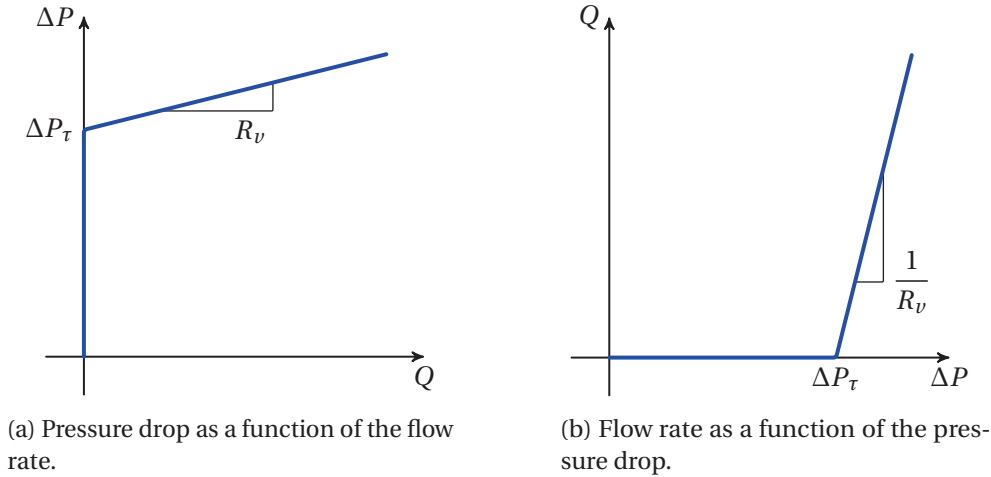


Figure 4.9 – Graphical representation of the annular valve characteristic depending on the independent variable chosen.

In any case, the piecewise linear characteristic which approximates the behaviour of the MR annular valve underlines the presence of a discontinuity. This corresponds to the threshold that the pressure at the valve inlet has to exceed to let the valve open and obtain a flow. Once the set point defined by ΔP_τ is passed, the fluid experiences a resistance to flow defined by R_v . In hydraulics, this behaviour is typical of check valves, the hydraulic equivalent of electric diodes, for which a preloaded spring forces a ball of small mass to close a bore [5].

Consequently, the model of the valve behaviour must describe the switching between two valve states, namely *closed* and *open*, if the overall pressure drop across the valve, $|\Delta P|$, respectively remains below or exceeds the threshold ΔP_τ . In [6] the authors proposed that, if the state transition between one mode to another is fast enough to be considered negligible with respect to the other dynamics present in the system, a piecewise characteristic offers a sufficiently good approximation of the component behaviour. In MR valves, the magnetic field dependent yield stress $\tau_y(H)$ is the analogous of the preloaded spring of hydraulic check valves, and the transition of the fluid from the liquid to the semi-solid state is quick enough to be considered, at least for the sake of a first approximation, negligible with respect to the dynamics of the other phenomena involved. Moreover, the same authors proposed as bond graph representation of fast switching elements, the combination of a linear resistor and a modulated transformer of Boolean modulus controlled by the effort difference across the element [7]. Applying the same approach to the MR valves, we obtain the bond graph depicted in Fig. 4.10.

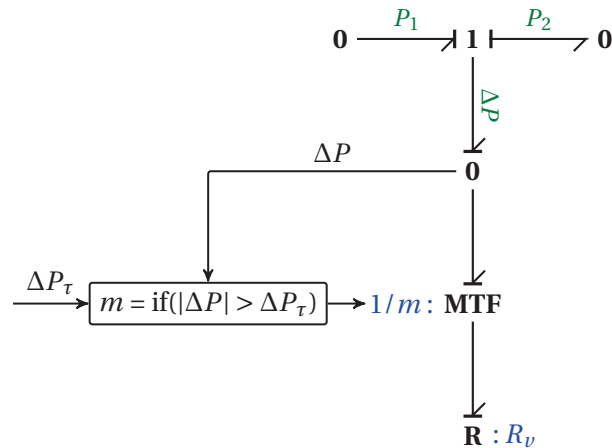


Figure 4.10 – Bond graph model of a fast switching element used to model the annular valve.

The Boolean variable m is the result of the comparison between the overall pressure drop ΔP and the threshold ΔP_τ . If the absolute value of the pressure difference exceeds the set point, m is set to 1. The fluid flows through the valve because a pressure drop is applied across the hydraulic resistance R_v . On the contrary, if the absolute value of ΔP does not go beyond the threshold, m is set to 0, and there is no flow through the valve channel because R_v assumes an infinite value. It must be underlined that the value of ΔP_τ is controlled by the magnetic field and it is determined elsewhere in the valve model. In this respect, the transformer as two sources of modulation.

The $Q - \Delta P$ characteristic and the behaviour of MR valves has been previously introduced by mean of the similarities with the common check valves. More in details, it can be noted that the threshold level depends on counteracting force of a preloaded spring. This is usually set to really small value to easily allow for fluid flow in the chosen direction. That is, the amount of energy which has to be given, i.e. stored, in the biased spring to achieve a deformation sufficient to unlock the valve, has to be as low as possible and, thus, it is often considered negligible with respect to the overall system energy.

MR valves are regulating mechanisms for which the varying threshold level defined by ΔP_τ is obtained imposing a certain magnetic flux density in the channel active regions, which corresponds, as underlined in the previous section, to store a certain magnetic energy in the corresponding permeances. Relying on the strict analogy with the example given for the modelling of the electromagnet discussed in section 4.2, the hypothesis of hydraulic energy storage in MR valve is also done. The consequent main implication is the possibility to transduce signals from the hydraulic to the electric domain. In this respect, whether relevant or not in terms of magnitude with respect to the overall energy involved in the system, estimate the energy required to switch from the *no-flow* to the *flow* conditions acquires a high relevance for sensing purposes. In order to better clarify the hypothesis done and to add further elements to complete the dynamic model of the MR valve under analysis, an illustrative representation

is given in Fig. 4.11.

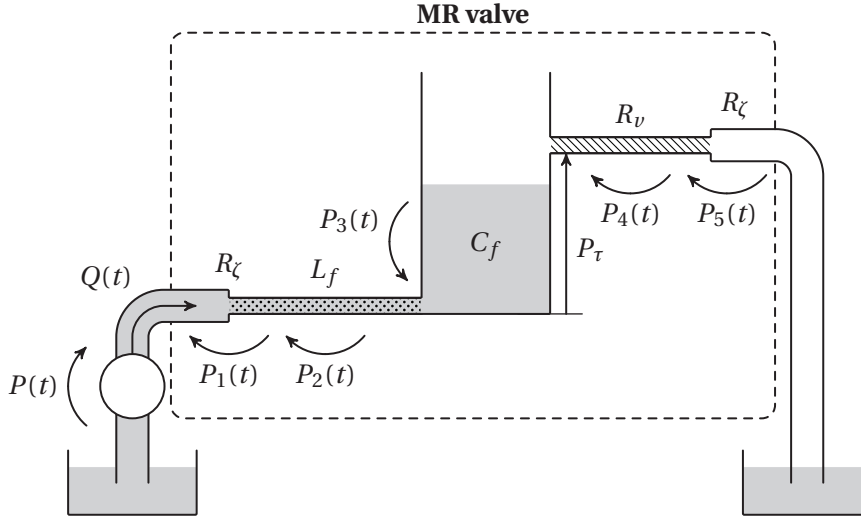


Figure 4.11 – Schematic representation of the equivalent hydraulic circuit used to model the annular valve.

An hydraulic pump is used to impose an input pressure $P(t)$ at the inlet of the valve. The hydraulic resistance R_ζ is used to model the pressure drops related to the valve intake and outtake. In fact, although this components are not part of the valve itself, considering that the valve channel is annular, the fluid has always to undertake a sudden compression to enter the valve duct together with a change in the shape of the streamlines (the lines which connects points in the fluid having the same velocity magnitude and direction), while a sudden expansion occurs at the valve outlet. The fluid inertance L_f associated to the valve channel which, for an annular duct, can be computed as

$$L_f = \int_0^h \frac{\rho}{A(l)} dl = \int_0^h \frac{\rho}{\pi[(r_g + g)^2 - r_g^2]} dl = \frac{\rho h}{\pi[(r_g + g)^2 - r_g^2]} \quad (4.18)$$

where $A(l)$ represents the channel cross-section orthogonal to and function of the path l . As already discussed, the pressure ΔP_τ defines the threshold that has to be exceeded in order to obtain an outflow across the internal and outlet valve resistances. This is represented in Fig. 4.11 assuming that the vertical position of the valve resistance R_v is variable and controlled by ΔP_τ . In any situation, we have that, $P_3(t)$ must be equal to ΔP_τ to obtain a flow through the valve. If this equals zero, the outlet is located at the base of the fluid reservoir. The fluid directly flows through all the valve resistances and the pressure drop across the tank of capacitance C_f is null. On the contrary, for non-zero values of P_τ , the fluid level in the tank has to rise until it reaches the imposed level of the outtake to obtain a flow through the valve. This rise corresponds to the storage of hydraulic energy in the tank C_f . In this example, the potential energy of the fluid mass related to the fluid volume variation in the open reservoir is the counterpart of the potential energy of the spring for a check valve, while it is the analogous of the magnetic energy in the MR valve.

4.3. Bond Graph modelling of MR valves

The storage of hydraulic energy is thus justified assuming a volume variation of the valve channels. Nevertheless, because of the nature of the devices itself, no relative motion among any of the parts composing MR valves actually occurs. The volume variation is seen as an apparent increase of the channel gap due to the deformation of the MR fluid contained in the active regions. The latter, which has undergone the transition to the solid-state because of the exciting magnetic field in the valve channels, is assumed to deform under the action of the external pressure ΔP assuming the shape schematically presented in Fig. 4.12.

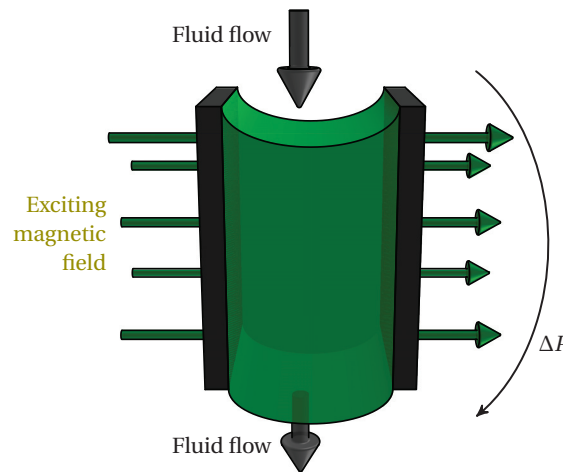


Figure 4.12 – Assumed variation of the channel volume due to the apparent increase of the channel length.

In [8], Ocalan et al. have investigated the micro-structural evolution of the MR particles clusters in micro-channels with geometries and exciting conditions similar to the ones typical of MR valves. One of the main results they reported is that, as clearly depicted in Fig. 4.13, chain-like structures deform under the action of an external pressure and they maintain this deformed shape for steady flow conditions. In particular, Fig. from 4.13a to 4.13e report the clusters structure for steady conditions of both flow rate and exciting magnetic field, and for increasing values of the Mason number. The latter models the fluid particles interactions at the microscopic level and it is defined as the ratio between the hydrodynamic drag force on the particle, f_d , and the inter-particles forces, f_{int} . The drag force of the fluid on a single particle can be determined using the Stokes formula

$$f_d = 6\pi\eta r_p^2 \dot{\gamma} \quad (4.19)$$

where r_p is the particle radius. The inter-particles force in the case of two spherical dipoles in contact is

$$f_{int} = \frac{\pi}{6} \mu_0 r_p^2 M_p^2 \quad (4.20)$$

where M_p is the particle magnetisation. This leads to the following definition of the Mason

number

$$M_n = \frac{f_d}{f_{int}} = \frac{36\eta\dot{\gamma}}{\mu_0 M_p^2}. \quad (4.21)$$

Accordingly to the reference macroscopic quantities used so far to describe MR valves, results depicted in Fig. 4.13 represent micro-channels having the same flow rate $Q = 0.01[\text{cm}^3 \cdot \text{s}^{-1}]$, but growing values of exciting magnetic field, i.e. increasing ΔP_τ .

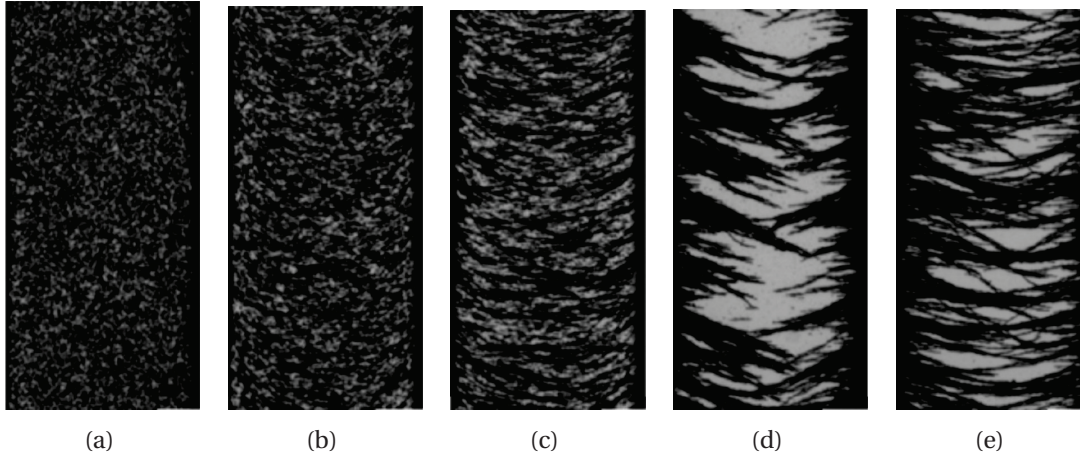


Figure 4.13 – Evolution in aggregate microstructure of MR fluid. Flow positive direction is from top to bottom, while exciting magnetic field horizontal. The Mason numbers in the images are: (a) - ∞ (field-off), (b) - 0.16, (c) - 0.018, (d) - 0.0016, (e) - 0.00014. The channel dimensions are $w = 1.2$ mm and $h = 0.3$ mm [8].

Apart from Fig. 4.13a for which there is no exciting field, the assumed augmentation of the active regions volume because of the apparent increase of the channel gap is verified by the stretching of the particles chains. The parabolic shape proposed in Fig. 4.12 to justify the volume increase and the storage of hydraulic energy can be recognised in all the images from 4.13b to 4.13e, which strengthens the validity of the introduced hypothesis. In reason of the last considerations introduced, the initial bond graph model presented in Fig. 4.10 can now be extend to introduce all the elements associated to the MR valve displayed in the schematic representation given in Fig. 4.11. The complete diagram for the hydraulic part of a generic MR valve is presented in Fig. 4.14

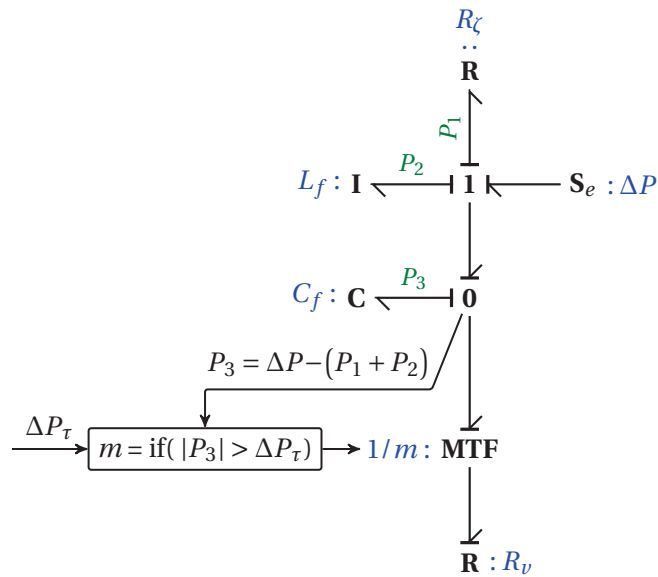


Figure 4.14 – Bond graph model of the hydraulic domain for a general MR valve.

4.3.3 Complete MR valve bond graph model

After having described separately the different valves physical domains, a complete bond graph of the MR valve can now be built merging the ones defined for the electromagnetic and the hydraulic part (Fig. 4.15).

The threshold pressure ΔP_τ required to determine the actual behaviour of the hydraulic part of the valve, because of its dependence with the magnetic field intensity in the valve channels, can be obtained directly from the 0 junction which imposes the same effort Θ_{MR} to its linked components.

As previously introduced, the final structure that the complete bond graph assumes is suggested by the example discussed in section 4.2. In fact, considering the analogies of the MR valve with the electromagnet system, the element linking the electromagnetic and the hydraulic domains is a transducer, identified by the symbol, \mathbb{C} . It simultaneously represents the storage of magnetic energy in the permeance of the valve active regions and the accumulation of hydraulic energy in the valve channels. The most relevant result of all the modelling discussed so far is that the followed approach as allowed to let emerge the sensing possibilities of MR valves, but MR devices in general, while keeping a "high level" perspective of investigation which has avoided to directly refer to the phenomena occurring at microscopic level (the latter have been addressed only in a second phase to justify some of the hypothesis done).

In order to justify all the modelling steps introduced so far, which are mainly derived from systems analogies and a qualitative analysis, the constitutive equation of \mathbb{C} can be derived, as it has been done for the electromagnet. This way, mathematical evidences describing the signal transduction from the hydraulic to the electric domain are provided. Rather than this option, it has been preferred to go beyond this step and directly validate the assumed sensing possibilities experimentally.

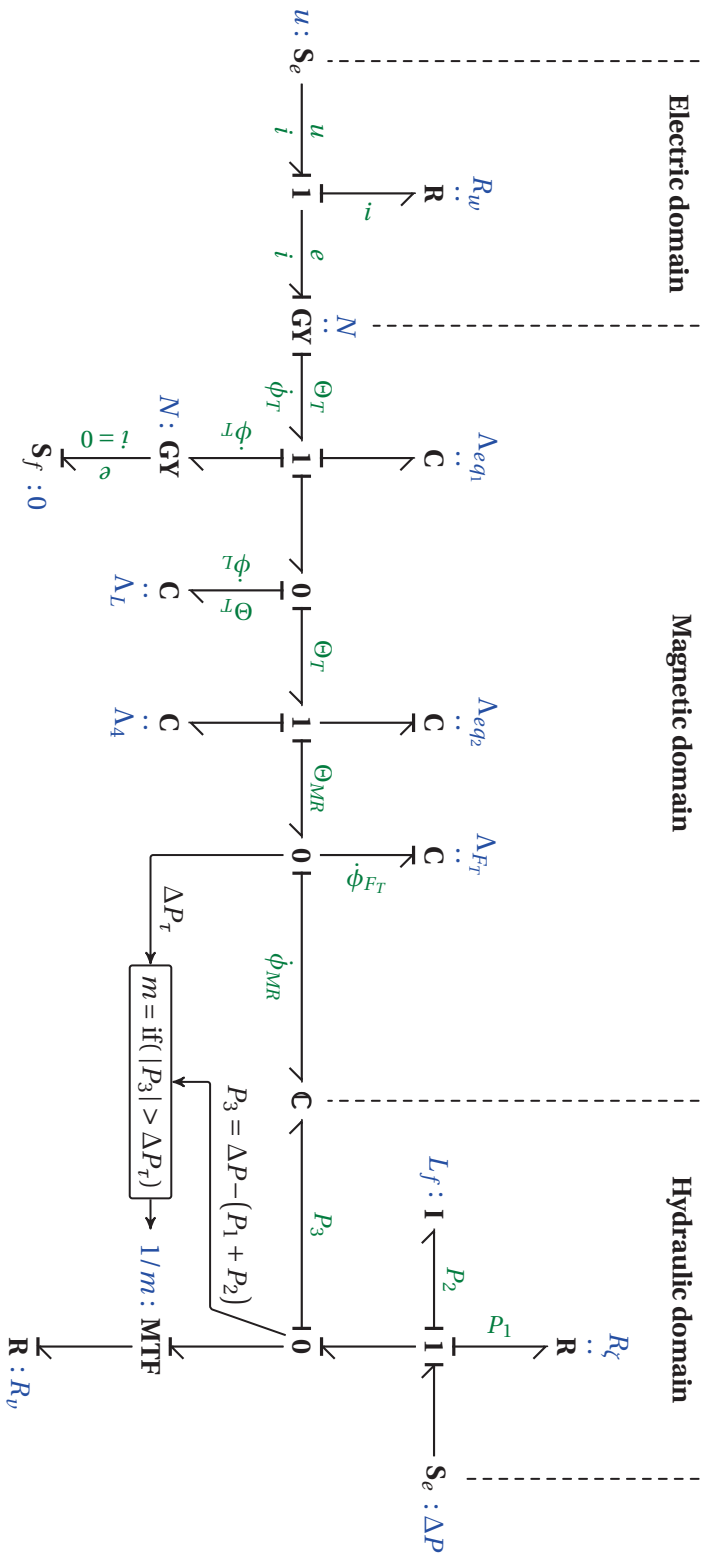


Figure 4.15 – Complete bond graph model of the annular MR valve.

4.4 Sensing Possibilities of MR valves

The transducer \mathbb{C} couples hydraulic and electric variables through the magnetic domain. This underline the possibility of detecting pressure or flow variations by mean of magnetic flux analysis. In order to perform such investigation, a secondary coil, having the same numbers of turn N of the exciting coil, has been wrapped on the central magnetic core. It is represented by the gyrator directed downwards and connected to the source of flow \mathbf{S}_f (Fig. 4.15). As it can be seen, \mathbf{S}_f imposes a flow $f = 0$ to the system and only the effort e on the respective connecting bond can have a non-zero value. This is the common representation of sensors in bond graphs. In fact, an intrinsic feature of a sensor is that it senses a signal without affecting the system. In this respect, if their dynamics can be neglected, they can be represented by an energy sink imposing either zero effort (flow sensor) or zero flow (effort sensor). In the particular case considered, the sensing signal is the induced voltage e .

Mainly because of the geometrical constraints imposed by the valve structure, the sensing coil has been placed on the central magnetic core and it is crossed by the overall magnetic flux circulating in the structure. The induced voltage is proportional to $\dot{\phi}_{MR}$ which represents only a fraction of $\dot{\phi}_T$. Moreover, the expected magnetic flux variation can be alternatively justified by mean of a variation of the reluctance of the active regions \mathcal{R}_{MR} due to the stretching of the particles chains

$$\dot{\phi}_T = \frac{d\mathcal{R}_{MR}}{dt}. \quad (4.22)$$

In any case, the underlying phenomenon is always the same and the last introduced explanation is only a different perspective used to describe it.

4.4.1 Experimental sessions and results

To experimentally validate the concepts introduced so far, test sessions have been performed imposing pressure drop variations across a miniature magneto-rheological valve embedding a sensing coil. In order to enhance the possibility of detection of an induced voltage, the pressure difference and the flow rate are imposed to have high dynamics. This is achieved by mean of an almost square exciting signal which offers high frequency components at the transition fronts between two pressure or flow levels. More in details, the bench test used for the experimental investigation is made of two chambers relied by a duct in which the MR valve is located. While the secondary chamber is an open reservoir, the primary chamber is a closed tank. The fluid can be forced to pass from one chamber to another by mean of a piston which can vary the volume of the first one, as for a syringe. The flow rate is indirectly estimated measuring the linear displacement of the piston, while the pressure drop across the valve is measured by two pressure sensors located respectively at its intake and outtake.

For what concerns the induced voltage measurements, considering that the magnitude of the expected signal is of the order of microvolts, a high accuracy instrumentation amplifier for low signal level amplification is used to increase the induced voltage while reducing the

measurement noise. The amplifier gain is set to $G_a = 1000$.

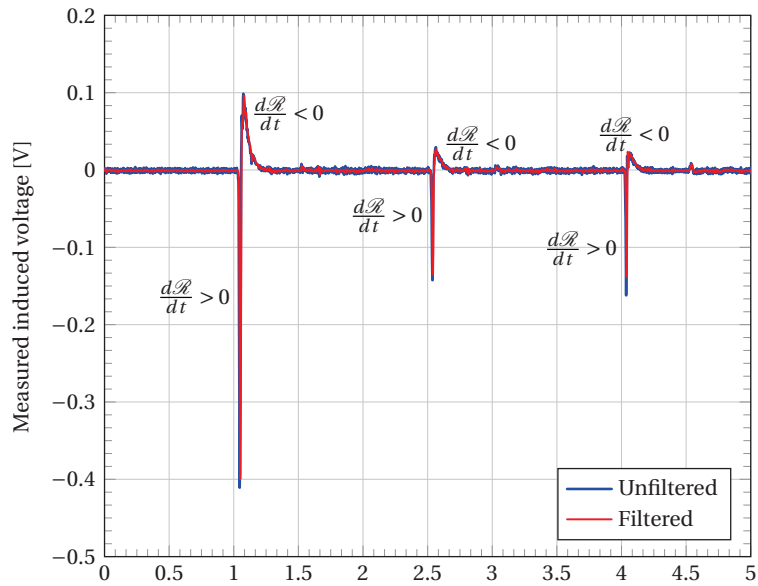
Both the pressure and flow rate variations are measured with a sampling frequency of 1 kHz. Two different experimental sessions are performed. For all the test sessions, the main exciting coil is fed with a constant current of 50 mA. This value corresponds to a relatively low magnetic flux intensity in the valve channel, high enough to obtain the formation of the particles clusters along the magnetic field lines, but at the same time not too strong to let the chain-like structures deforms under the application of moderate pressure. The maximum limit for the imposed pressure drop across the MR valve is fixed to 300 kPa.

Unidirectional flow rate

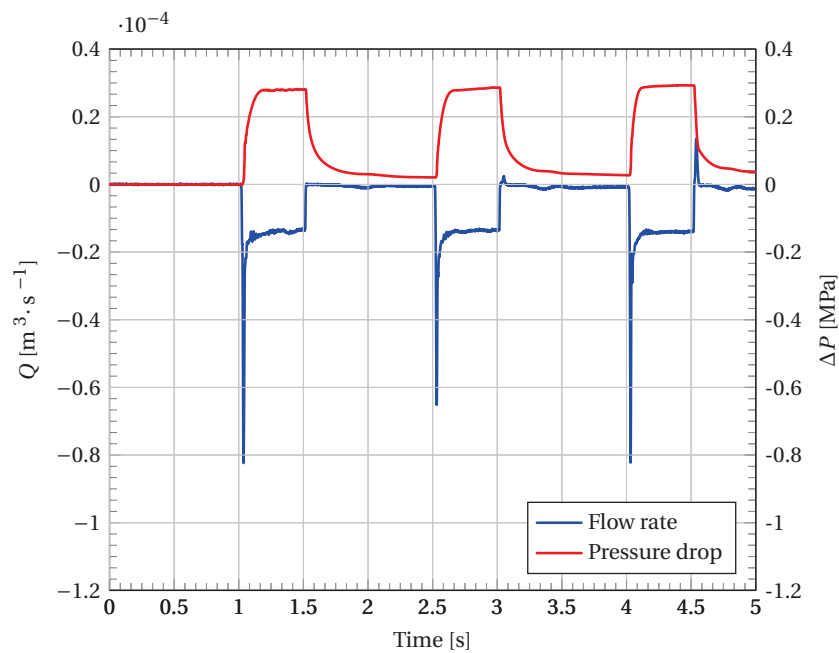
In the first test session, the piston is initially activated to obtain a fluid outflow from the first chamber. After a certain period, the piston position is blocked. This way the flow rate variation is imposed to assume a square profile. In particular, for this test the direction of the piston remains unchanged during the whole session, which implies that the flow rate variations are only related to the magnitude while the direction remains unchanged. Furthermore, the amplified induced voltage provided by the differential amplifier is filter using a fourth order Butterworth low-pass filter with a cut-off frequency $f_{cut} = 150$ Hz. The obtained results are depicted in Fig. 4.16.

Some considerations related to the flow rate signal have to be done for the sake of clarity. The large spikes measured for the flow rate are mainly due to a small quantity of air still remained trapped in the test apparatus. When the piston activates air bubbles can be easily compressed reducing their volume. This results in a quick movement of the piston which gives as an apparent spike in the flow rate.

As soon as a flow rate is imposed through the MR valve, a negative voltage drop is measured across the sensing coil which underlines an increase in the magnetic circuit reluctance associated with the stretching of the particles clusters. Successively, particles chains reposition to achieve steady state and the consequent decrease in the channel reluctance is measured as a positive voltage. As expected, when a constant flow rate is obtained, the magnetic clusters inside the valve channel do not undergo any modifications and no induced voltage is measured. On the contrary, when the piston rod is blocked and the condition of no flow is reached, the variation in the induced voltage is difficultly measurable (only some small oscillations can be observed). A first explanation of this result can be given considering that the variation in the flow rate depicted in Fig. 4.16 is lower than the one previously described. In fact, as introduced before, even if there is no linear movement of the pushing rod, the relaxation of air bubbles in the main chamber induces a bias flow through the MR valve which further smooths the expected transition. This explanation is validated by the pressure signal in the descent front, which underlines that the first chamber slowly discharges through the resistance of the valve channels.



(a)



(b)

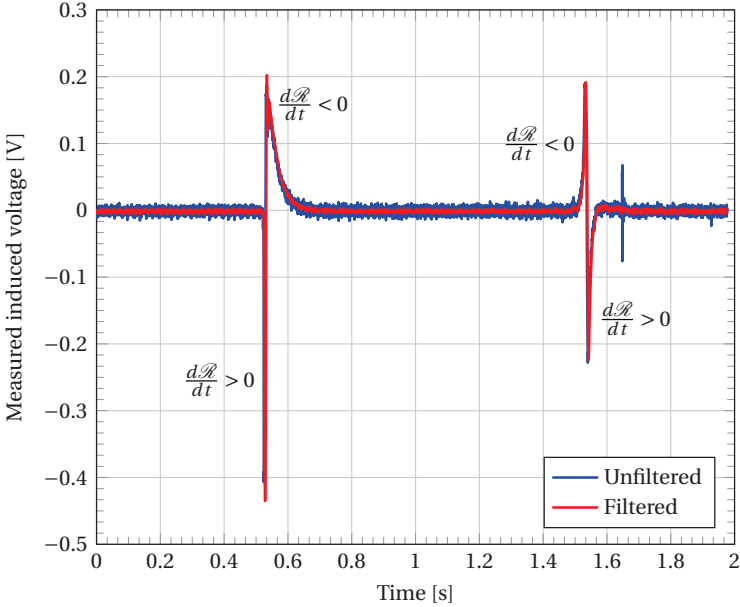
Figure 4.16 – Results from the first experimental session described for unidirectional flow rate. (a) - Measured induced voltage. (b) - Pressure drop and flow rate.

Bidirectional flow rate

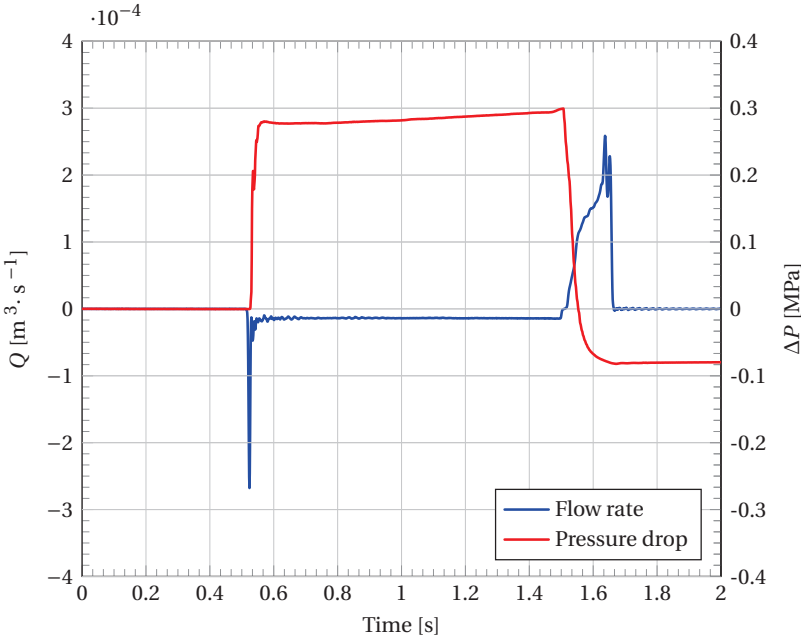
The second test session is intended to define the behaviour of the system if a change in the flow rate direction is imposed. In this respect, the piston is initially pushed towards the MR valve to obtain an outflow from the main chamber and an increase in the pressure. Successively,

Chapter 4. Dynamic Modelling and Sensing Possibilities of MR Valves

the piston is retracted and the MR fluid is forced to change its flow direction and reflow in the main chamber. The results are depicted in Fig. 4.17.



(a)



(b)

Figure 4.17 – Results from the second experimental session described for which bidirectional flow rate is imposed. (a) - Measured induced voltage. (b) - Pressure drop and flow rate.

When the transition from the no flow condition to a constant flow is achieved ($t = 0.5 \text{ s}$), the same behaviour encountered in the previous test session is measured, i.e. particles clusters

firstly stretch and, when steady state flow conditions are achieved, they reorganise with a consequent decrease in the reluctance. On the contrary, the change in the piston movement direction and the consequent abrupt inversion of the MR fluid flow results in a quick variation detected as a relevant induced voltage. The initial voltage increase measured at $t = 1.5$ s can be explained considering that the stretched particles chains reduce their length achieving a minimum in correspondence of the peak in the induced voltage. At this moment the flow rate and the pressure drop across the valve are zero. Successively, as soon as the MR fluid flow increases in the opposite direction, the particles clusters are stretched again and the reluctance increases, which produces a negative variation in the induced voltage.

Unfortunately, although the pressure drop across the valve is measured with a satisfactory accuracy and it represents exactly the evolution of the pressure on both the valve sides, the indirect estimation of Q does not reflect the real flow rate through the valve. More in details, while the biasing phenomena are reduced when the fluid is ejected from the first chamber, when the piston is suddenly retracted the air in the chamber easily expand even if the fluid is probably slowly sucked back. Precise considerations on the flow rate influence are limited by this inconvenient, and most of the conclusions given here are restricted to a qualitative analysis of the actual phenomena observed during the test sessions. In this respect, to improve the performed analysis and to give the due importance to the sensing possibilities of MR valves, an accurate and reliable strategy to measure the actual fluid flow through the valve channels must be done, in spite of the several problems intrinsic to the fluid itself.

4.5 Summary and conclusions

In this chapter the dynamic modelling and the sensing possibilities of MR valves have been discussed. After a preliminary introduction required to define the main features of the used modelling tools, i.e. the bond graph approach, all the different physics domain involved have been analysed and modelled.

More in detail, although the first modelling phase in which the electro-magnetic domain has been addressed, relies on a traditional approach for which any new contents has been introduced, for what concerns the analysis of the remaining physics related to the hydraulic part a new methodic approach has been proposed. This has been possible using the strict analogies that the studied system has with other existing apparatuses. In this regard, MR valves hydraulic part has been initially described as a *fast switching* device, in analogy with electric diodes and check valves. This modelling step has allowed to introduce the conjecture related to the possibility of MR valves to store and simultaneously exchange energy in both the electromagnetic and hydraulic domains, this last feature being an intrinsic property of transducers. In this sense, the bond graph approach has not only allowed to built a model in which all the components belonging to the different physics have been described with the same convention and in which the related power exchanges are clearly represent, but it has demonstrated to be a reliable investigation tool leading to the hypothesis of the sensing possibilities in MR-based devices.

Chapter 4. Dynamic Modelling and Sensing Possibilities of MR Valves

The assumptions given to justify the signal transduction between the hydraulic and electromagnetic domain have been firstly indirectly validated discussing results present in the literature and concerning the micro-structural evolution of MR particles cluster. Successively, direct measurements of the induced voltage across a sensing coil inserted in a miniature MR valve has proven the validity of hypothesis done. In particular, evidences have been provided on the possibility to detect pressure and flow variations in MR valves, but in all kind of MR devices in general, by mean of magnetic flux analysis.

Nevertheless, although the contents provided in this chapter appear to give a great contribution to the actual state of the art of MR-based devices and open new possibilities for what concerns their utilisation as transducer, for example in the perspective of sensor-less control, the correctness of some of the hypothesis done have been justified merely qualitatively. A further effort has still to be done to quantitatively validate some of the conjectures given and the reliability of the introduced concepts must be strengthened by further experimental evidences, this last point representing an interesting and challenging perspective for future researches.

Publications related to this chapter:

- D. Grivon, Y. Civet, Z. Pataky and Y. Perriard, *Detection of Pressure or Flow Rate Variations in MR Valves through Magnetic Flux Analysis*, Electrical Machines and Systems, International Conference on, Accepted for publication, 2016.

Bibliography

- [1] W. Borutzky, *Bond Graph Methodology: Development and Analysis of Multidisciplinary Dynamic System Models*, Springer, 2009.
- [2] D. Karnopp, *Understanding Magnetic and Electrostatic Actuators Using Bond Graphs and a Mechanical Model*, Journal of Franklin Institute, 1984, Elsevier.
- [3] P. E. Wellstead, *Introduction to Physical Modelling*, 1979, Academic Press LTD.
- [4] M. Hecquet, P. Brochet, *Modeling of a claw-pole alternator using permeance network coupled with electric circuits*, Magnetics, IEEE Transactions on, Vol. 31, No. 3, 1995.
- [5] W. Durfee, Z. Sun, J. V. de Ven *Fluid Power System Dynamics*, Center for Compact and Efficient Fluid Power, University of Minnesota, 2015.
- [6] G. Dauphin-Tanguy and C. Rombaut, *Why a unique causality in the elementary commutation cell bond graph model of a power electronics converter*, Systems, Man and Cybernetics, IEEE International Conference on, Vol. 1, pp. 257-263, 1993.
- [7] J. P. Ducreux, G. Dauphin-Tanguy and C. Rombaut, *Bond Graph Modelling of Commutation Phenomena in Power Electronic Circuits*, International Conference on Bond Graph Modelling, ICBGM-93, Proc. of the 1993 Western Simulation Multiconference, pp. 132-136, 1993.
- [8] M. Ocalan and G. H. McKinley, *Rheology and microstructural evolution in pressure-driven flow of a magnetorheological fluid with strong particle-wall interactions*, Journal of Intelligent Materials and Structures, Vol. 23, No. 9, pp. 969-978, 2012.

5 Case Study: Miniature Soft Plantar Pressure Limiter for Smart Footwear

This chapter resumes most of the concepts introduced so far about MR valves through their direct application in the development of an intelligent footwear for foot plantar pressure redistribution in diabetic patients.

A preliminary medical overview concerning diabetes is given in order to introduce the complications that characterise this disease, with a main focus on its connection with lower limb amputation due to peripheral neuropathy and high plantar pressures. The statistical data provided underline the relevance of this global burden and they are used as the main source of motivation for the development of an innovative device able to reduce the issues related to the diabetic foot and the actual recurrence of plantar ulcerations.

After defining the objectives that the future smart footwear must satisfy, the foreseen offloading strategy for its realisation are introduced together with the definition of the main system requirements. In this context, the interesting properties of MR based devices, valves above all, presented in the previous chapters are exploited for the development of miniature soft MR *plantar pressure limiters* to be embedded in the intelligent footwear. Their unique and novel configuration and its advantages with respect to other existing solutions are discussed and, finally, experimental sessions are used to underline the fulfilment of the imposed system requirements as well as the reliability of the developed miniature controllable modules. Last, but not least, the foreseen concept of smart footwear for diabetic patients with foot insensitivity is presented, its completion representing the main future perspective of the work presented in this thesis.

5.1 Introduction: Foot neuropathy in diabetic patients

Despite a big effort and the several sophisticated techniques developed in the last twenty years, diabetes remains one of the first causes of non-traumatic lower limb amputation worldwide. Every year, more than one million of diabetic patients loses a leg because of their own disease which means that every 30 seconds an amputation due to diabetes occurs somewhere in the world [1].

Every year, 90'000 amputations are made in USA and more that 250'000 in Europe [2]. These numbers are even more terrifying considering that the mortality after the surgical procedure may reach the 30% after 30 days and 50% after a year [3].

The majority of amputations (85%) are preceded by a plantar ulceration [4]. In fact, the loss of pain sensation, due to peripheral neuropathy which affects almost 50% of diabetic patients, is a crucial factor in the causal path leading to an ulceration [5]. The absence of an alarm signal causes a bad perception of local micro-traumatic events which, because of their magnitude, but mainly in reasons of their cyclic nature, lead to the development of an ulceration. Moreover, the presence of a peripheral arterial disease, frequently occurring among diabetic people, may contribute to worsen the situation.

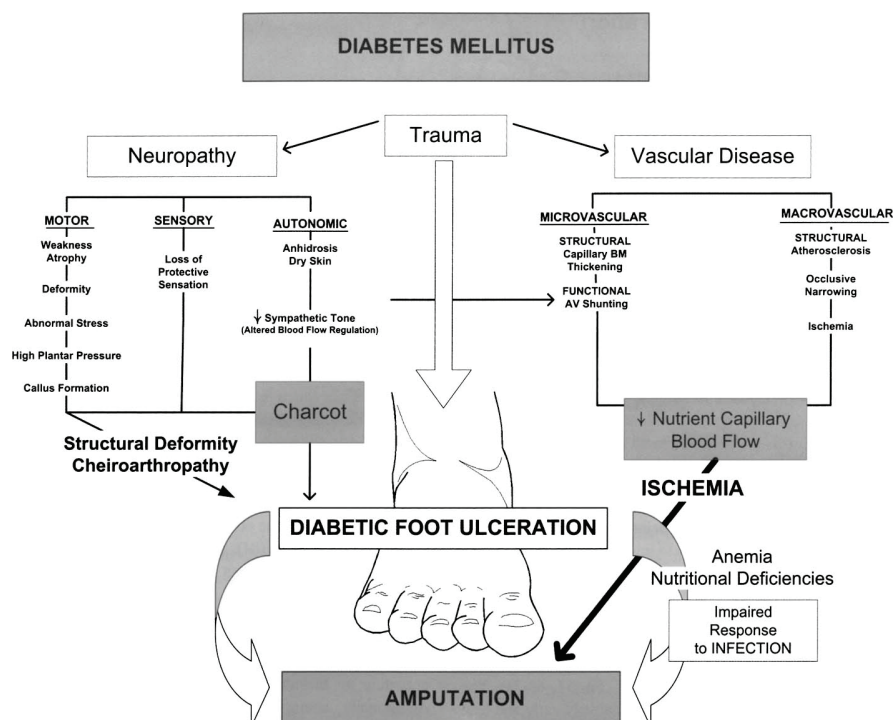


Figure 5.1 – Diabetes mellitus is responsible for a variety of foot pathologies contributing to the complications of ulceration and amputation. Multiple pathologies may be implicated, from vascular disease to neuropathy and mechanical trauma [6].

5.1. Introduction: Foot neuropathy in diabetic patients

Although several different factors may contribute to the development of a plantar ulceration (Fig. 5.1), it has been demonstrated that an increase of the plantar pressure (PP) to values above the common threshold defined for healthy subjects is present in 94% of the plantar ulcerations [7]. Table 5.1 compares the maximum pressures measured in barefoot conditions under different areas for healthy subjects and for diabetic people with a peripheral neuropathy, but free of any foot abnormality.

	Healthy [kPa]	Diabetic with neuropathy [kPa]
Heel	350-400	350-400
Midfoot	150-200	200-250
Forefoot	350-400	700 (up to 1 MPa)

Table 5.1 – Different PPs distribution in diabetic [8] and healthy patients [9]. Pressures refer to the maxima measured in each region in barefoot condition.

The combination of high stresses and loss of the pain sensation lead to a high risk of ulceration and consequent lower limb amputation. In fact, in the presence of an overstressed plantar region and/or a foot trauma, a person without peripheral neuropathy is able to adapt its walking movements to reduce the pain sensation. On the contrary, a diabetic patient affected by peripheral neuropathy is unable to detect any alarm signal even during the formation or in the presence of a wound. Without any changes in the usual walking movement, the repetition of the localised stresses leads to the formation of a chronic plantar ulceration (Fig. 5.2).



Figure 5.2 – Neuropathic ulcer in typical position under second metatarsal head [10].

Offloading the foot plantar is probably the most important element, but, at the same time, the most difficult to obtain for both the treatment and the prevention of foot ulcerations. Many offloading techniques exist and among them total contact cast (TCC) is considered the gold standard (Fig. 5.3a). It allows a decrease of the PP up to 87% [11]. Nevertheless, it must be underlined that only from 2 to 35% of the patients with a prescription of TCCs actually use it [12]. This is mainly related to the impairments and difficulties that it brings to everyday life

Chapter 5. Case Study: Miniature Soft Plantar Pressure Limiter for Smart Footwear

activities.

Removable cast walkers are a less invasive solution (Fig. 5.3b), bringing the same healing rates of TCCs, but with the drawbacks of giving the possibility to be easily removed, which causes a low adherence of the patient which tends to remove it as soon as he can, mainly because of the troubles in everyday activities [13].

Among the others offloading methods, pressure relief shoes like rocker shoes and half shoes (Fig. 5.3c) can be really effective in the cicatrisation process for an ulceration occurring in the forefoot region, but they can lead to the high risk of falling in patients already weakened by the peripheral neuropathy [14].

For what concerns the prevention of plantar wounds, it may be even more difficult. Essentially, this is due to the attitude of the patient with feels less concerned because of the absences of the symptoms, as for any other chronic and silent disease. In this case, orthopaedic shoes and custom made insoles are prescribed (Fig. 5.3d). Nevertheless, the offloading function they implement is passive and, sometimes, it results in a merely displacement of the region with high PP elsewhere in the foot plantar, with the consequent non-solution of the problem.



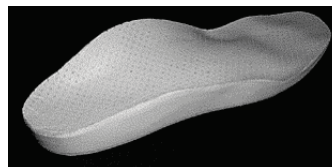
(a) Total contact cast.



(b) Removable cast walker.



(c) Rocker shoes.



(d) Custom made insole.

Figure 5.3 – State of the art offloading techniques for the diabetic foot treatment (images freely available online).

5.2 Intelligent footwear for foot plantar pressure redistribution

Resuming the information given in the introduction, we have that the actual state of the art devices for the diabetic foot treatment allow for good healing percentages of plantar ulcerations. Nevertheless, their main problems and drawbacks remain

- extremely high rates of ulceration recurrence
- low adherence of the patients for the prescribed offloading solutions
- impossibility to adapt to the wound evolution and to the different walking situations encountered.

In order to offer a new solution to these problematics, a concept of smart footwear has been developed. More in detail, the two main functions that it has to implement are:

1. constantly measure the pressure distribution under the whole plantar region with high ulceration risk (i.e. mainly the forefoot and heel areas)
2. automatically offload the regions with high PPs redistributing them over the surrounding regions in order to restore a normal pressure distribution while avoiding the formation of new overstressed areas and, this way, reduce the ulceration risk.

Once defined the objectives that the smart footwear aims to address, the discussion will focus on the foreseen offloading strategy. The latter is intended to obtain a reduction of the PPs of at least 60% while allowing the patient to (almost) naturally wear it during his common day-long walking activities.

5.2.1 Offloading strategy

The proposed offloading strategy relies on the discretisation of the foot plantar in different control areas under which the foot ground contact pressure can be measured and, if required, reduced redistributing it to the surrounding regions (Fig. 5.4).

The chosen offloading strategy, which is relatively simple and similar to the ones employed for the aforementioned passive techniques, is based on the creation of a local depression Δl under the overstressed region to obtain a local relaxation of the plantar tissues and a consequent offloading, while the surrounding regions are used to sustain the foot load (Fig. 5.5).

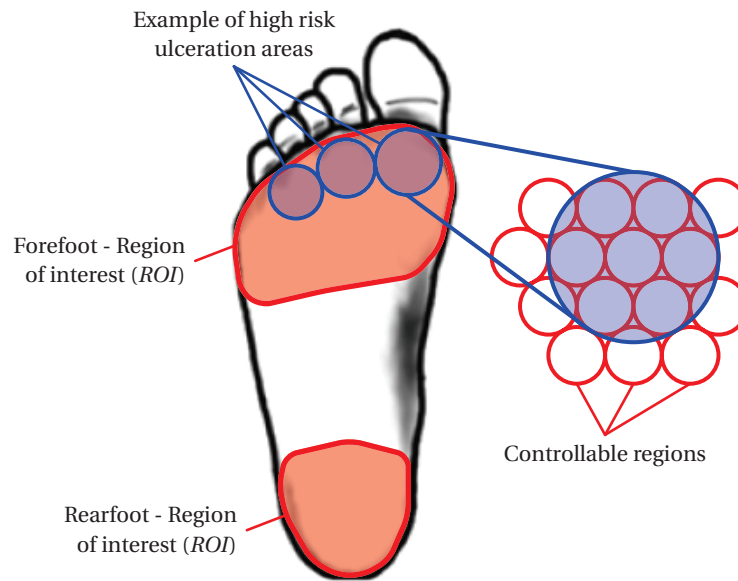


Figure 5.4 – Definition of the Regions of Interest, zone with high ulceration risk and the discretisation of the foot plantar to locate the variable stiffness modules.

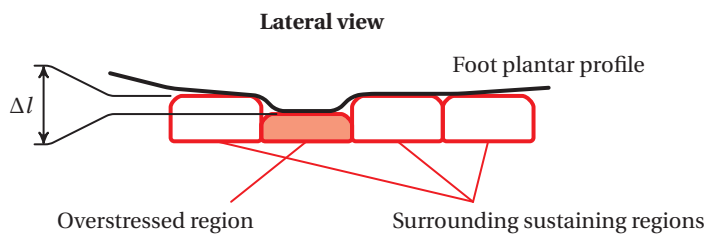


Figure 5.5 – Sagittal view of the sole with a representation of the intended offloading strategy.

Four different pathways, corresponding to four different functions realised by the controllable regions, can be chosen to implement the local offloading of the foot plantar:

1. **variable stiffness:** control of the sole stiffness under the region to be offloaded
2. **variable damping coefficient:** regulation of the damping coefficient of the module located beneath the area to be offloaded
3. **force/pressure limiter:** control of the threshold value for which a sole region is flattened under the effect of the foot axial load
4. **controllable position offset:** definition of the depression depth Δl , corresponding to a module shortening, in order to produce an offset of the force-displacement and force-speed characteristic able to reduce the contact force.

Considering that the aim of the system is to intervene only if a peak of PP is detected rather than precisely control the dynamic response and the pressure evolution during the foot-ground

5.2. Intelligent footwear for foot plantar pressure redistribution

contact period, the two first functions are considered to provide unnecessary control possibilities. Focusing more on the two remaining solutions, it results easier and more straightforward to directly address the value of the force acting over the controllable surface (i.e. the pressure, the primary variable of interest) rather than the entity of the foreseen depression Δl required to shift the load characteristics. Therefore, the final function chosen to be implemented by the controllable modules have to implement is a **plantar pressure limiter**.

5.2.2 System requirements

Vertical deformation

The entity of the minima depression required to achieve a sufficient offloading of the overstressed region can be determined considering the characteristic stress-strain curve of the plantar tissues located under the areas with the highest ulceration risk, i.e. the metatarsal heads. In [15, 16] the authors reported the same properties of plantar tissues located in these regions, having the characteristic non-linear behaviour depicted in Fig. 5.6.

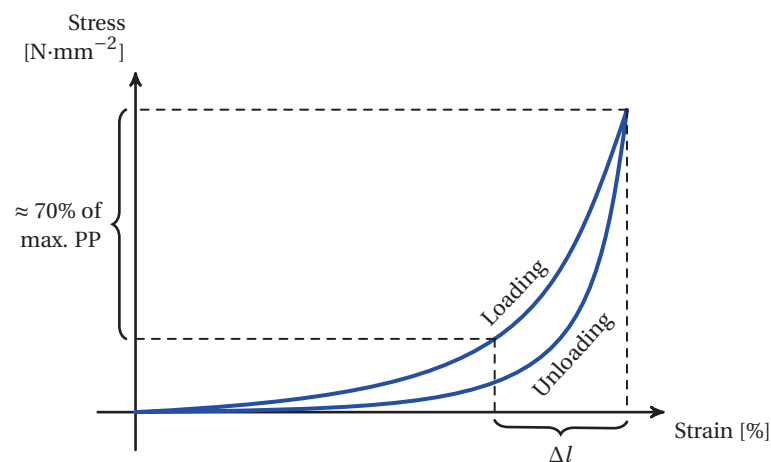


Figure 5.6 – Typical non-linear stress-strain characteristic of the foot plantar tissue under the metatarsal heads. Modified from [15].

Its most relevant feature is related to the sudden increase of the stresses in the last part of the characteristic, which underlines that almost the 70% of the total stress is related to the last 20% of the total strain measured. The magnitude of the depression Δl actually defines the threshold for which the maximum stress is achieved. In this sense, if Δl is 0 (highly stiff region) the blue path in Fig. 5.6 is entirely covered. For the opposite case, if Δl is set to the total maximum strain measured (a sort of hole condition), no stress will appear in the region because there is no actual contact. Extrapolating the results given in both [15, 16], we obtain that a depression of 2.5 to 3 mm guarantees a reduction of the PPs of at least 70%.

Spatial discretization

The size of the controllable regions used to achieve the intended pressure redistribution is a compromise between the complexity of the control system (in terms of both the hardware and the future governing algorithm) and the accuracy in the determination of the magnitude and location of the stress peaks. In this respect, in [17, 18] the authors underlined that, in most of the case, a sensor having a surface of 1 cm^2 is sufficient (accuracy of $\approx 90\%$), to define the position and the proportions of the peaks of pressure. Nevertheless, they also specified that, depending on the shape that the latter assume which, in particular for diabetic patients, can be really sharp, a decrease of the minimal surface is required to avoid the accuracy dropping to values below 60%. Moreover, measuring precision can be further compromised in the case that a peak of stress is located between two sensing regions or, even worse, between three of them.

It must be underlined that, although the straightforward association one actuating region \Leftrightarrow one sensor is the preferred one, an extension of the number of sensing spots per controllable area can be also used to improve the accuracy of the peaks detection.

On the contrary, the reduction of the controllable region cross-section merely enhances the possibility to precisely control the plantar pressure on a particular location, but it does not contribute to define the effectiveness of the offloading. The latter, as discussed in the previous paragraph, is mainly related to the possibility to guarantee a sufficiently high value of Δl . Furthermore, considering that the proposed strategy intrinsically embeds the concept of pressure averaging because of the redistribution strategy, it is not required to resort to cross-sectional areas as small as necessary for sensing purposes. Thus, at least for the sake of a preliminary definition of the system requirements, the reference value for the surface of the variable stiffness regions is fixed to 1.5 cm^2 , being a compromise between sufficient sensing resolution and system complexity.

5.2. Intelligent footwear for foot plantar pressure redistribution

Effective sustaining time and controllable region reactivity

In [19] it has been reported that, in order to define a healthy individual as 'active', the reference value of 10'000 steps per day is set, while evidences underlined that this goal may not be sustainable for older adults or people with chronic diseases, like diabetic patients. This is why this value is used as an upper threshold for the following considerations.

Figure 5.7 represents the different events defining the phases of a complete gait cycle.

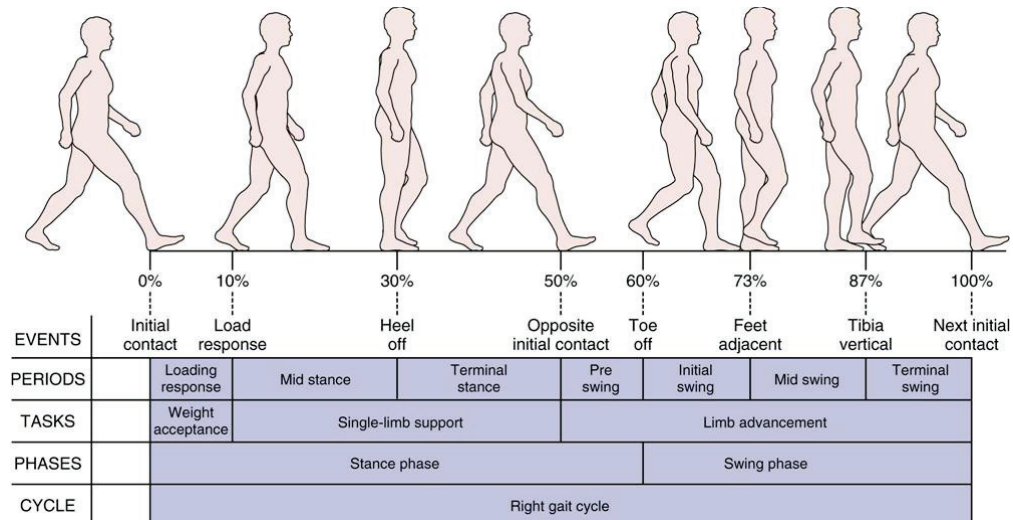


Figure 5.7 – Phases of the gait cycle (modified from [20]).

While a complete gait cycle is defined by the recurrence of two successive initial contacts of the same foot, the concept of step and its duration is mainly related with the stance phase. It accounts for 60% of the total gait cycle and it is defined by the initial contact and the toe off. Moreover, the rearfoot (i.e. the heel) and the forefoot equally share the stance phase, the duration of the heel contact and forefoot contact being the same and corresponding to the 50% of the stance phase. Because of this similarity, even if both the regions are characterised by a high ulceration risk (Fig. 5.4), only the forefoot will be addressed in the following discussion. In [21] an accurate analysis of the gait cycle in diabetic patients underlined that, although the percentage of each phase in healthy and diabetic subject are equal, diabetic patients are characterised by an overall gait cycle 10% longer, which last for 1.1 seconds. In [22] it has been reported that the average contact time in correspondence of the metatarsal heads varies from 250 to 300 milliseconds in diabetic subjects, affected or not by peripheral neuropathy. This leads to the estimation of the total forefoot contact during day-long walking activities, which defines the *effective sustaining time*, of approximately 20 to 25 minutes (standstill is not taken into account).

Furthermore, the same authors provided the evolution of pressure measurements with respect to time which allowed to estimate that the average time required for the areas under the metatarsal heads the interval between the achievement maximum pressure and the no-load condition, occurring when the foot-ground contact finished, is 175 to 200 milliseconds. This

value fixes the maximum time required to obtain the deformation Δl which defines the *controllable region reactivity*.

5.3 Miniature soft MR pressure limiters

Considering the offloading strategy defined in section 5.2.1, the modules embedded in the smart footwear have to implement the function of defining the threshold for which an imposed load is sustained during the foot ground contact and, in the case it is required, regulate their stiffness to achieved two different basic states:

- **locked:** the module achieves a locked state for which it is able to sustain a defined maximum load
- **unlocked:** the defined deformation Δl can be easily obtained under moderate to light loads.

Among the different possibilities to realise a controllable system able to implement the intended function, the ones designed on the basis of the MR phenomenon may be particularly advantageous. In fact, as already introduced in chapter 1, MR-based devices offer as main features high sustainable loads, fast response time, high dynamic range, high controllability, compactness, low complexity and low power requirements.

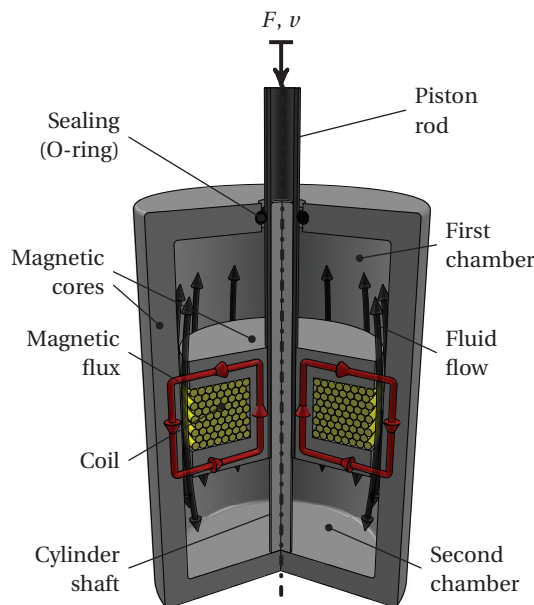


Figure 5.8 – Basic MR damper configuration.

In the most common MR damper configuration (Fig. 5.8), the fluid flow between the first and the second chamber due to the valve vertical displacement is orthogonally crossed by

the valve magnetic flux. The induced change in the fluid viscosity produces a consequent increase in its resistance to flow. Thus, a pressure drop rises between the two chambers and the damper sustainable force increases.

Starting from this common configuration, some attempts towards miniaturisation have been done in [23] to realize a fully portable force feedback glove capable of recreating touch feelings, while in [24] the authors discussed a miniature haptic button designed to convey realistic and vivid sensations to the user in small electronic devices. Nevertheless, although these works present some evidences of the actual possibility to use the MR phenomenon to design small and compact actuators with performances difficultly achievable with other more traditional solutions, the ranges of displacements and external efforts applied on the system are far away from the ones required for the realisation of the intended pressure limiters to be embedded in the smart insole. Furthermore, the presence of part in relative motion between each other still maintain a non negligible level of complexity in the structure and mainly due to the measures and the dedicated structures required to prevent fluid leakages and ensure a correct sealing for all the operating conditions.

As introduced, the miniaturisation process is crucial for the particular application considered and it may be critical if abruptly applied to the common MR damper configurations. The environment in which the offloading system has to operate is particularly harsh. Severe guiding and sealing problems are expected among parts in relative motion if it is considered that the load transmitted by the foot to the module is not purely axial, but it includes a remarkable radial component. In fact, plantar shear stresses during the foot ground contact are not negligible and have been estimated to range from 30 up to more than 80 kPa [25, 27]. In this case, dedicated structures are required to adequately address these issues, but they can result in a not admitted increase of the bulkiness of the overall device. These issues together with the need to provide a smooth interface with the loading body (foot plantar tissues), strengthen the path towards a soft solution in which no parts in relative motion to each other are present.

In this respect, among the several patents based on the principle of regulating the sole stiffness controlling the deformation of a soft cushion filled with some fluid, in [26] the inventor proposes probably the most interesting implementation (Fig. 5.9). More in details, the footwear illustrated in Fig. 5.9 is composed of a multi-bladder system located in the insole. The different bladders, filled with a MR fluid, are connected together by some ducts around which MR valves are located (labeled 117 in the schematics). The pressure distribution at the foot contact is controlled regulating the fluid exchanges between the different soft chambers. This way, the system should be able to change the stiffness of a portion of the footwear sole when a pressure is applied thereto, and returns to equilibrium when the pressure is removed. The most interesting feature of this invention is the intrinsic pressure redistribution implemented by the communication bladders. In fact, as soon as an unbalanced pressure is applied to the different chambers, the fluid is forced to outflow from the cushion subjected to the highest pressure to the surrounding ones and the equilibrium is restored.

Nevertheless, the main limitation of this a configuration (at least for what concerns the

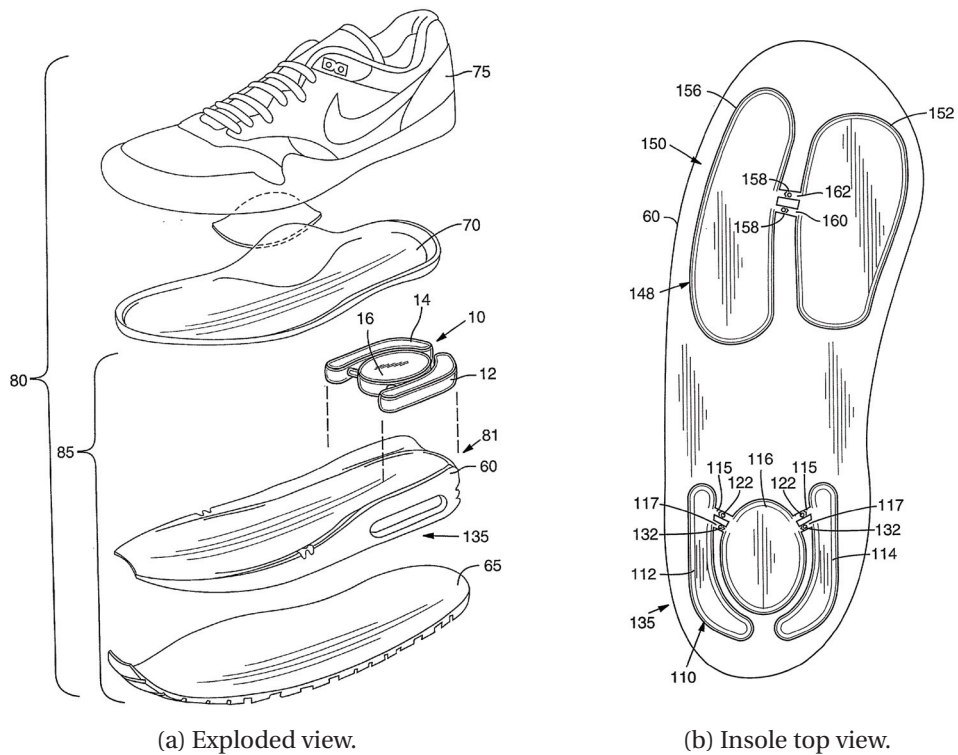


Figure 5.9 – The footwear with a controllable stiffness system made of bladders filled with MR fluid presented in [26].

description given in the patent) is related to the positioning of the regulating parts, i.e. the MR valve, in-between two adjacent bladders. Firstly, this results as rigid spots in the sole which can be perceived as external bodies if they are not covered by a softening layer. Furthermore, the improvement the spatial resolution required to handle peaks of pressure characteristic of diabetic patients can only be achieved increasing the number of bladders. It is evident how the positioning of the valve at their sides will compromise the possibility to achieve a good density of controllable regions under the regions of interest of the foot plantar.

5.3.1 Offloading module configuration

To solve the aforementioned issues a novel soft MR force limiter has been conceived. In particular, similarly to the aforementioned example, no parts in relative motion to each other are present, but all the main constitutive elements are stacked along their symmetry axis (Fig. 5.10). This last feature is probably the most important because it allows to minimise the actual actuator cross-section restricting it to the only foot-module contact surface. This way, a maximisation of the density of the variable stiffness regions under the foot plantar can be achieved.

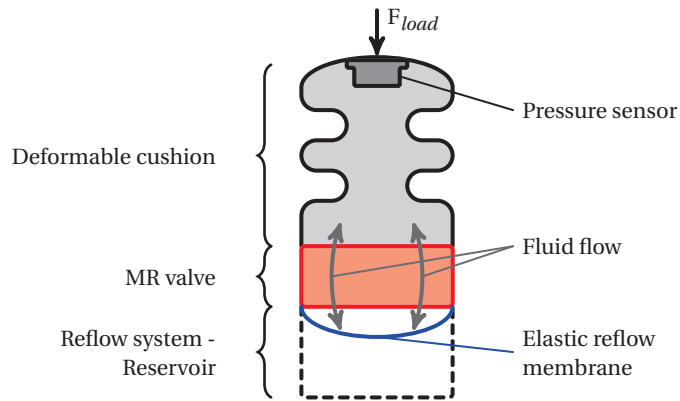


Figure 5.10 – Schematic representation of the configuration proposed to realise the soft MR pressure limiter.

The vertical displacement under an applied load is controlled regulating the MR fluid flow from an external deformable cushion to an expandable reservoir beneath, which is made of an elastic reflow membrane. Once the load is removed, the module initial state is restored thanks to an elastic reflow membrane which brings back up the MR fluid into the deformable cushion. More in detail, the overall module structure can be divided in 3 different main parts:

- deformable cushion
- MR control valve
- reflow system/reservoir.

5.3.2 Deformable cushion

The deformable cushion, which has been manufactured using SLA (stereolithography), is the part directly in contact with the loading body (i.e. the foot plantar). In order to obtain a compliant component easily deformable along its symmetry axis, a bellow structure has been used (Fig. 5.11). It must be underlined that no specific dimensioning of this part has been done and the bellow has been designed following a trial-and-error procedure based on results obtained from the experimental sessions. In order to fulfil the imposed requirements, the cushion structure has been shaped to easily obtain a maximum deformation along the symmetry axis of about 3 to 3.5 mm once the bellow external walls are flattened to touch each other. The material properties of cured SLA resin make it particularly adapted to realise a deformable bellow, considering a tensile strength ranging from 5.95 to 6.95 MPa, a maximum elongation to failure of 90% and a shore A hardness of 80-90 [28].

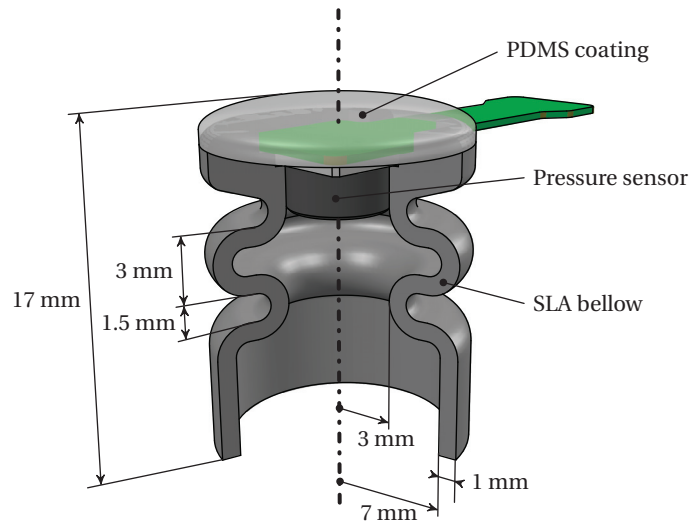


Figure 5.11 – Detailed cross-section and main dimensions of the bellow embedding a miniaturised sensor to measure the fluid pressure inside the deformable cushion.

5.3.3 Elastic reflow membrane

The reflow membrane has been chosen to be made of a latex disc having a diameter of 13 mm and a thickness of 0.2 mm. The most relevant feature, considering the function it has to implement, is the ability to allow deformation up to 200% before failure. Furthermore, in order to prevent the oil composing the MR fluid to affect the latex mechanical properties and reduce the membrane elasticity, a fluoro-silicone coating layer having a thickness of 0.2 mm has been added.

5.3.4 Miniature MR Valves

After having introduced the device configuration and its principle of operation, it is straightforward that the MR valve located in-between the deformable cushion and the expandable reservoir realised using the reflow membrane is the core control element of the system.

Two annular and two radial valves, one for each configuration, have been dimensioned using the design methodology discussed in chapter 3. In order to fulfil the system requirements discussed in section 5.2.2, the quantities listed in Table 5.2 have been chosen as input of the dimensioning routine.

Scenario	ΔP [kPa]	Q	J [$\text{cm}^3 \cdot \text{s}^{-1}$]	B_{MR} [T]
# 1	1000	1	6	0.7
# 2	1500			

Table 5.2 – MR valve requirements for the two design scenarios chosen.

5.3. Miniature soft MR pressure limiters

In particular, the choice to not realise any annular-radial valve has been taken in relation to the realisation drawbacks (in the manufacturing and assembling processes) of this configuration when small dimensions of the constituting parts are required. The obtained geometrical parameters defined in chapter 3 and required for their implementation are listed in Table 5.3.

Scenario # 1						
	h	r_g	g	N. of Turns	R_w [Ω]	
Annular	1	4.4	0.1	67 (68)	0.68 (0.53)	
Scenario # 2						
	h	r_g	g	N. of Turns	R_w [Ω]	
Annular	1.3	4.7	0.1	71 (70)	0.70 (0.56)	
Scenario # 1						
		r_e	r_i			
Radial	1	4.6	3.9	0.08	31 (41)	0.25 (0.20)
Scenario # 2						
		r_e	r_i			
Radial	1.1	5.2	4.2	0.08	34 (39)	0.28 (0.21)

Table 5.3 – MR valves parameters for the two design scenarios (geometrical dimensions are expressed in [mm]). The actual coil number of turns and measured resistances are also reported with respect to reference design values (given in parentheses).

Figures 5.12 and 5.13 report respectively a detailed cross-sectional view showing the different elements composing the MR valves manufactured.

As it can be seen, both the annular and the radial valves realised offer the expected low level of complexity, resulting in simple parts which can be easily manufactured (all the parts are axisymmetric) and simply assembled along their symmetry axis. More in details, no fastening auxiliary part is required, exception given for the upper and lower plastic supports required

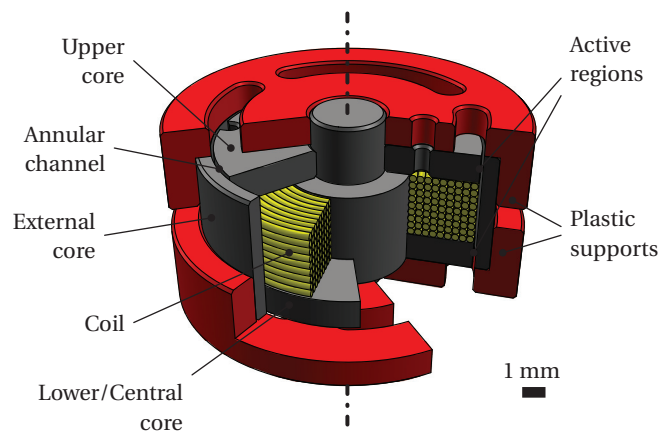


Figure 5.12 – Detailed representation of the miniature annular valve MR.

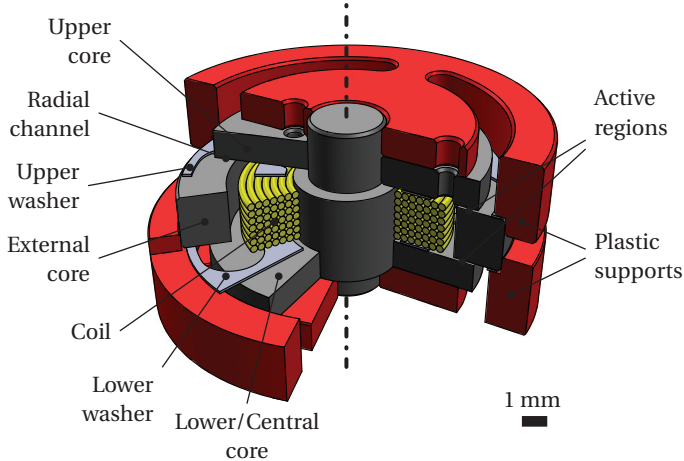


Figure 5.13 – Detailed representation of the miniature radial valve MR.

to fix the relative position of the external cores with respect to the other valve component. All the elements are fastened to the neighbouring ones imposing correctly tolerances of the interpenetrating parts. Moreover, even if not strictly required, two holed washers have been added in the radial configuration to ensure the maintenance of the channel gap. The high level of miniaturisation achieved can be recognised both qualitatively in Fig. 5.12 and 5.13 and quantitatively in Table 5.3.

5.3.5 Complete MR miniature soft pressure limiter

The manufactured parts of the main elements composing the conceived device are displayed in Fig. 5.14.

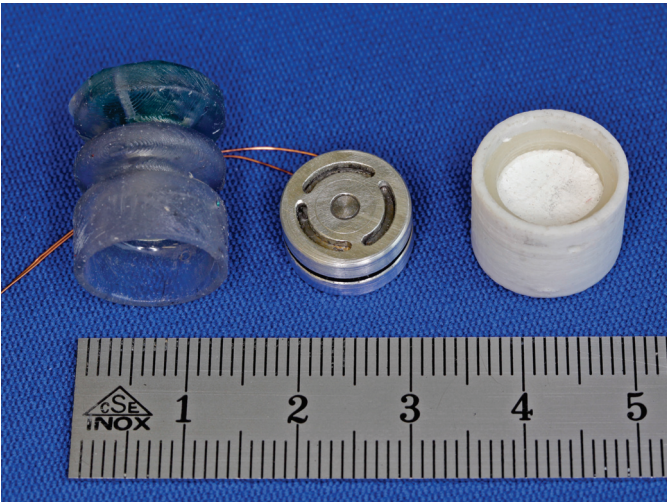


Figure 5.14 – The three main parts composing the plantar pressure limiter: SLA deformable cushion, an annular MR valve and base support with the reflow membrane (from left to right).

A complete and detailed view of the overall soft MR pressure limiter system can now be given (Fig. 5.15).

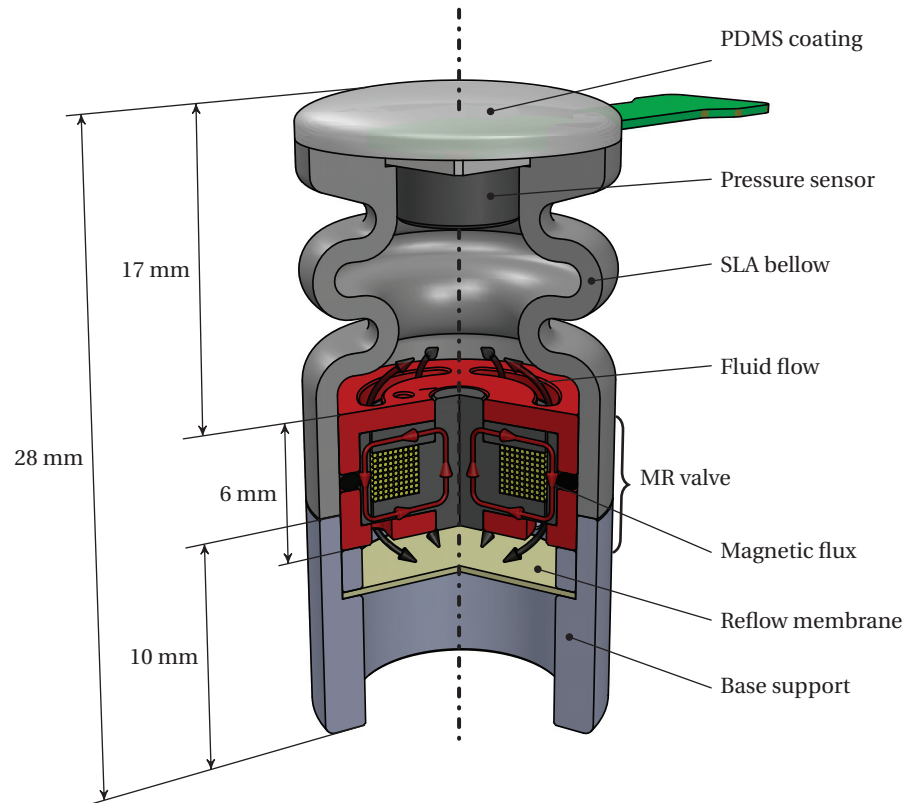


Figure 5.15 – Detailed cross-section of the complete miniature soft MR plantar pressure limiter.

5.4 Experimental sessions and results

In order to characterise both the performances of the different miniature soft MR pressure limiters manufactured, a simple, but effective experimental bench test has been realised. The load is applied using a compressed air piston able to exercise a maximum load of 100 N at a maximum frequency of 10 Hz. The pressure of the MR fluid internal to the deformable cushion is measured using a pressure sensor which allows a maximum sampling frequency of 1 kHz and a maximum resolution of 12 bits. The displacement of the loading piston rod, which corresponds to the vertical deformation of the soft cushion, is measured using an optical laser sensor.

5.4.1 Static measurements

In order to investigate the performances of the three different constituting elements introduced in the previous section, the latter are firstly tested in static condition. This initial test allows to define the relevance of possible non-linearities in their stress to strain characteristic and, in the case of a linear behaviour, the determination of the elastic constant from the measurements (Fig. 5.16).

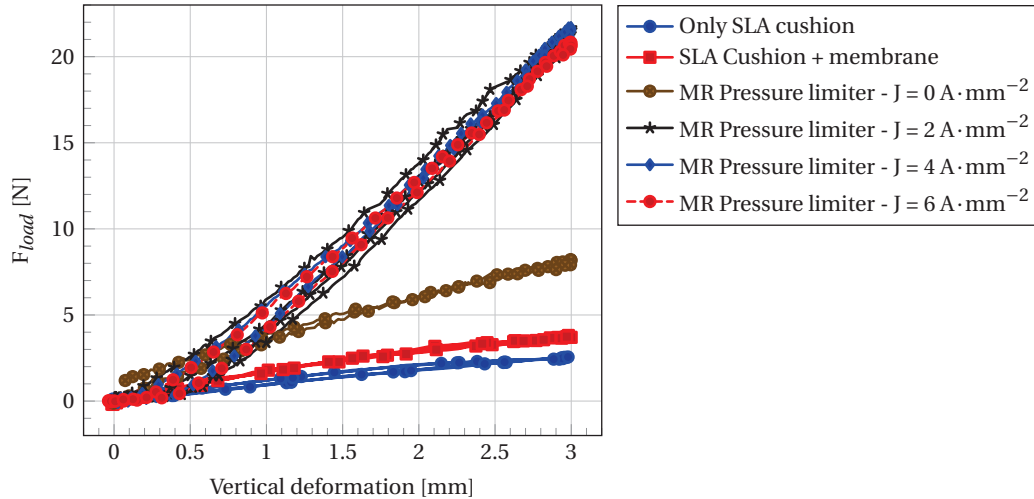


Figure 5.16 – Comparison of the static measurements of the different subsystems under test.

All the subsystems stress to strain characteristics can be well approximated to have a linear behaviour. As expected, the introduction of the latex membrane contributes to increase the rigidity of the system. On the contrary, when the complete system is tested and the MR valve is in the off state ($J = 0 \text{ A} \cdot \text{mm}^{-2}$), the static response should be the same of the SLA cushion + latex membrane. The difference encountered can be explained considering that, due to previous tests, a residual induction B_{MR} in the valve channel may exist because of ferromagnetic core magnetisation, the latter preventing the free flowing of the MR fluid. Thus, higher loads have to be imposed in order to reach a fluid pressure inside the cushion and overcome the residual yield stress of the fluid in the valve duct. Considering the other measurements for which the device is supplied with increasing values of current density, the MR valve appears to be always in the locked state. In this case the cushion compliance alone determine the slopes of the characteristics in Fig. 5.16 which, as expected, are the same. Furthermore, the trends underline that even with relatively small loads (20 N) the achieved vertical deformation is relatively large (3 mm), which underlines the need of SLA cushions with a reduced compliance. A leakage flow of MR fluid still exists even if the valve should avoid any fluid flow, the latter being responsible of the small hysteresis due to the increased slope in the offloading characteristic.

5.4.2 Dynamic measurements

The performed dynamic tests consist in applying a load of 65 N to the module while the latter is supplied with different current densities. In particular, the value of J imposed for each device and thus, valve configurations, ranges from a minimum of 0 to a maximum of $8.1 \text{ A} \cdot \text{mm}^{-2}$, the latter value exceeding the imposed maximum current density defined in the aforementioned design scenario. This choice is used to compensate the fact that, as previously introduced, the number of turns resulting from the MR valve dimensioning is not perfectly matched for all the configurations. Furthermore, such a leeway in the imposable current supply before occurring in saturation of the valve magnetic cores can be used as a mean to verify the correctness of the magnetic modelling used in the MR valve design. If increasing the supply current the device performances in terms of sustainable pressure remain unchanged the saturation value of B_{MR} is reached, meaning that the design features are effectively matched. The following figure reports a schematic representation of the different phases of the performed test session.

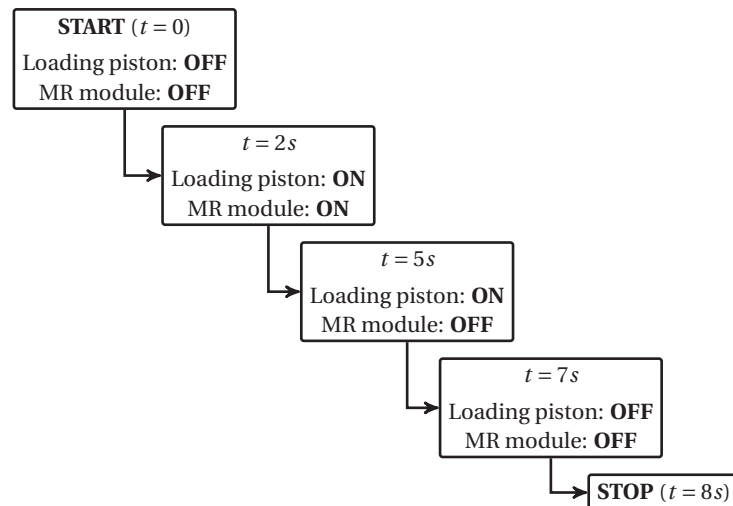


Figure 5.17 – Different events occurring in the performed test session.

After an initial interval of 2 s the piston is activated and the modules are turned on for a total time of 3 s and then are switched off while the load is still maintained. Finally, the load is removed releasing the compressed air in the piston rod. The measured deformation responses for the different measurement sessions are depicted in Fig. 5.18 and 5.19. The ON/OFF state of the modules is represented by the red line in the following graph. Moreover, in order to reduce the large vertical deformation encountered during the static measurements due to the cushion compliance, the bellows has been improved to obtain a structure radially stiffer while remaining easily deformable vertically.

Chapter 5. Case Study: Miniature Soft Plantar Pressure Limiter for Smart Footwear

All the characteristics depict an initial large vertical deformation of the cushion even when the module is in the locked state. This phenomenon can be explained considering that the cushion is made of soft material and that the undergoing deformations are not only vertical, but they can be also radial. Thus, if the volume of fluid in the cushion is maintained constant a radial enlargement will be compensated with a further vertical deformation. Furthermore, some air could remain trapped before the sealing procedure and its compression can enhance this phenomenon. Nevertheless, as previously introduced, the final application in which the tested pressure limiters will be inserted is a therapeutic shoe for plantar pressure redistribution. As a consequence, such behaviour does not represent a drawback, on the contrary it fulfils the system requirements providing a further intrinsically soft interface for the foot contact.

For increasing values of current density the slope of the initial part of the deformation characteristic, which is related to the flow rate through the MR valve, reduces. Thus, the response of the shock absorbers can be actually controlled regulating the supply current. This underlines that, further to the achievement of a desired highly stiff state, the possibility to control the module as a traditional shock absorber providing different damping level exists. Considering this last point, if annular and radial modules are compared, it appears that radial valves offer a better controllability, providing a higher flow rate change (i. e. the differences in slopes in the part of the characteristic are more evident and regularly spaced) for the same supply current change.

All the tested modules succeeded in sustaining the applied load achieving a locked state for which the vertical deformation is maintained almost constant (a residual outflow bias still persists preventing the characteristic to achieve a vertical asymptote when the module is in the

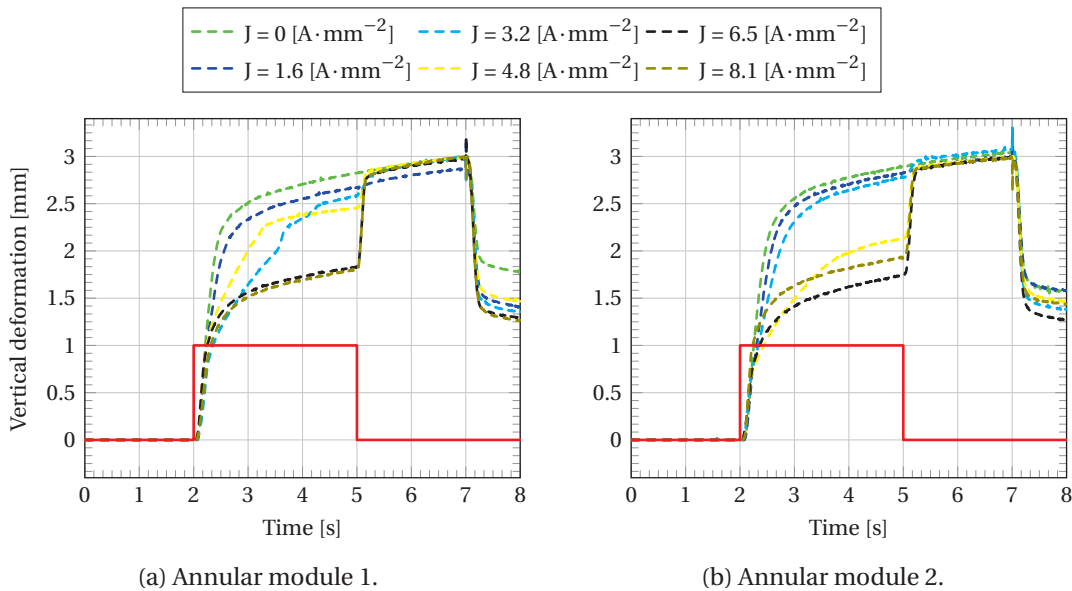


Figure 5.18 – Vertical deformations of the annular modules supplied with different current densities (dashed lines) and valve state with straight Boolean convention (red piecewise line).

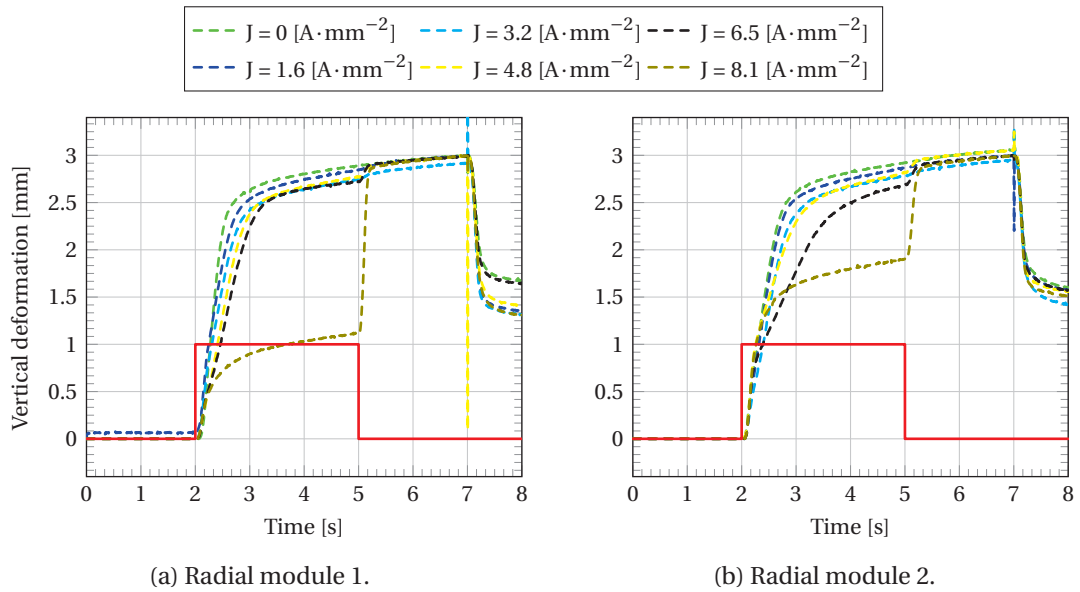


Figure 5.19 – Vertical deformations of the radial modules supplied with different current densities (dashed lines) and valve state with straight Boolean convention (red piecewise line).

locked state, but it can be considered negligible with respect to the overall actuators stroke and the considered time scale). Nevertheless, while absorbers embedding an annular MR valve satisfy this condition for current densities within the limit fixed by the design scenario of Table 5.2 and even an increase of the coil current density up to $J = 8.1 \text{ A} \cdot \text{mm}^{-2}$ does not change the modules response, radial valve based modules require a higher current supply to achieve this state. This phenomenon can be explained considering that the coil number of turns is not matched for radial modules and, consequently, a current density proportionally higher is required to obtain the same magnetic potential defined during the dimensioning phase and achieve the imposed value of magnetic induction over the MR fluid surface. Furthermore, it can be seen that the slope of the characteristics when the module is turned off leaving the locked state to let the soft cushion deform completely is really high and the measured time required to achieve the complete flattening of the module always remains below the 250 milliseconds. In this respect, the system requirements discussed in section 5.2.2 and defined as the controllable region reactivity is fulfilled.

The last parts of the characteristics show the tendency of the modules to restore the initial non-deformed state as soon as compressed air is released from the loading piston, thanks both to the intrinsic cushion stiffness and to the reflow membrane, highlighting the validity of the design solutions employed. Only because of a residual load due to piston internal friction the initial cushion shape is not restored.

Chapter 5. Case Study: Miniature Soft Plantar Pressure Limiter for Smart Footwear

As a final benchmark, Table 5.4 reports the different modules power consumption evaluated as Joule losses in the case of maximum current density required to achieve the *locked state*.

	Annular 1	Annular 2	Radial 1	Radial 2
Joule Losses [mW]	109	112	63	70

Table 5.4 – Power consumption of the different shock absorbers tested.

The main results of Table 5.4 is related to the low power consumption of the pressure limiters embedding radial MR valves, which is 44 - 42% lower than modules based on MR annular valve configuration, which is in accordance with the improved efficiency discussed in 3.5 and which underlines the effectiveness and reliability of this novel design.

5.5 Summary and Conclusion

This chapter has discussed the development and the tests results of some miniature soft MR pressure limiters to be embedded in an intelligent footwear for diabetic patients with foot insensitivity.

After an initial medical introduction to define the problematics related to the diabetic foot as well as the main system requirements to be fulfilled in order to achieve an effective pressure relief and load redistribution under the foot plantar, the discussion focused on the particular configuration chosen to implement the offloading strategy. The latter is based on miniature MR pressure limiters for which the constitutive parts are stacked along the damper symmetry axis. The advantages of the chosen solution, namely reduced complexity, high reliability, easiness of assembling and manufacturing and, last but not least, the possibility to achieve high density of the controllable regions under the foot plantar are comprehensively discussed. Finally, experimental results provide concrete evidence that the manufactured miniature pressure limiters fulfil the imposed system requirements. Moreover, the conceived modules demonstrated extended capabilities beyond their primary function of pressure limiters, as for example the possibility to control the module damping coefficient and, consequently, more precisely influence its dynamic response. In this respect, a further effort has still to be done to better describe these *secondary* behaviours, both from a modelling and from an experimental point of view, for example with the definition of a force-velocity characteristic, as it is typically done for dampers.

Nevertheless, the design methodology used to dimension MR devices simply defines the maximum ratings of the sustainable efforts (i.e. maximum sustainable load for MR dampers, pressure drop for MR valves...) whether neglecting the relevance of their dynamics (respectively the impact velocity of the loading body for shock absorbers and the flow rate for MR valves) which, depending on the specific applications, may assume a fundamental relevance. In this respect, although the foreseen highly stiff state, for which only small deformations occur even under high stresses, is achieved for loads being static or having moderate dynamics, the

more the body-pressure limiter impact velocity increases the more the device sustainable load decreases. This behaviour underlines the importance of considering the power balance among the mechanical power of the external load, the supply electrical power and the properties (mechanical and electromagnetic) of the system components. The path for seeking out the contribution that the different elements provide to the overall system dynamics offers many perspectives for future research activities aiming to model the dampers behaviour as a whole system as well as for the amelioration of the module performances. This process is required to come to a successful completion of the intelligent footwear concept foreseen (Fig. 5.20).

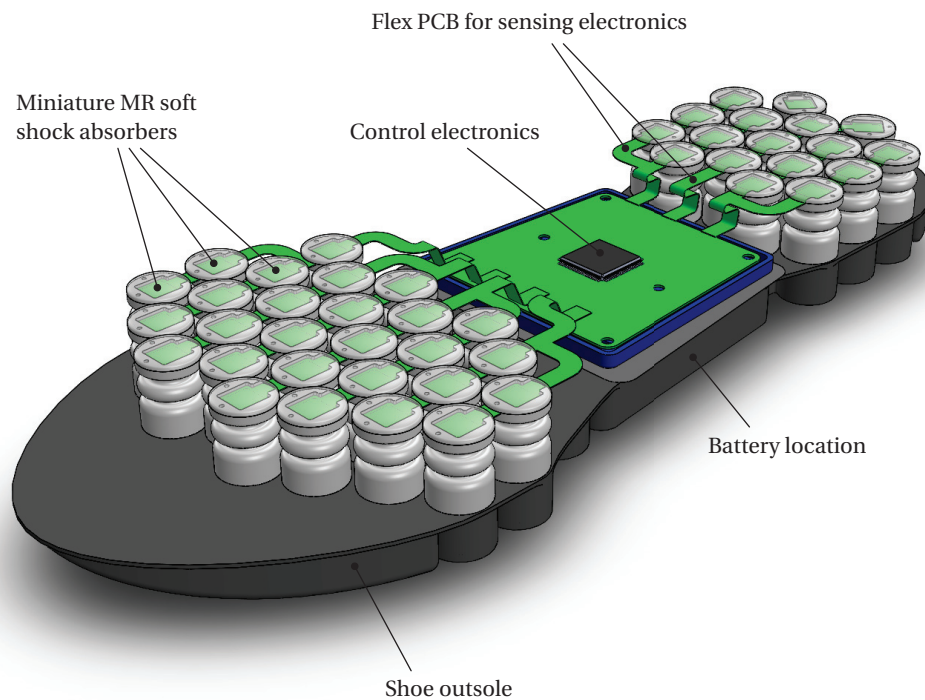


Figure 5.20 – 3D concept of the intelligent footwear for diabetic patients with foot insensitivity embedding the developed miniature MR shock absorbers.

Publications related to this chapter:

- D. Grivon, Y. Civet, Z. Pataky and Y. Perriard, *Design and Characterisation of a Soft Magneto-Rheological Miniature Shock Absorber*, The 10th International Symposium on Linear Drives for Industry Applications (LDIA 2015), Aachen, Germany, July 27 - 29, 2015.

Chapter 5. Case Study: Miniature Soft Plantar Pressure Limiter for Smart Footwear

- D. Grivon, Y. Civet, Z. Pataky and Y. Perriard, *Design and characterisation of a soft magneto-rheological miniature shock absorber for a controllable variable stiffness sole.*, in Archives of Electrical Engineering, vol. 64, num. 4, p. 547 - 558, 2015.
 - D. Grivon, Y. Civet, Z. Pataky and Y. Perriard, *Intelligent footwear for diabetic patients with foot insensitivity*, International Trade Show and World Congress, Leipzig, Germany, 3-6 May, 2016
 - Z. Pataky, D. Grivon, Y. Civet and Y. Perriard, *Chaussures intelligentes pour patients diabétiques*, Revue Médicale Suisse, Vol. Nouveautés en médecine 2015, No. 502, pp. 143-147, 2016.
 - D. Grivon, Y. Civet, Z. Pataky and Y. Perriard, *Experimental Investigation of the Dynamic Performances of a Miniature Soft Magneto-Rheological Shock Absorber*, Advanced Intelligent Mechatronics (AIM), IEEE/ASME International Conference on, Banff, AB, Canada, 2016.
-

Patents related to this chapter:

- Y. Perriard, Z. Pataky, D. Grivon and Y. Civet, *Système de régulation de pression agissant localement sur la peau et le tissu sous-cutané*, Patent No. WO2016075599 (A1), 2015.

Bibliography

- [1] International Diabetes Foundation, *Facts and figures. Did you know*, available online at www.idf.org, 2012.
- [2] Z. T. Bloomgarden, *2000: The diabetic foot*, American Diabetes association, 60th Scientific Sessions, *Diabetes Care*, 24, pp. 946-951, 2001;.
- [3] M. T. Kristensen, G. Holm, K. Kirketerp-Moller, M. Krashennniko, P. Gebuhr, *Very low survival rates after non-traumatic lower limb amputation in a consecutive series: What to do?* *Inter-cardiovascular thoracic surgery*, 14, pp. 543-547, 2012.
- [4] R. E Pecoraro, G. E. Reiber, E. M. Burgess, *Pathways to diabetic limb amputation. Basis for prevention*, *Diabetes Care*, 13, pp. 513-521, 1990.
- [5] S. Tesfaye, D. Selvarajah, *Advances in the epidemiology, pathogenesis and management of diabetic peripheral neuropathy*, *Diabetes/Metabolism Research and Review*, 28, pp. 8-14, 2012.
- [6] R. G. Frykeberg et al., *Diabetic foot disorders: A clinical practice guideline*, Supplement to the *Journal of Foot and Ankle Surgery*, 2006.
- [7] B. E. Sumpio, *Foot ulcers*, *National English Journal of Medicine*, 343, pp. 787-193, 2000.
- [8] W. M. Chen, T. Lee, P. V. S. Lee, J. W. Lee and S. J. Lee, *Effect of internal stress concentration in plantar soft-tissue - A preliminary three dimensional analysis*, *Medical Engineering and Physics*, 32, pp. 324-331, 2008.
- [9] N. Hayafune and H. A. C. Jacob, *Pressure and force distribution under the normal foot during the push-off phase in gait*, *The Foot*, 9, pp. 88-92, 1999.
- [10] W. J. Jeffcoate and K. G. Harding,, *Diabetic foot ulcers*, The Lancet Publishing Group, Vol. 361, pp. 1545-1551, 2003.
- [11] B. J. Beuker, R. W. van Deursen, P. Price, *Plantar pressure in offloading devices used in diabetic ulcer treatment*, *Wound repair and regeneration*, 13, pp. 537-542, 2005.
- [12] C. E. Fife, M. J. Carter, D. Walker, *Why is it so hard to do the right thing in wound care?*, *Wound repair and regeneration*, 18, pp. 154-158, 2010.

Bibliography

- [13] D. G. Armstrong, L. A. Lavery, H. R. Kimbriel, B. P. Nixon, A. J. Boulton, *Activity patterns of patients with diabetic foot ulceration: patients with active ulceration may not adhere to a standard pressure offloading regimen*, Diabetes Care, 26, pp. 2595-7, 2003.
- [14] I. Allet, S. Armand and R. A. de Bie, *Gait alterations of diabetic patients while walking on different surfaces*, Gait and Posture, 29, pp. 488-493, 2009.
- [15] W. R. Ledoux and J. J. Blevins *The compressive material properties of the plantar soft tissue*, Journal of Biomechanics, 40, pp. 2975-2981, 2007.
- [16] P. R. Cavanagh, *Plantar soft tissue thickness during ground contact in walking*, Journal of Biomechanics, 32, pp. 623-628, 1999.
- [17] M. Lord, *Spatial resolution in plantar pressure measurements*, Medical Engineering and Physics, Vol. 19, No. 2, pp. 140-144, 1997.
- [18] T. C. Pataky, *Spatial resolution in plantar pressure measurements revisited*, Journal of Biomechanics, 45, pp. 2116-2124, 2012.
- [19] C. Tudor-Locke and D. R. Bassett Jr, *How many steps/day are enough? Preliminary Pedometer Indices for Public Health*, Sport Medicine, Vol 34, No. 1, pp. 1-8, 2004.
- [20] G. G. Simoneau, *Kinesiology of walking*, in Neumann DA, editor: Kinesiology of the musculoskeletal system: foundations of physical rehabilitation, 2nd edition, St Louis, 2010.
- [21] L. Allet, S. Armand and R. A. de Bie et al., *Gait alteration of diabetic patients while walking on different surfaces*, Gait and Posture, No. 29, pp. 488-493, 2009.
- [22] R. J. Abboud, D. I. Rowley and R. W. Newton, *Lower limb dysfunction may lead to foot ulceration in diabetic patients*, Clinical Biomechanics, No. 15, pp. 37-45, 2000.
- [23] G. Savioz, V. Ruchet and Y. Perriard, *Study of a miniature magneto-rheological fluid actuator for haptic devices*, IEEE/ASME International Conference on Advanced Intelligent Mechatronics (AIM), July, 2010.
- [24] T. H. Yang, J. H. Koo, S. Y. Kim and D. S. Kwon, *A miniature magneto-rheological actuator with impedance sensing mechanism for haptic applications*, Journal of Intelligent Material Systems and Structures, pp. 1-8, 2013.
- [25] M. Yavuz, A. Erdemir, G. Botek, G. B. Hirshmann, L. Bardlsey and B. L. Davis, *Peak Plantar Pressure and Shear Location*, Diabetes Case, Vol. 30, No. 10, pp. 2643-2645, 2007.
- [26] J. F. Switgard, *Article of footwear with a motion control device*, United States Patent Application Publication, Pub. No. US 2002/0053146 A1, May, 2002.
- [27] J. E. Perry, J. O. Hall and B. L. Davis, *Simultaneous measurement of plantar pressure and shear forces in diabetic individuals*, Gait and Posture, pp. 101-107, 2002.
- [28] Formlabs, Available Online at <http://www.formlabs.com/>

6 Conclusions and Perspectives

Overview

This thesis has addressed the design, the modelling and the sensing possibilities of MR-based devices, using as a privileged case of study MR valves.

As it has been underlined in the introductory chapter, although the proposed analyses as well as the formulations derived are referred to MR valves, they can be directly transferred to any MR-based device. This is possible thanks to some crucial common aspects that this family of systems share. First of all, they rely on the same basic principle, i.e. the MR phenomenon. Moreover, all the common configurations of MR dampers, brakes or clutches and valves consists in an axisymmetric structure, which brings a further geometrical affinity. Considering these analogies, a big effort has been done to keep the proposed analysis as broad as possible so that, if required, they can be easily extended to other MR systems.

The design of three different MR valves has been addressed and complete analytical relations have been derived for each of them, giving easy access to the relevance that the different geometrical parameters have on the valve features. The definition of four figures of merit has allowed to focus on the performances that each configuration offers giving the possibility of a direct comparison. Based on the developed analysis, a design routine for the dimensioning of MR valves has been proposed and its reliability, simplicity and cost efficiency have been demonstrated through the comparison with FEA.

Considering that the quality of the approach proposed to design MR valves strongly depends on the accuracy of the magnetic structure modelling used, the development of an enhanced magnetic equivalent circuit, called High-Fidelity Magnetic Equivalent Circuit, has been discussed. Bringing the typical advantages of analytical modelling and developed with the objective of providing a modelling tool applicable to any axisymmetric structure, its reliability has been proved in comparison with FEA results.

The development of miniature MR shock absorbers to be embedded in a smart footwear for

diabetic patients with foot neuropathy has been presented as a particularly challenging case study for the direct application of the presented concepts, the core control element being a miniature MR valve. Advantages of the chosen design configuration have been deeply discussed and the fulfilment of the system requirements have been demonstrated. Moreover, the system limitations as well as some research paths to better understand the system behaviour in the perspective of improving its performances have been discussed.

Within this main research framework, a qualitatively consistent attempt for the dynamic modelling of MR valves has been presented. In this respect, a high level perspective of analysis is proposed by mean of the bong graph modelling approach. The latter has proven its efficacy bringing out the chance of employing MR-based systems as transducer. The assumptions which allowed to set the hypothesis of the sensing possibilities in MR valves have been firstly analysed and justified with state of the art results addressing the micro-structural behaviour of MR fluids. Successively, dedicated test sessions on MR valves have provided experimental evidences to the approach and concepts developed.

6.1 Original Contributions

The core of the presented research work, is related to the three main arguments discussed in the central chapters of this thesis, each of them bringing a novel contribution to the related state of the art.

- *High Fidelity Magnetic Equivalent Circuit:*
this model has been developed to enhance traditional magnetic modelling techniques and offer a simple, reliable, flexible and computationally inexpensive approach to analyse general axisymmetric magnetic structures. The analytical formulation derived from a FE-based semi-empirical modelling to describe arc-shaped permeances has been used to extend common lumped parameter circuits including fringing and leakage fluxes occurring at the transition of magnetic domains with different relative permeability. This situation is intrinsic in MR-based devices, where three materials with different permeability are commonly present and in which fringing fluxes play a fundamental role. The proposed approach has demonstrated high accuracy in the computation of all the main magnetic quantities of relevance and it can be used to deal with every axisymmetric magnetic structure.
- *Design and comparison of different MR valves configurations:*
A complete set of analytical relations has been derived to describe each of the three MR valve configuration under study. A dimensioning routine, which relies on the HFMEC for what concerns the description of the magnetic part, is developed from the given constitutive formulations. The result is a comprehensive methodology for the analysis, the design and the comparison of different MR valves geometries. Moreover, the radial MR valve is a novel configuration among the ones addressed, presented in this work

for the first time. The evaluation of some different figures of merit allow comparing and highlighting the respective features of each geometry, while contributing to provide some guidelines to define the most suitable for some particular application. Last, but not least, both the principles and the main steps of the proposed design methodology have been put in place with a particular effort to allow easy extension to geometries and devices having similar features, with a further contribution of the state of the art design techniques of MR-based devices.

- *Dynamic modelling and sensing possibilities:*

Exploiting the main advantages of bond graph modelling technique (the approach used to describe MR valves, which allows for a high-level perspective and an intuitive description of the multi-physical systems) a novel and qualitatively consistent dynamic model of a MR valve has been proposed. The systematic bond graph construction and the analogies exploited for its completion allowed to bring out the sensing possibilities of MR valves. Experimental evidences have been provided to validate the performed analysis and demonstrate that MR-based devices can be used as transducers.

6.2 Outlook

The research conducted in this thesis can be pursued and completed. In this respect new perspectives of investigation appear.

- *Power analysis generalisation on MR systems*

The design methodology proposed for the dimensioning of MR valves merely addresses static conditions neglecting the relevance of the dynamics involved which, depending on the specific applications, may assume a fundamental relevance. In this respect, experimental observations have underlined that, although the maximum efforts imposed as system requirements are fulfilled for external loads static or having a moderate dynamics, the more the latter increase the more the device sustainable load decreases. This behaviour underlines the importance of considering the power balance among the mechanical power of the external load, the supply electrical power and the properties (mechanical and electromagnetic) of the system components. A further analysis is required to achieve a better comprehension of the whole system behaviour under different conditions and its limitations in order to provide further design elements to improve the proposed methodology.

- *Dynamic modelling and sensing possibilities:*

Although the considerations given along with the approach used to address the dynamic modelling of MR valves and the evidences of the sensing possibilities provided appear to give a great contribution to the actual state of the art of MR-based devices and open new possibilities for what concerns their utilisation as transducer, for example in the perspective of sensor-less control, the correctness of some of the hypothesis

Chapter 6. Conclusions and Perspectives

done have been justified merely qualitatively. In relation with the research perspective introduced in the previous point, a further effort has still to be done to quantitatively validate some of the conjectures given and the reliability of the introduced concepts must be strengthened by further experimental evidences, this last point representing an interesting and challenging perspective for future researches.

- *Smart footwear realisation:*

The contents presented throughout all this thesis as well as the aforementioned research outlooks may be resumed in the common perspective of the final implementation of the intelligent footwear concept. Once this will be available, other research perspective will open, for example for what concerns the implementation of the foreseen offloading strategy through the development of a load transfer algorithm for pressure redistribution.

A Flow of Bingham fluid between two fixed parallel plates

In the following, a comprehensive derivation of the analytical expression describing the flow of Bingham fluid between parallel plates is given. All the geometrical parameters used are referred to Fig. 1.10. Before starting the derivation, the equations of motion for an incompressible newtonian fluid given with respect to the cylindrical coordinates defining a point $P(r, \theta, z)$ represented in Fig. are presented.

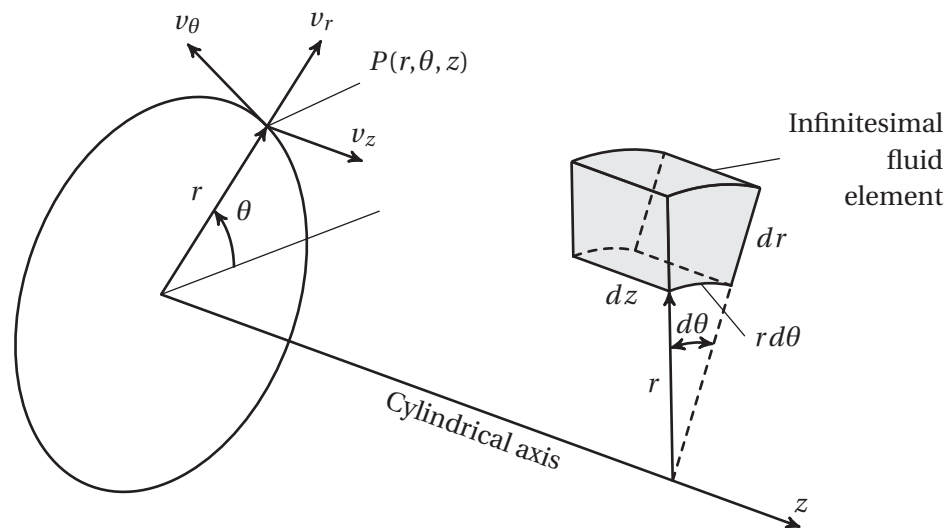


Figure A.1 – Schematic representation of an infinitesimal fluid element defined with respect to a cylindrical coordinate system.

Given the velocity components $\mathbf{u} = (v_r, v_\theta, v_z)$, the continuity equation defines

$$\frac{1}{r} \frac{\partial}{\partial r}(r v_r) + \frac{1}{r} \frac{\partial}{\partial \theta}(v_\theta) + \frac{\partial}{\partial z}(v_z) = 0. \quad (\text{A.1})$$

Appendix A. Flow of Bingham fluid between two fixed parallel plates

The convective time derivative is

$$\mathbf{V} \cdot \nabla = v_r \frac{\partial}{\partial r} + \frac{1}{r} v_\theta \frac{\partial}{\partial \theta} + v_z \frac{\partial}{\partial z} \quad (\text{A.2})$$

while the Laplacian operator is defined as

$$\nabla^2 = \frac{1}{r} \frac{\partial}{\partial r} \left(r \frac{\partial}{\partial r} \right) + \frac{1}{r^2} \frac{\partial^2}{\partial \theta^2} + \frac{\partial^2}{\partial z^2}. \quad (\text{A.3})$$

The r -momentum equation:

$$\rho \frac{\partial v_r}{\partial t} + \rho (\mathbf{V} \cdot \nabla) v_r - \frac{\rho}{r} v_\theta^2 = -\frac{\partial p}{\partial r} + \rho g_r + \eta \left(\nabla^2 v_r - \frac{v_r}{r^2} - \frac{2}{r^2} \frac{\partial v_\theta}{\partial \theta} \right). \quad (\text{A.4})$$

The θ -momentum equation:

$$\rho \frac{\partial v_\theta}{\partial t} + \rho (\mathbf{V} \cdot \nabla) v_\theta + \frac{\rho}{r} v_\theta v_r = -\frac{1}{r} \frac{\partial p}{\partial \theta} + \rho g_\theta + \eta \left(\nabla^2 v_\theta - \frac{v_\theta}{r^2} - \frac{2}{r^2} \frac{\partial v_r}{\partial \theta} \right). \quad (\text{A.5})$$

The z -momentum equation:

$$\rho \frac{\partial v_z}{\partial t} + \rho (\mathbf{V} \cdot \nabla) v_z = -\frac{\partial p}{\partial z} + \rho g_z + \eta \nabla^2 v_z \quad (\text{A.6})$$

where ρ is the fluid density.

For laminar and flow in a circular duct, it can be assumed

- no fluid velocity variation along the circular direction and no twist in the duct
 $\Rightarrow v_\theta = \text{const}$
- flow in the channel completely developed $\Rightarrow \mathbf{u} = u(r)$ only.

Thus, continuity equation A.1 simplifies in

$$\frac{1}{r} \frac{\partial}{\partial r} (r v_r) = 0 \quad \Rightarrow \quad r v_r = \text{const}. \quad (\text{A.7})$$

Considering that there is *no slip* at the walls, $v_r = 0$ everywhere and only the velocity component $v_z = u(r)$ persists.

For steady state flow and neglecting the influence of gravity, the momentum equations along the r and θ directions, respectively defined in (A.4) and (A.5), vanish.

For what concerns the z direction, relation (A.6) becomes

$$\rho (\mathbf{V} \cdot \nabla) v_z = -\frac{\partial p}{\partial z} + \eta \nabla^2 v_z. \quad (\text{A.8})$$

By mean of the definition of the convective time derivative (A.2) and Laplacian operator (A.3) and introducing of shear stress characteristic of newtonian fluid (1.2), we have

$$\frac{\partial p}{\partial z} = \eta \left[\frac{1}{r} \frac{\partial}{\partial r} \left(r \frac{\partial v_z}{\partial r} \right) \right] = \frac{1}{r} \frac{\partial}{\partial r} (r\tau) = \frac{\partial \tau}{\partial r} + \frac{\tau}{r}. \quad (\text{A.9})$$

In case $g \ll r$, the axisymmetric geometry can approximated by two parallel plates (Fig 1.10) and (A.9) can be simplified again. Managing correctly the reference directions so that r becomes y , we have

$$\frac{dp}{dz} = \frac{d\tau}{dy}. \quad (\text{A.10})$$

Assuming a quasi-static situation, the pressure gradient \mathcal{P} is assumed to vary linearly along the channel length l . Thus, it can be defined with respect to the overall pressure drop ΔP as

$$\mathcal{P} \doteq -\frac{dp}{dz} = \frac{\Delta P}{l}. \quad (\text{A.11})$$

The integration of this last relation allows to define the distribution of the shear stress along the y direction of the channel

$$\tau = -\mathcal{P} \cdot y + c. \quad (\text{A.12})$$

The constant c can be determined considering that symmetry and continuity along the y direction of the duct require that there is no shear stress in the middle of the channel and thus

$$c = \frac{\mathcal{P} \cdot g}{2}. \quad (\text{A.13})$$

Following this approach, it is possible to find the values of y for which the shear stress distribution in the channel equals the $|\tau_y|$

$$\begin{cases} h_1 = \frac{g}{2} - \frac{\tau_y}{\mathcal{P}} \\ h_2 = \frac{g}{2} + \frac{\tau_y}{\mathcal{P}}. \end{cases} \quad (\text{A.14})$$

By mean of the analysis introduced, 3 different regions across the channel width can be defined (Fig. 1.10)

- one *pre-yield* region at the center of the channel, where $\tau \leq |\tau_y|$ and fluid velocity remains constant
- two *post-yield* regions near the walls of the channel, where $\tau > |\tau_y|$ and shear rate exists.

In particular the thickness of *pre-yield* region (plug) where the fluid moves at constant velocity

Appendix A. Flow of Bingham fluid between two fixed parallel plates

is

$$h_p = h_2 - h_1 = \frac{2l\tau_y}{\Delta P}. \quad (\text{A.15})$$

Substituting the characteristic equation of Bingham fluid (1.3) in (A.10) and integrating, it is possible to obtain the general expression of the velocity profile. Furthermore, using again the hypothesis of linear variation of the pressure gradient along the channel length, we have

$$u(y) = \frac{1}{\eta} \left(\frac{dp}{dz} \right) y^2 + \mathcal{A}y + \mathcal{B} = \frac{\Delta P}{2\eta l} y^2 + \mathcal{A}y + \mathcal{B}. \quad (\text{A.16})$$

As proposed in [13], the velocity profiles for each region (Fig. 1.10) can be determined considering the following conditions

- **no slip** at walls: $u(0) = u(g) = 0$
- **continuity** of the velocity profile: $u'(h_1) = u'(h_2) = 0$

obtaining

$$\begin{cases} u_1(y) = \frac{\Delta P}{2\eta l} [y^2 - (g - h_p) \cdot y], & \text{for } 0 \leq y < h_1 \\ u_2(y) = -\frac{\Delta P}{8\eta l} (g - h_p)^2, & \text{for } h_1 \leq y \leq h_2 \\ u_3(y) = \frac{\Delta P}{2\eta l} [y^2 - (g + h_p) \cdot y + g \cdot h_p], & \text{for } h_1 < y \leq g. \end{cases} \quad (\text{A.17})$$

The flow rate throughout the channel can be determined simply integrating the velocity profiles described in (A.17)

$$Q = \int_0^{h_1} u_1(y) dy + \int_{h_1}^{h_2} u_2(y) dy + \int_{h_2}^g u_3(y) dy. \quad (\text{A.18})$$

As expected, if the fluid yield stress is 0 (no applied magnetic field) the plug thickness h_p reduces to 0 and the velocity profile across the channel assumes a regular parabolic shape. Thus, Q matches the flow rate usually defined for newtonian fluids

$$Q = \frac{\Delta P g^3 w}{12\eta l} \quad (\text{A.19})$$

and the viscosity dependent pressure drop can be obtained

$$\Delta P_\eta = \frac{12\eta Q l}{g^3 w}. \quad (\text{A.20})$$

The yield stress dependent component ΔP_τ can be determined analysing the relation introduced in (A.15). In fact, it can be noticed that if the h_p is equal to g , the velocity profiles

defined in (A.17) cancel, suggesting that no flow rate exists. Thus, it can be stated that the pressure limit for which this condition is achieved defines the yield stress dependent pressure drop

$$\Delta P_{\tau} = \frac{2\tau_y(H)l}{g}. \quad (\text{A.21})$$

Pressures under this value are sustained by the yield stress induced by the MR phenomenon. Finally, combining the last introduced relations, it is possible to define the overall pressure drop across for the flow of Bingham fluid between parallel plates

$$\Delta P = \Delta P_{\eta} + \Delta P_{\tau} = \frac{12\eta Ql}{g^3 w} + \frac{2\tau_y(H)l}{g}. \quad (\text{A.22})$$

B Complete permeances formulations

B.1 MEC permeances

The complete list of all the permeances for the MECs associated to the three MR valve configurations analysed are presented in Table B.1 at the end of this Appendix.

B.2 Fringing permeances

For the following expressions of the permeances associated to the **radial valve** configuration, refer to schematics depicted in Fig. B.1.

Considering 2.9 we have that

$$L_{F_{1,e}}^* = \frac{r_e}{\cos(\theta_e^*)} \cdot 10^{-2}.$$

Permeances for the first group of fringes, developing externally to the valve, but through the MR fluid, can be defined as

$$\Lambda_{F_1} = \Lambda_{F_{1,R}} + \left(\frac{2}{\Lambda_{F_{1,e}}} + \frac{1}{\Lambda_{F_{1,c}}} \right)^{-1} \quad (\text{B.1})$$

$$\Lambda_{F_{1,R}} = 2\mu_0\mu_{MR} r_e \ln \left(1 + \frac{\pi L_{F_{1,e}}^*}{g_r} \right) \quad (\text{B.2})$$

$$\Lambda_{F_{1,e}} = 4\mu_0\mu_{MR} \left[r_e \ln \left(\frac{h}{L_{F_{1,e}}^*} \right) + (h - L_{F_{1,e}}^*) \cos(\theta_e^*) \right] \quad (\text{B.3})$$

$$\Lambda_{F_{1,c}} = \mu_0\mu_{MR} \frac{\pi[(r_e + h)^2 - r_e^2]}{g_r}. \quad (\text{B.4})$$

Appendix B. Complete permeances formulations

Considering 2.9 we have that

$$L_{F_{2,i}}^* = \frac{r_i}{\cos(\theta_i^*)} \cdot 10^{-2}.$$

Permeances for the second group of fringes, developing externally to the valve, partially through the MR fluid and the valve support

$$\Lambda_{F_2} = \Lambda_{F_{2,R}} + \left(\frac{1}{\Lambda_{F_{2,i}}} + \frac{1}{\Lambda_{F_{2,c}}} \right)^{-1} \quad (\text{B.5})$$

$$\Lambda_{F_{2,i}} = 4\mu_0\mu_{MR} \left\{ r_i \ln \left(\frac{n}{L_{F_{2,i}}^*} \right) + (n - L_{F_{2,i}}^*) \cos(\theta_e^*) \right\} \quad (\text{B.6})$$

$$\Lambda_{F_{2,c}} = \mu_0\mu_{MR} \frac{\pi [r_i^2 - (r_i + n)^2]}{g_r} \quad (\text{B.7})$$

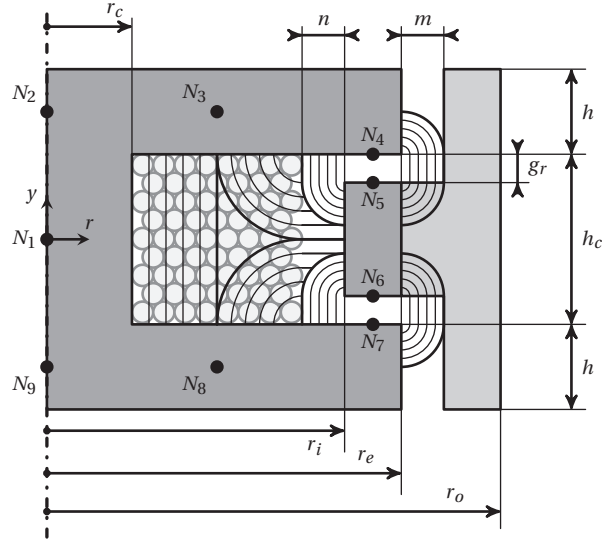
$$\Lambda_{F_{2,R}} = 2\mu_0\mu_{MR} r_i \ln \left(1 + \frac{\pi L_{F_{2,i}}^*}{g_r} \right). \quad (\text{B.8})$$

Permeances for the third group of fringes (internal to the magnetic structure and crossing the valve coil and the MR fluid)

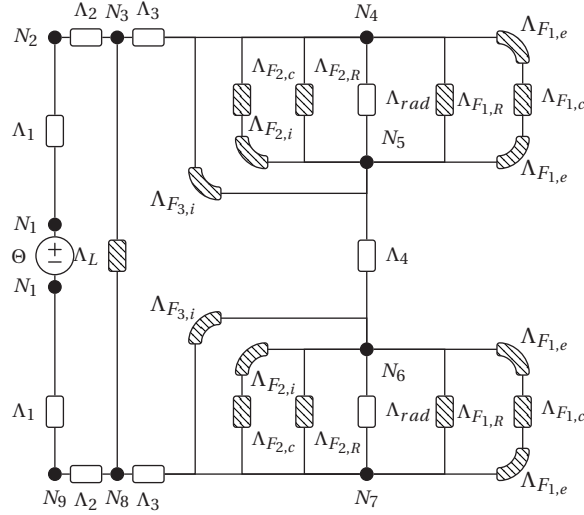
$$\Lambda_{F_3} = \left(\frac{1}{\Lambda_{F_{3,i}}} + \frac{1}{\Lambda_{F_{3,d}}} \right)^{-1} \quad (\text{B.9})$$

$$\Lambda_{F_{3,i}} = 4\mu_0 \left[(r_i - n) \ln \left(\frac{h_c}{2g_r} \right) - \left(\frac{h_c}{2} - g_r \right) \cos(\theta_i^*) \right] \quad (\text{B.10})$$

$$\Lambda_{F_{3,d}} = \mu_0\mu_{MR} \frac{2\pi (h_c/2 - g_r)}{\ln [r_i / (r_i - n)]}. \quad (\text{B.11})$$



(a)



(b)

Figure B.1 – **Radial MR valve configuration:** (a) - Nodes placement for the lumped magnetic model. (b) - Corresponding HFMEC.

For the following expressions of the permeances related to the **annular-radial valve** configuration, refer to schematics depicted in Fig. B.2. Furthermore, the fringes permeances associated with the annular active area of width \$g_a\$ have the same expressions already defined for annular valve. Considering 2.9 we have that

$$L_{F_{2,i}}^* = \frac{r_i}{\cos(\theta_i^*)} \cdot 10^{-2}.$$

The second group of internal fringes associated with the radial active area of width \$g_r\$ can be

Appendix B. Complete permeances formulations

modelled with the permeances

$$\Lambda_{F_2} = \Lambda_{F_{2,R}} + \left(\frac{1}{\Lambda_{F_{2,i}}} + \frac{1}{\Lambda_{F_{2,c}}} \right)^{-1} \quad (\text{B.12})$$

$$\Lambda_{F_{2,R}} = 2\mu_0\mu_{MR} r_i \ln \left(1 + \frac{\pi L_{F_{2,i}}^*}{g_r} \right) \quad (\text{B.13})$$

$$\Lambda_{F_{2,c}} = \mu_0\mu_{MR} \frac{\pi(r_i - L_{F_{2,i}}^*)^2}{g_r}. \quad (\text{B.14})$$

Permeances for the third group of fringes (internal to the magnetic structure and crossing the valve coil and the MR fluid)

$$\Lambda_{F_3} = \left(\frac{1}{\Lambda_{F_{3,i}}} + \frac{1}{\Lambda_{F_{3,c}}} \right)^{-1} \quad (\text{B.15})$$

$$\Lambda_{F_{3,e}} = 4\mu_0 \left[(r_e + g) \ln \left(\frac{h_c}{2g_a} \right) + \left(\frac{h_c}{2} - g_a \right) \cos(\theta_e^*) \right] \quad (\text{B.16})$$

$$\Lambda_{F_{3,c}} = \mu_0\mu_{MR} \frac{\pi[(r_e + h_c)^2 - (r_e + g_a)^2]}{g_r}. \quad (\text{B.17})$$

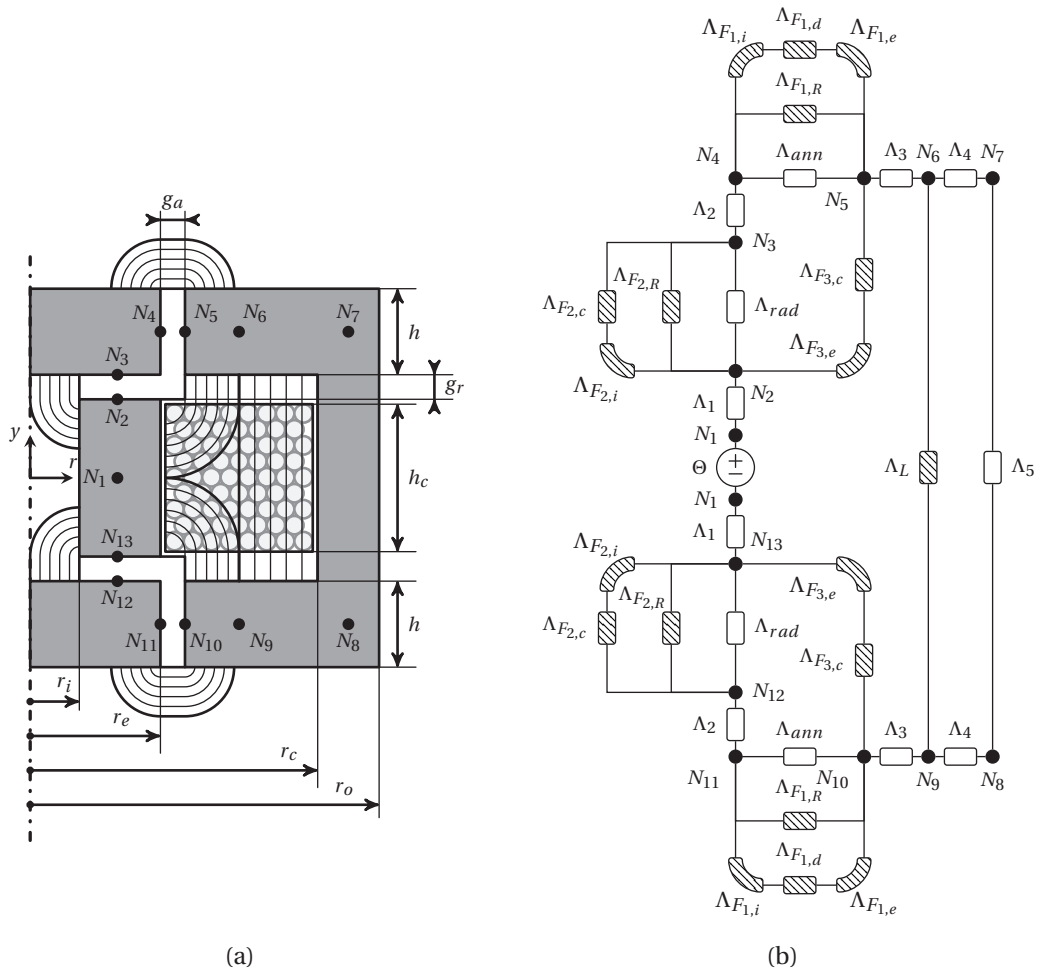


Figure B.2 – Annular-Radial MR valve configuration: (a) - Nodes placement for the lumped magnetic model. (b) - Corresponding HFMEC.

Appendix B. Complete permeances formulations

Λ	Annular	Radial	Annular-Radial
Λ_1	$\frac{2\pi r_c^2}{\mu_0 \mu_{Fe} h + h_c}$	$\frac{2\pi r_c^2}{\mu_0 \mu_{Fe} h + h_c}$	$\frac{2\pi(r_e^2 - r_i^2)}{\mu_0 \mu_{Fe} h_c}$
Λ_2	$\frac{2\pi h}{\ln\left(1 + \frac{w_c}{2r_c}\right)}$	$\frac{2\pi h}{\ln\left(1 + \frac{w_c}{2r_c}\right)}$	$\frac{2\pi(r_e^2 - r_i^2)}{h}$
Λ_3	$\frac{\mu_0 \mu_{Fe}}{2\pi h} \frac{2\pi h}{\ln\left[\frac{r_g}{(r_c + \frac{w_c}{2})}\right]}$	$\frac{\mu_0 \mu_{Fe}}{2\pi h} \frac{2\pi h}{\ln\left[\frac{(r_e + r_e)}{2} / (r_c + \frac{w_c}{2})\right]}$	$\frac{\mu_0 \mu_{Fe}}{2\pi h} \frac{2\pi h}{\ln\left[(r_e - \frac{w_c}{2}) / (r_e + g_a)\right]}$
Λ_4	$\frac{\mu_0 \mu_{Fe}}{h_c + h} \frac{\pi [r_o^2 - (r_g + g_a)^2]}{2}$	$\frac{\mu_0 \mu_{Fe}}{h_c - 2g_r} \frac{\pi (r_e^2 - r_i^2)}{2}$	$\frac{\mu_0 \mu_{Fe}}{2\pi h} \frac{2\pi h}{\ln\left[(r_e + w_c) / (r_e - \frac{w_c}{2})\right]}$
Λ_5	–	–	$\frac{\mu_0 \mu_{Fe}}{2\pi [r_o^2 - (r_e + w_c)^2]} \frac{2\pi [r_o^2 - (r_e + w_c)^2]}{h_c + 2g_r + h}$
Λ_{ann}	$\frac{\mu_0 \mu_{MR}}{\ln\left(1 + \frac{g_a}{r_g}\right)} \frac{2\pi h}{\ln\left(1 + \frac{g_a}{r_g}\right)}$	–	$\frac{\mu_0 \mu_{MR}}{\ln\left(1 + \frac{g_a}{r_e}\right)} \frac{2\pi h}{\ln\left(1 + \frac{g_a}{r_e}\right)}$
Λ_{rad}	–	$\frac{\mu_0 \mu_{MR}}{g_r} \frac{2\pi (r_e^2 - r_i^2)}{g_r}$	$\frac{\mu_0 \mu_{MR}}{g_r} \frac{2\pi (r_e^2 - r_i^2)}{g_r}$

Table B.1 – Permeances for the MECs of the different MR valve configurations studied.

C Bond graph elements: A more complete overview

In this appendix a detailed extension of the concepts given in the introduction of chapter 4 and related to the fundamental bond graph elements is provided. Nevertheless, it must be underlined that the aim of this appendix is not to offer a complete and comprehensive presentation of the bond graph methodology. The objective is rather to provide further tools, mainly by mean of some intuitive examples of the role that the different basic elements may have in different physical domains (with a preference for the electro-magnetic and hydraulic ones), to help the reader understanding the concepts related to bond graph modelling. If further details are needed, the reader may refer to the book by Borutzky "*Bond Graph Methodology: Development and Analysis of Multidisciplinary Dynamic System Models*", from which most of the concepts presented hereafter are taken.

C.1 Power conserving junctions

Nodes are inserted in the bond graph model to split power coming from external sources to the system elements. In particular, these power junctions do not dissipate neither store incoming energy and they satisfy the conservation of power which, in the case of a n -ports junction, establishes

$$e_1 f_1 - e_2 f_2 - \dots - e_n f_n = 0. \quad (\text{C.1})$$

In this respect, two basic types of junctions can be determined in the case that all the node flows rather than the efforts are equal. *Flow junctions* or *0-junctions* are multiports elements for which

$$e_1 = e_2 = \dots = e_n \quad (\text{C.2a})$$

$$f_1 = f_2 + \dots + f_n \quad (\text{C.2b})$$

Appendix C. Bond graph elements: A more complete overview

while the constitutive equations defining *effort junctions* or *1-junctions* are

$$f_1 = f_2 = \dots = f_n \quad (\text{C.3a})$$

$$e_1 = e_2 + \dots + e_n. \quad (\text{C.3b})$$

In particular, if mechanical systems are addressed, 0-junctions define links among the system components while 1-junctions satisfy the d'Alembert's principle. If used to describe electrical circuits, 0-junctions link elements that in reality are connected in series and equation (C.2b) is the well-known Kirchoff's current law, while 1-junctions represent electrical elements in parallel and equation (C.3b) is the Kirchoff's voltage law.

For what concerns causality, if an element imposes an effort to a 0-junction, because of definition (C.2a), the junction will convey the same effort to the other connected elements (Fig. C.1a). Dually, if the flow is settled over a 1-junction by an element, in reason of what defined in (C.3a) the latter will necessarily impose the same flow to the remaining elements (Fig C.1b).

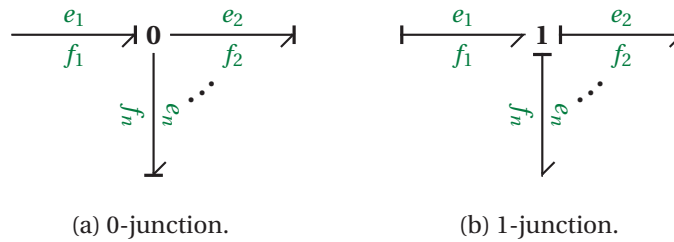


Figure C.1 – Power junctions representation and related causality assignment.

C.2 Energy Storage Elements

Two different types of energy storage elements can be used in bond graphs. These are respectively described as one port elements labelled with the symbols C (capacitor) and I (inertia).

C.2.1 1-port C energy store

These elements are characterised by the definition of a function ϕ_C which defines the component behaviour and which relates the effort applied to the element to its generalised displacement

$$q(t) = \phi_C(e(t)). \quad (\text{C.4})$$

To clarify this concept, let's consider a simple spring. We have that the generalised displacement $q(t)$ at a certain time t , which defines the deformation $x(t)$ imposed to the spring itself, can be easily found integrating the flow variable, i.e. the velocity, with respect to time, as stated by equation (4.2). Moreover, we have that, as defined in (C.4), the effort variable $e(t)$, which

represents the force $F(t)$ acting on the spring, and the generalised displacement $q(t)$ can be directly related as

$$F(t) = k \cdot x(t) \iff e(t) = k \cdot q(t), \quad \phi_C^{-1}(q(t)) = k \cdot q(t) \quad (\text{C.5})$$

where k is the stiffness of the spring. We can now define the amount of energy stored at time t as

$$E(t) = \int_0^t e(\tau) \cdot \underbrace{f(\tau) d\tau}_{dq} = \int_0^q \phi_C^{-1}(\tilde{q}) d\tilde{q} = \frac{1}{2} k x^2(t). \quad (\text{C.6})$$

It may be noted that the last introduced relation underlines that the integral of the flow with respect to time, the conserved quantity q , defines a measure of the storage energy. Thus, it is considered as the element *energy variable*. It describes the entity of the deformation for a linear spring, as in the proposed example, but it can also define the amount of charges stored in a capacitor rather than the volume variation for a hydraulic tank.

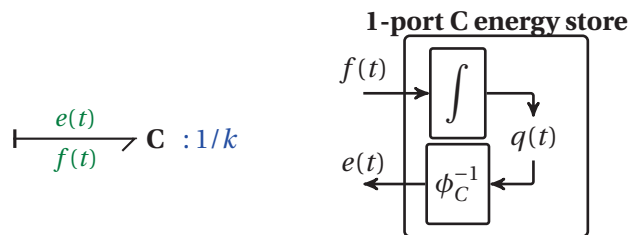
Concerning causality, any of the power conjugate variables (effort or flow) may be the input or the output. Nevertheless, there is a preferred causality. In fact, if equation (C.4) is solved for the effort, $e(t)$ is considered the element output obtained through the integration with respect to time of the input, i.e. the flow variable $f(t)$. The causality is thus defined *integrative* (Fig. C.2a). Dually, if the considered input variable is the flow, the effort must be obtained deriving with respect to time the component constitutive equation, and the causality in this case is *derivative* (Fig C.2b). This may lead to problems if a sudden variation of $f(t)$ occurs at a time t , because its derivation in this case will produce an infinite spike in the effort. On the contrary, this situation never occurs with integrative causality, which is thus the preferred one for 1-port C energy stores. The bond graph representation of C energy store, in the so far considered example of a spring, is depicted in following figure.

C.2.2 1-port I energy store

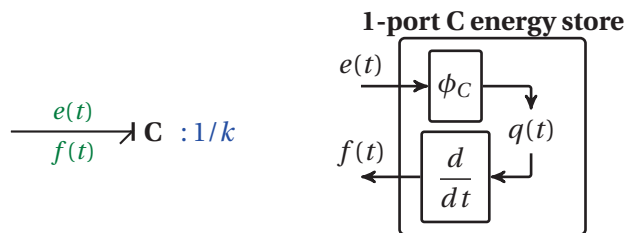
Similarly to what introduced before, a 1-port element is of type I if it can be defined an expression ϕ_I relating the flow variable to the generalised momentum p as follows

$$p(t) = \phi_I(f(t)). \quad (\text{C.7})$$

where I is usually referred as the component inertia. In mechanical systems, such relation represents the storage of energy in a rigid body (translational mechanics) or in a flywheel (rotational mechanics). In hydraulic systems the storage of energy in I elements is due to fluid inertance associated with a pipe, while in electro-magnetic systems, I elements define the storage of magnetic energy in a coil. More in details, for this last case we have that the generalised momentum $p(t)$ at a certain time t , which defines the amount of magnetic flux $\lambda(t)$ linked by the coil itself, can be found integrating the flow variable, i.e. the voltage drop imposed to the coil, with respect to time, as defined in (4.3). Moreover, we have that, as defined



(a) Integrative causality.

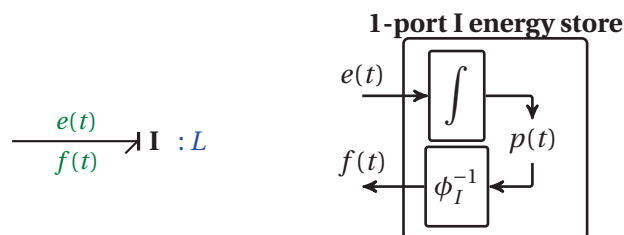


(b) Derivative causality.

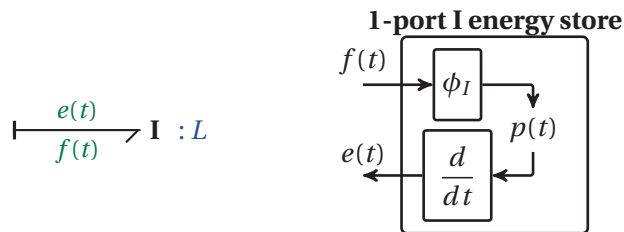
Figure C.2 – Causality assignment for 1-port C elements.

in (C.7), the flow variable $f(t)$, which represents the current $i(t)$ flowing in the coil, and the generalised momentum $\lambda(t)$ can be directly related as

$$\lambda(t) = L \cdot i(t) \iff p(t) = L \cdot f(t), \quad \phi_I(f(t)) = L \cdot f(t) \tag{C.8}$$



(a) Integrative causality.



(b) Derivative causality.

Figure C.3 – Causality assignment for 1-port I elements.

Appendix C. Bond graph elements: A more complete overview

type of source are either effort $E(t)$ for S_e or flow $F(t)$ for S_f , is the following



Figure C.5 – (a) - Effort source. (b) - Flow source.

In the case of an electro-mechanic actuator, if the current supplying the coil is controlled rather than the voltage across it, the correct representation is of a flow source.

C.5 Couplers

Ideal couplers are assumed to convert energy with neither storing nor dissipating it. In this sense, they are elements satisfying the power conservation principle. Although n -ports couplers exist, the following introduction will only address 2-ports elements.

C.5.1 Transformers

The constitutive equations defining a 2-ports *transformer* constraint the efforts and the flows as follows

$$\begin{aligned} e_1(t) &= m \cdot e_2(t) \\ f_2(t) &= m \cdot f_1(t) \end{aligned} \tag{C.11}$$

where m , called modulus, can be a non-negative real constant, a function of another power variable in the system or a function of the time. In bond graphs, this element is denoted with the symbol TF if the modulus is a constant (Fig. C.6a), while in the case of a varying m , TF is prefixed by the letter M and the element is called *modulated transformer* (Fig. C.6b).

Because, as defined by their constitutive relations (C.11), input-output efforts and input-output flows are directly related, if the chosen causality defines the effort on the transformer input port, the transformer itself imposes the effort to the element connected to its output port (Fig. C.6a). The dual analogous is valid for causality imposing flow (Fig. C.6b).

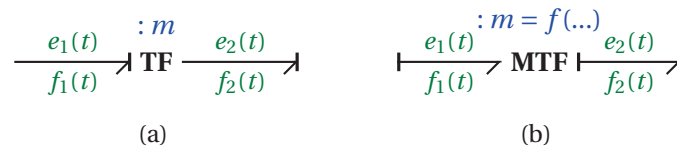


Figure C.6 – (a) - Transformer with imposed effort at the input. (b) - Modulated transformer with imposed flow at the input.

Typical examples of transformers for electrical and mechanical domains are ideal electric transformers and frictionless mechanical gear pairs, the respective moduli being the number

of turns ratio N_2/N_1 between the secondary and primary coils and the ratio r_2/r_1 between the driven and the driving wheels. On the contrary, a crank-rod mechanism, for which rotary motion is converted in a translation, is an example of a modulated transformer, the linear motion being a function of the rotation angle crank.

C.5.2 Gyrotors

Similarly to what introduced before, an element for which a constitutive relation between the input effort and the output flow can be defined as

$$\begin{aligned} e_1(t) &= w \cdot f_2(t) \\ e_2(t) &= w \cdot f_1(t) \end{aligned} \tag{C.12}$$

is called 2-port *gyrator* and w is the gyrator ratio. The bond graph notation for gyrators having a fixed ratio is GY while, in the case that w is a varying quantity, *modulated gyrators* MGY are used.

Because, as defined by their constitutive relations (C.12), the input effort and output flow as well as the input flow and the output effort are directly related, if the chosen causality defines the effort on the transformer input port, the transformer itself imposes the flow to the element connected to its output port (Fig. C.7a). The dual analogous is valid for causality imposing flow (Fig. C.7b).

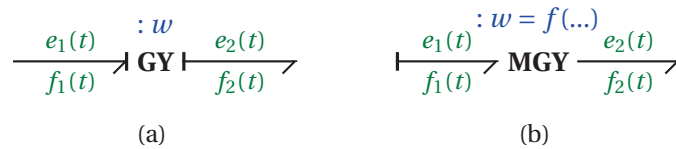


Figure C.7 – (a) - Gyrator with imposed effort at the input. (b) - Modulated gyrator with imposed flow at the input.

Gyrators are used to describe ideal couplers located at the interface between two physical domains that transform energy from one form into another. The energy conversion occurring in a coil can be represented by a gyrator. DC motors, for which the exciting magnetic flux relates proportionally both the torque-current and the voltage-speed, can be described by a modulated gyrator.

Nomenclature

Acronyms

<i>Symbol</i>	<i>Description</i>
FE(A)	Finite Element (Analysis)
HFMEC	High Fidelity Magnetic Equivalent Circuit
MEC	Magnetic Equivalent Circuit
MR	Magneto-Rheological
PDMS	Polydimethylsiloxane
PP	Plantar Pressure
RCW	Total Contact Cast
SLA	Stereolithography
TCC	Removable Cast Walker

List of symbols

<i>Symbol</i>	<i>Unit</i>	<i>Description</i>
α	$\text{N} \cdot \text{A}^{-1} \cdot \text{m}^{-1}$	Slope of the magnetic field dependent yield stress at the origin
B	T	Magnetic flux density
B_{MR}	T	MR fluid saturation induction
B_{iron}	T	Iron saturation induction
c	-	MR fluid coefficient
C_f	$\text{Pa}^{-1} \cdot \text{m}^3$	Hydraulic capacitance
χ	-	Coil filling factor
D	-	Valve dynamic range

Nomenclature

ε	$\text{Pa} \cdot \text{W}^{-1}$	Valve efficiency
E	J	Energy
ε	-	Relative error
η	$\text{Pa} \cdot \text{s}^{-1}$	Viscosity
η_0	$\text{Pa} \cdot \text{s}^{-1}$	Unexcited MR fluid viscosity
F	N	Force
F_η	N	Viscosity dependent damping force
F_τ	N	Yield stress dependent damping force
ϕ	Wb	Magnetic flux
$\dot{\phi}$	Wb	Magnetic flux rate
$\dot{\gamma}$	s^{-1}	Shear rate
H	$\text{A} \cdot \text{m}^{-1}$	Magnetic field
J	$\text{A} \cdot \text{m}^{-2}$	Current density
κ	$\text{Pa} \cdot \text{m}^{-3}$	Pressure to volume ratio
L	H	Inductance
L_i	m	Inner radius (arc-shaped fringes)
L_o	m	Outer radius (arc-shaped fringes)
Λ	H	Magnetic permeance
ω	$\text{rad} \cdot \text{s}^{-1}$	Angular velocity
μ_0	$\text{N} \cdot \text{A}^{-2}$	Vacuum permeability
μ_{MR}	-	MR fluid relative permeability
μ_m	-	Fluid carrier permeability
μ_p	-	Magnetic particles permeability
μ_r	-	Relative permeability
N	-	Coil number of turns
v_p	-	Volume fraction of inclusion
ΔP	Pa	Total pressure drop
ΔP_η	Pa	Viscosity dependent pressure drop
ΔP_τ	Pa	Magnetic field dependent pressure drop
$\Delta P_{\tau_{max}}$	Pa	Maximum magnetic field dependent pressure drop

Nomenclature

\mathcal{P}	$\text{Pa} \cdot \text{m}^{-1}$	Pressure gradient
Q	$\text{m}^3 \cdot \text{s}^{-1}$	Flow rate
\mathcal{R}	$\text{Pa} \cdot \text{s}^{-1}$	Valve reactivity
\mathcal{R}	H^{-1}	Magnetic reluctance
ρ	$\Omega \cdot \text{m}$	Resistivity
ϱ	$\text{kg} \cdot \text{m}^{-3}$	Density
R_w	Ω	Wire resistance
R_v	$\text{Pa} \cdot \text{s} \cdot \text{m}^{-3}$	Hydraulic resistance
R_ζ	$\text{Pa} \cdot \text{s} \cdot \text{m}^{-3}$	Hydraulic resistance due to channel direction variations or sudden expansions/contractions
S_{MR}	m^2	MR fluid active surface
ζ	-	Maximum induction ratio
σ	-	Percentage of the total magnetomotive force acting on the valve channels
t	s	Time
T	$\text{N} \cdot \text{m}$	Torque
T_η	$\text{N} \cdot \text{m}$	Viscosity dependent torque
T_τ	$\text{N} \cdot \text{m}$	Yield stress dependent torque
τ	$\text{N} \cdot \text{m}^{-2}$	Shear stress
τ_y	$\text{N} \cdot \text{m}^{-2}$	Yield stress
ϑ	rad	Deformation angle
Θ	A	Magnetomotive force
θ_e^*	degrees	Optimal angle external fringes
θ_i^*	degrees	Optimal angle internal fringes
\mathbf{u}	$\text{m} \cdot \text{s}^{-1}$	Fluid velocity
v	-	Smoothing coefficient
v	$\text{m} \cdot \text{s}^{-1}$	Linear velocity
V_{tot}	m^3	Valve total volume
x, y, z	$\text{m} \cdot \text{s}^{-1}$	Cartesian coordinates
ξ	-	Ratio between the viscosity dependent pressure drops of the active and non-active channels

Nomenclature

ζ - Hydraulic losses coefficient for channel direction variations or sudden expansions/contractions

Curriculum Vitae

Daniel GRIVON

Born April 10, 1988

Italian Citizen

daniel.grivon@gmail.com

Study and professional experience

- 2013 - 2016 Teaching assistant and PhD student at the Integrated Actuators Laboratory (LAI), École Polytechnique fédérale de Lausanne, Switzerland.
- 2010 - 2012 Master of Science in Mechatronics Engineering, Polytechnic of Turin, Italy.
Master of Science in Automation Engineering, Polytechnic of Milan, Italy.
- 2010 - 2013 Diploma of Alta Scuola Politecnica, Polytechnic of Turin and Polytechnic of Milan educational program for "*young and exceptionally talented students*", Italy.
- 2007 - 2010 Bachelor of Science in Mechatronics Engineering, Polytechnic of Turin, Italy.

Patents

- Y. Perriard, Z. Pataky, D. Grivon and Y. Civet, *Système de régulation de pression agissant localement sur la peau et le tissu sous-cutané*, Patent No. WO2016075599 (A1), filed November, 2014.
- E. Zezzetti, S. Moos, D. Grivon, K. L. Bräul, E. B. Fuentes and V. Marino, *Dispositivo e sistema di scansione tridimensionale, e relativo metodo*, Patent No. TO2013A000202, filed March, 2013.

Journal Articles

- D. Grivon, Y. Civet, Z. Pataky and Y. Perriard, *High-Fidelity Magnetic Equivalent Circuit Modelling of Axisymmetric Magneto-Rheological Devices*, Magnetics, IEEE Transactions on, Accepted for Publication.

Curriculum Vitae

- D. Grivon, Y. Civet, Z. Pataky and Y. Perriard, *Design and characterisation of a soft magneto-rheological miniature shock absorber for a controllable variable stiffness sole*, in Archives of Electrical Engineering, Vol. 64, No. 4, pp. 547-558, 2015.
- D. Grivon, E. Vezzetti and M. G. Violante, *Study and development of a low cost "OptInertial" 3D scanner*, Precision Engineering, Vol. 38, Issue 2, pp. 261-269, 2014.
- D. Grivon, E. Vezzetti and M. G. Violante, *Development of an innovative low-cost MARG sensors alignment and distortion compensation methodology for 3D scanning applications*, Robotics and Autonomous Systems, Vol. 61, Issue 12, pp. 1710-1716, 2013.

Conference Publications

- D. Grivon, Y. Civet, Z. Pataky and Y. Perriard, *Detection of Pressure or Flow Rate Variations in MR Valves through Magnetic Flux Analysis*, Electrical Machines and Systems, International Conference on, Accepted for publication, 2016.
- D. Grivon, Y. Civet, Z. Pataky and Y. Perriard, *Experimental Investigation of the Dynamic Performances of a Miniature Soft Magneto-Rheological Shock Absorber*, Advanced Intelligent Mechatronics (AIM), IEEE/ASME International Conference on, Banff, Canada, 2016.
- D. Grivon, Y. Civet, Z. Pataky and Y. Perriard, *Intelligent footwear for diabetic patients with foot insensitivity*, International Trade Show and World Congress, Leipzig, Germany, 2016
- D. Grivon, Y. Civet, Z. Pataky and Y. Perriard, *Design and Characterisation of a Soft Magneto-Rheological Miniature Shock Absorber*, The 10th International Symposium on Linear Drives for Industry Applications (LDIA 2015), Aachen, Germany, 2015.
- D. Grivon, J. Chavanne and Y. Perriard, *Comparison of two different Eddy currents based magnetic levitation techniques*, The 10th International Symposium on Linear Drives for Industry Applications (LDIA 2015), Aachen, Germany, 2015.
- D. Grivon, Y. Civet, Z. Pataky and Y. Perriard, *Design and comparison of different Magneto-Rheological valves configurations*, 2015 IEEE International Conference on Advanced Intelligent Mechatronics (AIM), pp. 818-823, Busan, 2015.
- D. Grivon, Y. Civet, Z. Pataky and Y. Perriard, *Bingham-Papanastasiou and Approximate Parallel Models Comparison for the Design of Magneto-Rheological Valves*, Advanced Intelligent Mechatronics (AIM), 2014 IEEE/ASME International Conference on, pp. 168-173, 2014.
- D. Grivon, Y. Civet, Z. Pataky and Y. Perriard, *Experimental Study of Non-Ideal Phenomena Affecting Magneto-Rheological Elastomers Piezoresistivity*, Advanced Intelligent Mechatronics (AIM), 2014 IEEE/ASME International Conference on, pp. 168-173, 2014.

Curriculum Vitae

Reviews

- Z. Pataky, D. Grivon, Y. Civet and Y. Perriard, *Chaussures intelligentes pour patients diabétiques*, Revue Médicale Suisse, Vol. Nouveautés en médecine 2015, No. 502, pp. 143-147, 2016.

– Et pé fronì, i t'it-pué trouà sèn qué teu tchertchaé?

– *Et pour finir, t'as trouvé ce que tu cherchais?*

– Gnénca chûr.

– *Même pas sûr.*

— *Dialogue entre un jeune docteur et sa grand-mère*